EXPERIMENTAL INVESTIGATION OF BUOYANCY DRIVEN MIXING WITH AND WITHOUT SHEAR AT DIFFERENT ATWOOD NUMBERS

A Dissertation

by

BHANESH BABU AKULA

Submitted to the Office of Graduate and Professional Studies of
Texas A&M University
in partial fulfillment of the requirements for the degree of

DOCTOR OF PHILOSOPHY

Chair of Committee,	Devesh Ranjan
Committee Members,	Sharath Girimaji
	J.C. Han
	Gerald Morrison
Head of Department,	Andreas Polycarpou

December 2014

Major Subject: Department of Mechanical Engineering

ABSTRACT

The first objective of the present work is to study Rayleigh-Taylor instability (RTI) mixing, and turbulent velocity statistics at a high Atwood number ($A_t = (\rho_h - \rho_l)/(\rho_h + \rho_l)$) of 0.75. Until now, no detailed experimental results were available at this Atwood number. The second objective is to study the mixing growth rate parameter variation, velocity statistics, and turbulence behavior of combined RTI and KHI (Kelvin - Helmholtz Instability) at different Atwood numbers. In the present study, a new multi layer gas tunnel facility was built at Texas A&M University to perform the experiments. This is a convective type system where fluids with different density (air and air-helium mixture), initially separated by partitions, start to mix in a transparent acrylic test section. A new density probe was developed using hot-wire anemometry techniques to make instantaneous density measurements inside the mixing layer. This probe along with a three wire probe is used to measure instantaneous velocity components and density simultaneously. Visualization experiments are performed to measure mixing heights and growth rates. For the first time, Particle Image Velocimetry (PIV) is also implemented for measuring RTI velocity statistics at these Atwood numbers.

For the RTI experiments at Atwood number 0.75, the spike grew 1.8 times faster than the bubble, and also looked like fragmented dendrite like features rather than the classical mushroom structure. The velocity statistics measured at this Atwood number show self-similarity and scale well with the terminal bubble velocity. These scaling ratios and growth rate parameters are useful to validate existing RTI models. Combined instability experiments have shown that the initial mixing layer development is governed by KHI, and the late time mixing is governed by RTI. This

transition between the two regimes is quantified through the Richardson number at four different Atwood numbers, and observed to be in between -0.8 to -2.3. In the combined instability experiments, almost two decades of inertial range scales confirming the Kolmogorov 5/3 scaling law are observed. The molecular mixing in these regimes, and the velocity PDF evolution during the transition are discussed.

To my parents.....

ACKNOWLEDGEMENTS

I am thankful to Dr. Devesh Ranjan, for his continuous guidance and support throughout my research and stay at Texas A&M University. I would like to thank my committee members, Prof. Girimaji, for his suggestions in analysis, Prof. Han, for his help with the hot wire diagnostics, and Prof. Morrison for his valuable advice in the design of the facility. I would like to thank Dr. Oleg Schilling for carefully reviewing my thesis, and providing valuable feedback.

I would like to thank my lab mates, Adam, Belal, Bryce, David, Eric, Jacob for his advice and suggestions throughout the design and construction phases of the new facility, Kyle, Mark, Sandeep, Sarat, Skylar and Tom, who have been very supportive, and helpful in performing the experiments. I would like to thank my room mates, Aakansh, Abhay, Alok, Ashish, and Sandeep who made my stay at College Station memorable. This work has been funded by DOE grant #DE-FG52-09NA29462.

TABLE OF CONTENTS

LIST OF FIGURES

FIGURE Page

LIST OF TABLES

1. INTRODUCTION

1.1 Motivation

Rayleigh - Taylor instability (RTI) occurs whenever a higher density fluid is placed over a lower density fluid in a gravitational field. The study of RTI is very important to understand the effects of interfacial perturbation growth in Inertial Confinement Fusion (ICF) applications [1, 2, 3]. RTI also plays an important role in supernovae explosions [4, 5], nebula [6], atmospheric sciences [7], and geophysical flows [8]. ICF is one of the confinement techniques which has been proposed to confine fuel for nuclear fusion. In the case of ICF, low density DT (Deuterium-Tritium) fuel is compressed to higher pressure and temperature using compression waves generated from the laser ablation of the higher density pusher material that surround the fuel. Figure 1.1 shows the schematic of the ICF process. The interfacial perturbations present between the layers of material that surround the fuel grow due to RTI and cause fuel dilution at the core of the capsule. The turbulent mixing between DT fuel and the ablator, along with the asymmetry associated with compression, can severely degrade the fusion yield. In order to design better fuel capsules, it is required to understand the mixing phenomenon and the nature of RTI turbulence at these extreme conditions. Most of the RTI experiments performed until till now have focused on acquiring the mixing growth rates of the evolving flow field. To our knowledge, experimental data containing the velocity statistics is not available for the higher density ratio RTI (greater than four) experiments.

The objectives and outcomes of this dissertation are three fold. The first objective is to construct a multi-layer gas tunnel facility and develop a diagnostic to measure the density statistics. The second objective is to study RTI mixing and turbulent

velocity statistics at a relatively high density ratio of 7. There is no consensus in the community regarding the growth rate of this instability for $A_t > 0.5$. The present work reports the values obtained for growth rate values at Atwood number 0.75. The third objective of the present work is to understand and quantify the effect of KHI (Kelvin - Helmholtz instability or shear driven instability) on RTI growth and turbulence. Mikaelian [9], and Hoffmann *et al.* [10] emphasize the presence of this combined instability in an ICF fuel capsule when the incidental shock wave is oblique to the interface due to the asymmetry in the drive. It is important to understand the effect of these shear driven instabilities on RTI growth and turbulence. It is anticipated that the results may provide validation of various numerical models.

In the next two sections, details regarding the Rayleigh - Taylor instability theory, previous experimental work, and important parameters applied in quantifying RTI mixing have been discussed. The basic discussion regarding KHI, and the combined instability follows in the next section. Finally at the end of this chapter, the detailed objectives and the tasks performed to achieve these objectives are listed.

1.2 Rayleigh - Taylor instability

Rayleigh - Taylor instability (RTI) occurs whenever a heavier density fluid is placed over a lighter density fluid in a gravitational field. The necessary and sufficient condition for this instability is $\nabla p \cdot \nabla \rho < 0$, where ∇p is the pressure gradient and $\nabla \rho$ is the density gradient across the two fluid interface.

The schematic of the RTI instability is shown in Figure 1.2 with gravity pointing downwards. The heavier fluid density is ρ_1 and the lighter fluid density is ρ_2. Any small perturbation present at the two fluid interface are unstable and grow in time. The instability is named after Lord Rayleigh [11], who investigated the instability mathematically for the first time and Taylor [12], who first performed the experiments.

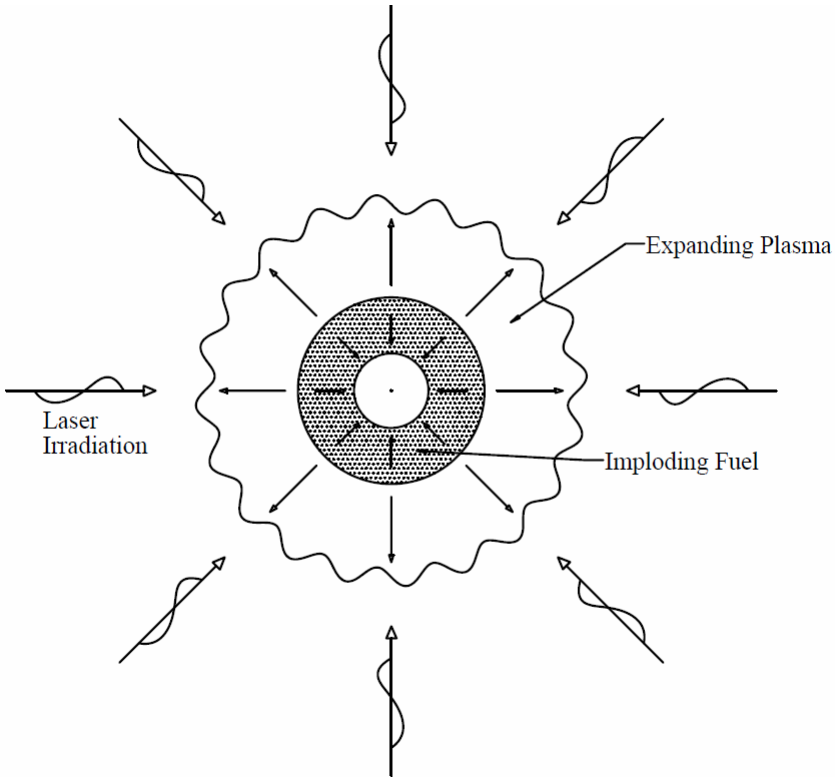

Figure 1.1: A schematic of the Inertial confinement fusion process. The RTI occurs at two stages of the ICF process. During the acceleration stage, the ablated plastic plasma pushing on the plastic causes the RTI to develop, which in turn seeds the perturbations at the fuel - pusher interface. During the deceleration and stagnation stage, the fuel develops enough pressure against the incoming pusher material and the fuel - pusher interface becomes RTI unstable and causes further dilution of the fuel.

Classically, small perturbations at the RTI interface grow in size with time and begin interacting with one another, which leads to turbulent mixing between the two fluids. One important parameter that characterizes RTI is the Atwood number

$$A_t = \frac{\rho_1 - \rho_2}{\rho_1 + \rho_2}. \tag{1.1}$$

The single mode perturbation case was the focus of attention in early RTI experimental and numerical studies. A single mode perturbation grows exponentially

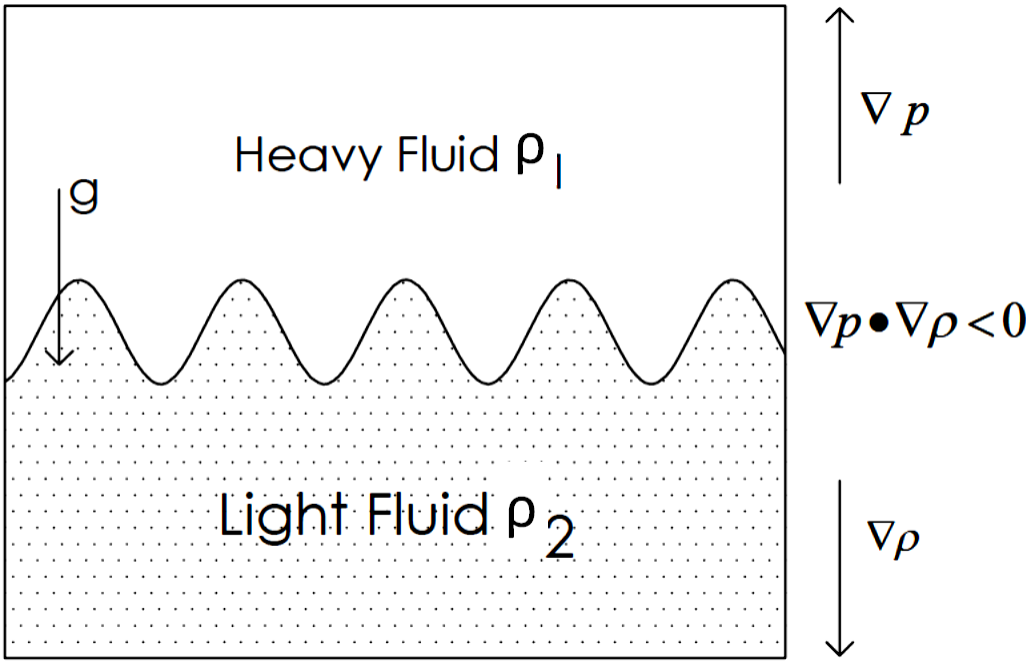

Figure 1.2: Schematic of RTI instability with gravity 'g' in the downward direction. Heavier fluid density is denoted by ρ_1 and the lighter fluid density is denoted by ρ_2. The density gradient and the pressure gradient directions are also indicated.

according to linear stability theory [13], which is valid for small times after the onset of the instability and predicts that smaller wavelength perturbations grow exponentially faster than longer wavelengths for RTI. After a certain time when the amplitude of the perturbation becomes comparable to its wavelength, the growth of the instability is considered to be in the non-linear regime, and other wavelengths begin to appear. In this regime, the bubble (lighter fluid penetrating into heavier fluid) and spike (heavier fluid falling into the lighter fluid) slow down due to the drag forces. When the Atwood number is close to 1.0, Layzer [14] showed that the bubble attains a constant velocity ($v_b = 0.511\sqrt{A_t g R}$, where R is the radius of the cylinder in which the fluids are placed) at late times, extending the theory developed by Davies and Taylor [12]. The spike falls freely at high Atwood numbers growing at

constant acceleration. Gonchorov [15] extended Layzer's theory to obtain the bubble growth and its continuous change from initial exponential growth to late time linear growth at Atwood numbers close to 1.

In the case of multi mode initial perturbations, the growth of these perturbations has been divided into three regimes [16, 17]. The first regime is a linear growth regime where perturbations grow exponentially according to linear stability theory. In the second regime, the small wavelength perturbation growth becomes saturated, when the amplitude of the perturbations reaches half of their initial wavelength. This saturation was demonstrated experimentally by Lewis [18]. In this regime, the exponential growth of successively longer wavelength perturbations persists (mode/bubble competition) and eventually the flow is dominated by longer wavelengths; however, if longer wavelengths are absent in the initial perturbations, then nonlinear interactions between saturated smaller wavelength structures (mode coupling) lead to larger structures. In the third regime, memory of the initial conditions is lost and the two-fluid mixing will reach self-similar growth. The three regime phenomenology has been challenged in recent years, with recognition that the fully self-similar development may not occur in an experiment due to the presence of initial long wavelengths that cause an acceleration of the mixing layer development [19] which, in turn, causes bubble competition and a variable growth rate coefficient. Haan [2] argued that the contribution of mode coupling/bubble competition compared to wave length saturation in the formation of longer wavelength structures, in the late-time non-linear regime, is negligible in contrast to the second regime explanation by Youngs [17].

The late time RTI mixing growth rate is characterized by growth rate parameter α_b and α_s, defined by equation 1.2. The bubble mixing height is h_b, and the spike mixing height is h_s. Both mixing heights are equal for small Atwood numbers $A_t < 0.1$ and asymmetry starts to appear at Atwood numbers greater than 0.1. Dimonte and

Schneider [20] proposed a relationship shown in equation 1.3, between α_b and α_s in terms of the density ratio $R = \frac{\rho_1}{\rho_2} = \frac{1+A_t}{1-A_t}$, through the analysis of their Linear Electric Motor (LEM) experiments, they reported the D_α value to be 0.33 ± 0.05.

$$h_{b,s} = \alpha_{b,s} A_t g t^2 \tag{1.2}$$

$$\alpha_s = \alpha_b R^{D_\alpha} \tag{1.3}$$

Many numerical simulations have been performed to understand the development of the RTI [19]. The mixing growth rate parameters α_b, and α_s were thought to be insensitive to initial conditions in early RTI studies. Youngs [17] performed numerical simulation of both single mode and multi-mode initial perturbations, and proposed that the mix development becomes independent of the initial perturbations. Most numerical simulations predict smaller value of $\alpha_b \approx 0.02 - 0.04$ [17, 21, 22, 23] compared to experimental value of $0.05 - 0.07$ [24, 20, 25]. The discrepancy has not been resolved until recently. Most of the numerical simulations were initialized by small wavelength perturbations and the growth of the mixing layer is mainly due to 'bubble merger' between these small wavelengths [19]. Recent simulations by Dimonte [26] *et al.* and Ramaprabhu *et al.* [27] have shown that the RTI mixing growth parameters α_b are sensitive to the amplitude of the long wavelength initial perturbations. 'Bubble competition' dominates with the presence of longer wave length perturbations, causing longer wavelengths to saturate and grow faster at later times. Simulations by Dimonte *et al.* [19] have shown that the parameter α_b has a lower bound value with initial perturbation spectra containing only small wave length perturbations. Dalziel *et al.* [28] and Mueschke *et al.* [29] measured very long wavelengths in their initial condition spectra and noticed that the inclusion of these wavelengths in their simulations [30, 31] higher growth rate coefficients.

A review of small Atwood number ($A_t < 0.2$) RTI experiments has been given by Andrews and Dalziel [32]. Most RTI experiments are performed in a box type system, in which fluids of different densities are placed one above another. In many such experiments, the fluids are placed in a stratified configuration and the container is accelerated many times the acceleration due to gravity in the downward direction. This provides a body force in the direction opposite to gravity and RTI mixing starts between the fluids. This acceleration is provided through different mechanisms, for example, compressed air to accelerate the liquid column above air [18], rubber tubing and steel wire [33], bungee cords [34], compressed air [35], and a weight pulley drop tower [36]. To obtain large accelerations Read [24] used rocket rig motors, Dimonte *et al.* [37] used a Linear Electric Motor, and Kucherenko [38] used a high pressure gas system. Other type of box type experiments were performed using the acceleration due to Earth's gravity. Andrews *et al.* [39] overturned the box, which is initially placed in a stable configuration, to initiate the instability. Dalziel [40] used a rigid barrier to separate the fluids in an unstable configuration, and the removal of this barrier caused additional initial perturbations in the flow. White *et al.* [41] used a paramagnetic substance in a strong magnetic field to place the fluids in unstable configuration. The same technique was used by Huang *et al.* [42] and Tsiklashvili *et al.* [43]. RTI experiments were also conducted in a high energy density environment using the NOVA laser to test the applicability of available theories at these extreme conditions [44, 45]. They noticed bubble competition and inverse cascading with multi mode initial perturbations.

In general, all box-type experiments have very short experimental times. Most of the experimental setups used either back-lit photography or Laser-induced fluorescence to make measurements of the developing mixing layer. Velocity measurements are very difficult to make in these types of experiments, as the diagnostics are difficult

to implement and the experiments lasts for very small amount of time (typically less than a second). Until now, in the box-type experiments, only Daiziel *et al.* [28] implemented velocity measurement diagnostics using a particle tracking technique to quantify the initial conditions due to the removal of the barrier.

In contrast to box-type systems, a convective type system was first used by Snider [46] to study RTI mixing. Snider [46] used hot and cold water to study RTI mixing at small Atwood numbers ($A_t < 10^{-3}$). In this convective type system, the fluid streams, initially separated by a splitter plate, flow at constant velocity before they start to mix at the edge of the splitter plate. Taylor's hypothesis [47] is used, in assuming that the turbulence as well as flow phenomena are convected downstream at constant velocity equal to the stream velocity. The corresponding time t elapsed from the onset of instability is calculated using $t = \frac{x}{U}$, where x is the stream-wise distance from the splitter plate where the fluids started to mix, and U is the mean velocity of the flow streams. This convective type system allows for larger data sampling times. A typical experiment can last up to few minutes, giving enough time to collect turbulent velocity and density statistics at any point in the flow. Snider and Andrews [25] performed backlighting experiments to obtain mix-width growth rates. They ensemble averaged images taken over four minutes to obtain the statistically converged value of the mix-width. Wilson *et al.* [48] and Wilson and Andrews [49] used thermocouples in the water channel to measure mean density profiles and associated spectra. In this type of convective system, it is also easy to introduce shear between the flow streams by making one of the stream velocity larger than the other. Wilson [50] studied the effect of shear on buoyancy at Atwood number 2.4×10^{-4}. Ramaprabhu and Andrews [51] made PIV measurements for the first time inside of a RTI mixing layer using water channel. They used a S-PIV technique [52] to make simultaneous measurements of turbulent velocity and density

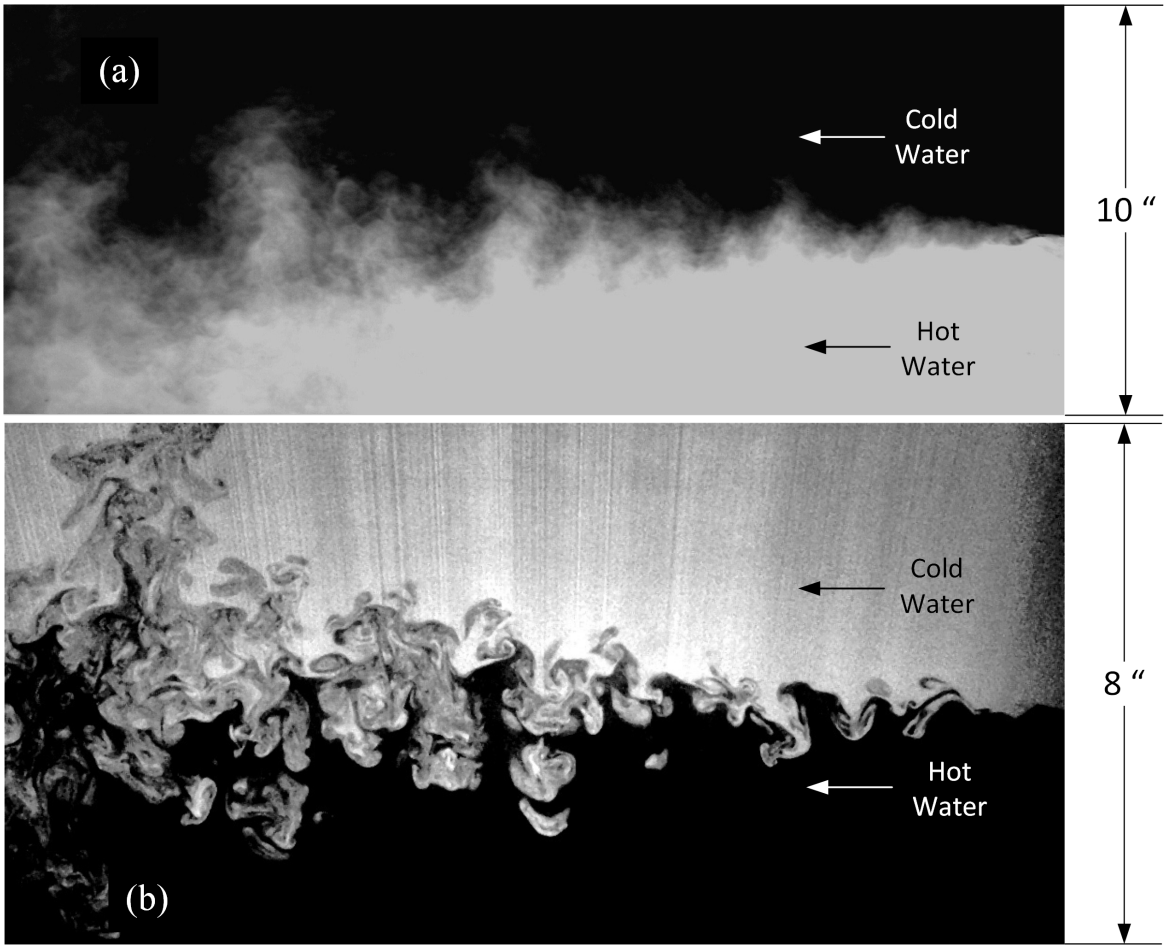

Figure 1.3: (a) Typical backlighting image taken during an experiment at Atwood number $A_t = 4 \times 10^{-4}$ in the water channel facility. The top cold stream is mixed with dye. The concentration of dye is proportional to the volume fraction of the top stream fluid. (b) LIF images taken during an Atwood number, $A_t = 4 \times 10^{-4}$ experiment. The top stream is seeded with fluorescent dye. (Courtesy: Sarat Kuchibhatla, STAML, Texas A&M)

statistics at Atwood number 2.4×10^{-4} . For the first time, they made velocity and density turbulent statistics in RTI mix layers. Mueschke *et al.* [29] quantified the initial velocity and density profiles right after the splitter plate in the water channel using S-PIV as well as thermocouple measurements. Mueschke and Mueschke *et al.* [53, 54] also studied the effect of Schmidt number on molecular mixing in RTI mix layers using the water channel. Figure 1.3(a) shows an image taken during a water channel RTI experiment with the top stream seeded with Nigrosin dye for mixing visualization with a uniform back-lit test section. The span-wise averaged bubbles and falling spike structures can be seen. Figure 1.3(b) shows the image with LIF (Laser Induced Florescence). In the backlighting image, the snapshot of the flow field is averaged in the span-wise direction, while the LIF image is a snapshot of a plane in the span-wise direction. The LIF image gives more details about the structures. Initially the structures are mushroom shaped and coherent. As these structures grow in size, the shear between the bubbles and spikes causes three dimensionality and turbulence.

This concept of convective type system to study RTI instability was further used to build gas tunnel facility [55]. Air is used for the heavier top stream and air-Helium mixtures are used for the bottom stream. To vary the Atwood number one can control the mixture composition of He in the He-Air mixture. Banerjee and Andrews [55, 56] used back-lit transparent test section with digital imaging techniques (similar to the water channel) to measure mixing widths at different Atwood numbers. Banerjee et.al. [57] used an Multi-Position Multi Overheat (MPMO) hot wire technique to measure different turbulent quantities, including vertical velocity fluctuation $\overline{v'^2}$, density variance $\overline{\rho'^2}$, stream-wise velocity fluctuation $\overline{u'^2}$, and turbulent mass fluxes $\overline{\rho' u'}$, $\overline{\rho' v'}$. The MPMO technique is suitable for only measuring statistically steady quantities and fails even at moderate Atwood numbers

$A_t > 0.1$. Moreover, the MPMO technique can only measure statistically averaged quantities and cannot measure instantaneous values. Kraft *et al.* [58] developed a new hot wire technique, simultaneous three wire cold wire anemometry (S3WCA), for measuring velocity and density fluctuations separately and simultaneously using the temperature as a marker for density. They validated the S3WCA technique against MPMO measurements and obtained instantaneous velocity, density, and turbulent mass fluxes. Statistical information including spectra, structure functions and higher order turbulence quantities can be obtained from this S3WCA technique. However, this technique used a three wire hot wire probe (Dantec 55p91) which is limited to flows with velocity rms fluctuations less than $20\% - 25\%$ of the mean flow velocity [59, 60]. In the present work, the gas tunnel facility is used for one set of experiments. A similar system with improved features, including the option to perform multi-layer experiments, was built at the Shock Tube and Advanced Mixing Laboratory (STAML) to further study RTI mixing at high Atwood numbers $A_t > 0.5$. A detailed description of both experimental setups is presented in the Chapter 2. A typical image taken during the experiments for both the gas tunnel facilities is shown in the Figure 1.4.

1.3 Kelvin - Helmholtz instability

In contrast to the RTI phenomenology, KHI occurs when two fluids of different velocities interact with each other. In KHI, like RTI, the mixing between the two streams can also leads to turbulence at late times. KHI between two parallel streams is usually referred to as the plane mixing layer problem. In 1942, Goertler [61] presented the first analytical solution to the mixing layer problem with two streams. He assumed that eddy viscosity is constant across the mixing layer and obtained a series solution for the velocity distribution. A summation of the first two terms in

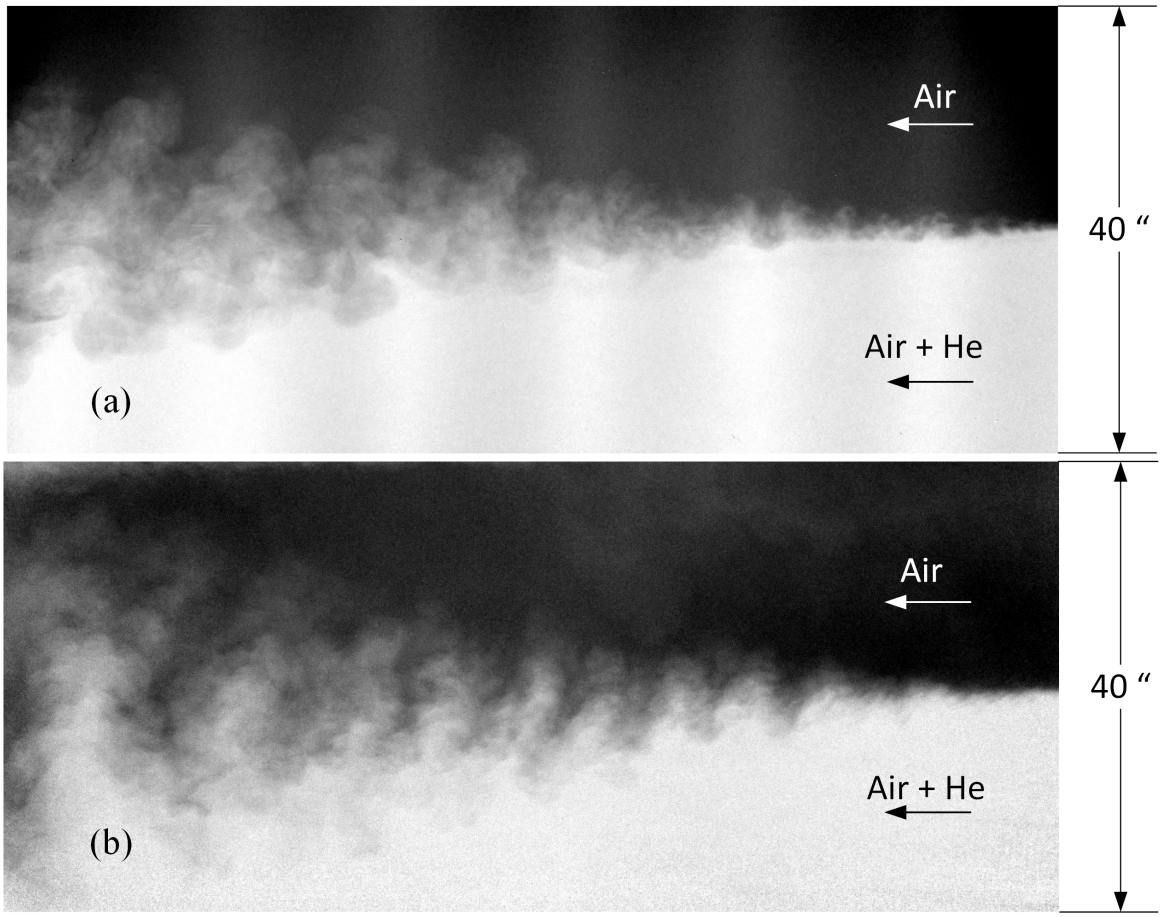

Figure 1.4: (a) Typical back-lighting image taken during an experiment with $A_t = 0.035$, $U = 0.65\ m/s$ in the two layer gas tunnel facility. (b) Typical back-lighting image taken during an experiment with $A_t = 0.63$, $U = 2.7\ m/s$ in the multi layer gas tunnel facility. In both the cases, the top stream fluid (pure air) is mixed with fog. The concentration of the fog is proportional to the volume fraction of the top stream fluid. The bottom stream fluid is a air+Helium mixture.

this solution, and neglecting all other terms, is considered by many researchers to be accurate enough for practical purposes. Using a similar approach, Sabin [62] derived a first order approximate solution with a pressure gradient for the plane mixing layer problem that compared well with the zero pressure gradient solution of Goertler [61] at lower velocity ratios. He suggested the use of the same eddy viscosity for all pressure gradients from his experimental work, and he quantified the dependence of the mixing layer spreading rate on the velocity ratio (velocity of slow moving stream/velocity of fast moving stream) between the two streams. Leipmann and Laufer [63] made the first measurements of the turbulence inside a mixing layer of an air stream issuing out of a nozzle into quiescent surroundings. They estimated the spreading rate and asymmetry of the mixing layer, and compared these estimates with available theories and experiments. They showed that phenomenological theories, like the Prandtl mixing layer theory, are only reasonable when predicting the mean velocity variations, and fail to predict higher order turbulent quantities. Yule reviewed plane mixing layer theory and the experimental data available up to 1972. He conducted mixing layer experiments in a two-stream wind tunnel at different velocity ratios. Yule compared the two stream mixing layer experiments with a free mixing layer (absence of a second stream), and observed that the large eddy structure is affected by the presence of the second stream. Yule also pointed out that Goertler's solution did not consider the asymmetry of the mixing layer, and suggested a method to calculate this asymmetry. Bell and Mehta [64] studied the effect of initial conditions in a plane mixing layer at a velocity ratio of 0.6. They observed a 20% difference in mixing growth rate constant between tripped and untripped initial conditions.

In the case of KHI, small perturbations at the interface grow in size with time and form into span-wise vortical rollups. Winant and Browand [65] studied the process of vortex pairing between two neighboring span-wise vortices using flow

visualization, and they observed that pairing does not always start at the same spatial location due to small spatial and temporal irregularities in vortical structures. They also proposed a model for the mixing width growth rate based on previous non-interacting vortex theories. Browand and Weidman [66] used a conditional sampling technique to study different stages of vortex pairing at small Reynolds numbers (defined based upon mixing width, velocity difference, and kinematic viscosity). The first stage was just after the pairing process, and the second stage was during the pairing process. They measured higher values of turbulent Reynolds stress production during the pairing process. They noted a similar pairing mechanism as observed by Brown and Roshko [67], and proposed that the pairing mechanism at lower Reynolds numbers was universal and can be extended to higher Reynolds numbers. At Reynolds numbers around 2500 Koochesfahani and Dimotakis [68] observed a large amount of high velocity stream fluid trapped inside the rollup with very little or no mixing with the other stream. As the Reynolds number increased above 23000, beyond the mixing transition, they observed enhanced mixing between the streams due to the three dimensionality of the flow, with a still higher amount of high velocity stream fluid at the center of the mixing layer. Lasheras and Choi [69] studied the formation of counter rotating stream-wise vortices on the braids of two dimensional span-wise vortex tubes for different types of perturbations at the splitter plate. Their investigation centered on the growth of these stream-wise vortices and the coupling process with the two-dimensional span-wise vortices that make the flow three dimensional. They observed the same coupling process for both the horizontal and vertical initial perturbations. Brown and Roshko [67] studied the effect of density difference (without any acceleration at the interface, i.e., without any stable or unstable stratification) on flow structure in plane mixing layers. They studied the large-scale structure for density ratios (density of low velocity stream/density of high

velocity stream) of 0.14, 1.0, and 7.0. They noticed similar structures at all density ratios and the change in the value of the spreading angle, which correlates with the mixing width growth rate, is relatively small compared to the change in the density ratios.

The mixing width height for KHI can be defined in many different ways. Pope [47] defines the mixing width δ as the distance between the point where the velocity $U = U_2 + 0.1(U_1 - U_2)$, and the point where the velocity is $U = U_2 + 0.9(U_1 - U_2)$, where U_1 and U_2 are the velocities of the fast moving (top stream in the present scenario), and slow moving streams (bottom stream in the present case) respectively. Another way of defining the mixing width is through the vorticity thickness $\delta_w = \frac{U_1 - U_2}{(\frac{\partial U}{\partial y})_{max}}$ [70]. Many turbulent studies [64, 71] measured error function velocity profiles across the mix layer for KHI. For an error-function distribution, it can be proven mathematically that these two definitions are exactly the same for the mixing width. Another way of measuring the mixing width height is through visualization. The mixing width height measured through visualization δ_{viz}, is approximately two times larger than δ_w [72]. The present work is mainly concentrated on visualization mixing width δ_{viz}.

1.4 Combined instability

One of the objectives of the present work is to study the combined KHI and RTI. The effect of KHI in a stratified fluid (opposite to RTI) is important to study as it affects most of the mixing processes in atmospheric and oceanic flows [73]. The relative strength of buoyancy to shear can be quantified using the Richardson number ($Ri = \frac{-g(\frac{\partial \rho}{\partial z})}{\rho(\frac{\partial u}{\partial z})^2}$), where g is gravity, $\Delta\rho$ and ΔU are the density and velocity differences respectively, and ρ are $2h$ the measured mean density and the mixing width. The Richardson number, defined based on the initial mixing width at the onset of the instability, is referred to here as initial Richardson number. The Richardson number

values are positive for stably stratified flows and negative for unstably stratified flows.

Thorpe [74] studied stably stratified shear flow by filling a long rectangular tube with different fluids and then tilting the tube before bringing it back to the horizontal position, in order for the instability to develop. From different experiments varying the parameters defining the Richardson number, Thorpe [75, 76] observed that at a Richardson number value of 0.33 striations started to appear and the turbulence started to decay. He observed that the ratio of the velocity interface thickness to the density interface thickness (velocity and density interface thicknesses are defined as the distance between the points in the mixing layer where the velocity and density reach their respective free stream values) increases with increased values of the initial Richardson number. The final Richardson number, defined at the center of the layer based on both velocity and density interface thickness, remained constant irrespective of the initial Richardson number after a fixed non-dimensional time from the onset of turbulence. Browand and Winant [77] performed experiments in a stratified shear layer and noticed that the mixing layer width collapsed onto a single final curve irrespective of the initial density difference between the streams. They concluded that turbulence due to the shear cannot be maintained in a stably stratified fluid. Koop and Browand [78] studied the turbulence and flow structure at different Richardson numbers in a stably stratified fluid with shear. They observed that at low Richardson numbers < 0.15, the vortical structures similar to the plane mixing layer still persist in their visualization experiments. The result was similar to Thorpe's observation [75]. The flow induced by these vortical structures pushed the heavier fluid to the top and the lighter fluid to the bottom. The vortical structures grew in size due to vortex pairing, but were unable to sustain against buoyancy and disintegrated before re-laminarizing into a non-turbulent flow. As the initial Richardson number increased further, the formation of the vortices was not observed and the flow structure was

replaced by interfacial waves. They showed that the decay of turbulence in the re-laminarizing region is similar to grid turbulence decay [78]. They compared the value of the maximum Richardson number at which turbulence started to decay with the non-interacting vortex model, and found good agreement with Thorpe's experiments. They also observed a decreased amount of molecular mixing with increasing values of initial Richardson number at a point well after the start of turbulence decay.

Shifting attention to unstably stratified (KH+RT) flows, Shumlak and Roderick [79] observed stabilization of RT instability with shear in Z-pinch implosions from their analytical and numerical work, including the effect of magnetic forces. Lawrence *et al.* [80] performed a stability analysis, with and without a finite interface thickness, for KH+RT flows. They also performed experiments in an unstable configuration in a water channel and noticed the transformation from shear instability dominated flow to RTI dominated flow. They presented the flow structure evolution in the channel for a compound shear and buoyancy case. Snider and Andrews [25] studied the effect of shear on RTI experimentally at small Atwood number (< 0.005). They did not notice any change in mixing width compared with RTI at late times in their compound shear and buoyancy experiments. They also observed a similar flow structure evolution as Lawrence *et al.* [80]. Due to experimental setup limitations Snider and Andrews [25, 81] could not achieve a higher velocity difference between the two streams. Snider and Andrews [82] simulated the compound case using a $k - \epsilon$ model, and found that the addition of shear to RTI decreased the mixing width growth rate, countering the perception that the addition of instabilities would increase the growth rate. Snider and Andrews [25, 82, 81] stated that the addition of shear to unstable buoyancy will not increase the mixing width growth rate, and more experiments were needed to check their simulations. More recently, Olson *et al.* [83] studied the effect of shear on RT instability numerically in the non-linear regime,

immediately after the linear regime, and found that the peak mixing width growth rate (highest mixing growth rate observed in time) changed non-monotonically with the increased amount of shear. They found an optimum value of shear for fixed RTI parameters at which the peak mixing width growth rate is minimum. The flow structure resembled pure KH instability at the point of lowest growth rate. They observed that the addition of a small amount of shear decreased the amount of vertical turbulent kinetic energy channeled from the available energy and resulted in a smaller mixing width growth rate.

1.5 Objectives of the present work

The three main objectives of the present work are as follows.

1. To design and construct a multi-layer gas tunnel facility for performing high Atwood number experiments. To design a density probe which can measure the volume fraction of Helium, rather than using a temperature marker technique [59].

2. To quantify the mixing heights and mixing growth rates for RTI at an Atwood number of 0.75. To measure turbulence velocity and density statistics, including $\overline{u'^2}$, $\overline{v'^2}$, $\overline{w'^2}$, $\overline{u'v'}$, $\overline{\rho'^2}$, and $\overline{\rho'v'}$ at this Atwood number.

3. To understand the effect of KHI on RTI growth, and turbulent statistics behavior. To quantify the transition point from the shear dominated behavior to buoyancy dominated behaviour in the combined instability.

The following tasks have been performed to achieve these objectives.

1. The original two layer gas tunnel facility was refurbished to work at a new location. Visualization and hot wire diagnostics were implemented and validated.

Combined instability experiments were performed at an Atwood number of 0.035 using this facility.

2. A new multi-layer gas tunnel facility was built which is capable of studying the mixing between eight different streams. The limitations of the old gas tunnel facility were kept in mind when designing this new facility.

3. A new density probe is designed to measure the volume fraction directly, instead of a using temperature marker for density measurements inside the mixing layer

4. Particle Image Velocimetry (PIV) is implemented for the first time in measuring velocity statistics at Atwood numbers greater than 0.01.

2. EXPERIMENTAL APPARATUS AND DIAGNOSTICS

In this chapter, two experimental setups that are used in the present work are explained. Three different diagnostics are used in the present work. One of them is a new diagnostic technique, which measures the Helium concentration directly, and is explained in detail. The implementation of other two diagnostics including visualization and Particle Image Velocimetry (PIV) is also described.

2.1 Two layer gas tunnel facility

The two layer gas tunnel facility was constructed by Banerjee and Andrews [55] to perform RTI experiments up to Atwood numbers 0.75. Unlike the box type systems, this facility is a convective type system where fluids of different densities move at constant velocity throughout the system. It is a blower type facility where both streams are initially separated by a splitter plate, flow parallel to each other, and start to mix after the splitter plate in a transparent plexiglass test section. In this statistically steady system, the velocity and mixing statistics of RTI can be collected by performing the experiments for longer times up to a few minutes depending on the availability of gases, unlike box type experiments where the experiment lasts only for a few seconds or less. This facility is an extension of the low Atwood number water channel facility [46] where hot and cold water are used as fluids to create the density difference. The density difference is created in the gas tunnel facility by injecting Helium into the bottom stream. Different Atwood numbers can be obtained by varying the amount of the Helium gas that is injected.

For this convective type system, Taylor's hypothesis is used for the coordinate transformation. The time elapsed from the onset of the instability is defined as $t = \frac{x}{U}$, where x is the distance from the splitter plate in the stream-wise direction and U is

the mean stream velocity. This time t is the same as the actual time measured from the onset of the experiment in the box type systems. The time dependent statistics measured in the current system would be same as the x-direction statistics from the box type system. The schematic of the two layer gas tunnel facility is shown in the figure 2.1. The stream-wise flow direction is taken as the x axis, the mixing layer developing transverse direction is taken as the y axis and the span-wise direction is chosen as the z axis. This facility is a blower type system with a blower connected to each of the streams. The blowers have air dampers which are used to adjust flow rate of the air coming into the streams. The bottom stream blower supplies the required amount of air into the mixing section. Helium is injected from the side at the blower exit. The blower exit has at least five to six times smaller cross section that the flow stream. Injecting Helium into this smaller cross section increases the contact area between both fluids. The mixture is then passed through a set of baffles to increase the residence time, thus increasing the mixture uniformity. The air-helium mixture is then supplied to the settling section on the upstream side of the test section through four lines of six inch flexible aluminum ducting. For the top stream, the fluid path is similar except that it does not pass through baffles in the mixing section. The fluid streams then pass through the settling section containing a honeycomb structure and a set of wire screen meshes. The details about the mesh sizes and their placement are given by Banerjee [56]. The honeycomb structure acts as a flow straightener and the meshes downstream of the honeycomb section reduce the turbulence and flow non-uniformities. Different diagnostics are used including visualization for measuring the mix width, and the S3WCA [59] hot wire technique for making simultaneous density and velocity measurements. This experimental setup is used for part of the present work, i.e., for the combined instability (KH+RT) experiments at Atwood number 0.035. All other experiments are performed using a new multilayer gas tunnel

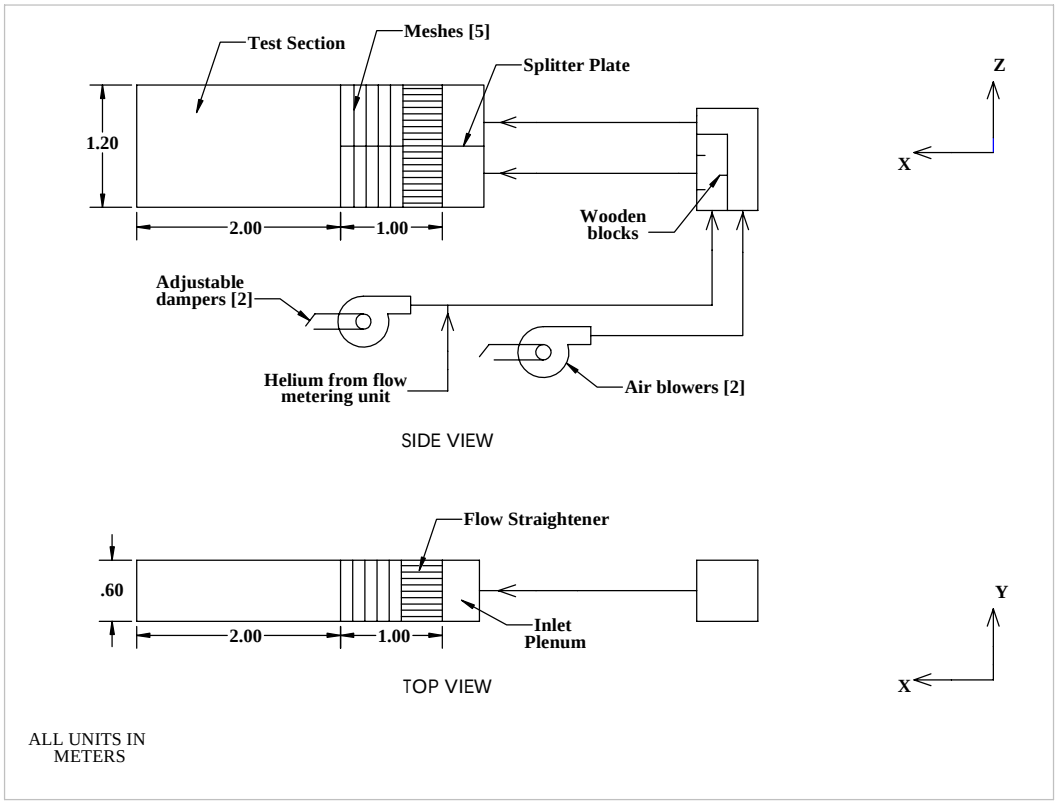

Figure 2.1: Schematic of the two layer gas tunnel mixing facility.

facility. The details about the new facility are given in the next section.

2.2 Multi layer gas tunnel facility

The second facility is the multi layer gas tunnel facility, designed and built as a part of the present work. This new facility was built keeping in mind about the limitations of the two layer gas tunnel facility. This facility can handle up to seven different streams. RTI mixing between more than two streams, and combination of different effects including shear, and stable stratification can be studied using this facility.

2.2.1 Limitations of the two layer gas tunnel

- In the two layer system, the lighter density bottom stream must push the heavier air out of the system during the start of the experiment. If there is no suction provided at the exit of the test section, the lighter density bottom stream fluid always tends to rise over the existing ambient air inside the test section. The resulting flow is similar to the flow shown in the Figure 2.2 (a). In the Figure, the bottom stream fluid is seeded with fog particles and the fog is illuminated from the top of the test section. The initial resident air causes the shifting of the mixing layer, and this problem becomes severe for larger Atwood number experiments. Kraft [59] built an exit plenum with a flap that would push both streams downward so that the ambient air initially in the tunnel is pushed outwards. This technique is not effective for high Atwood number experiments, and a splitter plate had to be used in conjunction with the exit plenum flap. The exit splitter plate configuration is shown in figure 2.2 (b). Due to the use of this exit partition, mixing width information could not be obtained at a distance over 120 cm from the splitter plate.

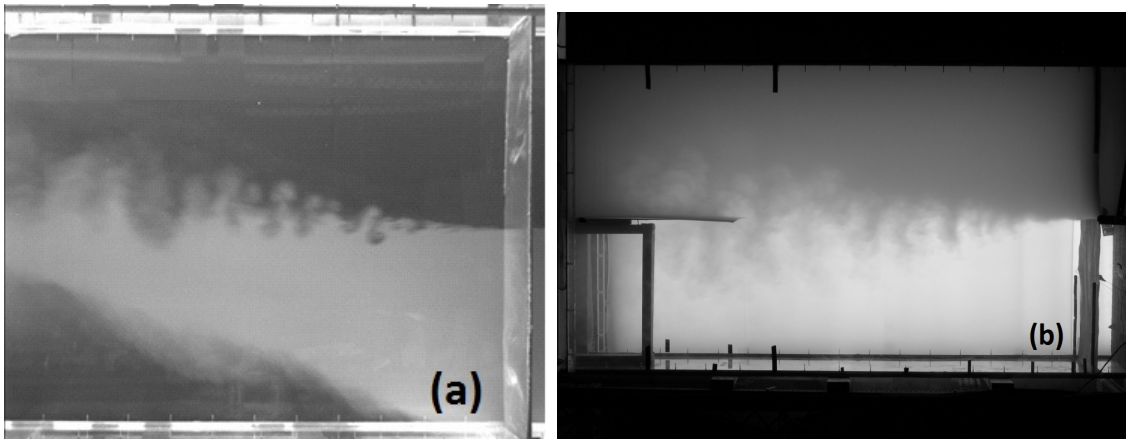

Figure 2.2: (a) Lighter stream rising over the ambient air in the two layer gas tunnel. The lighter density fluid stream is seeded with fog particles and the illumination is provided from the top of the tunnel (b) Exit splitter plate used to avoid the back flow problems for the Atwood number ~ 0.6 experiment.

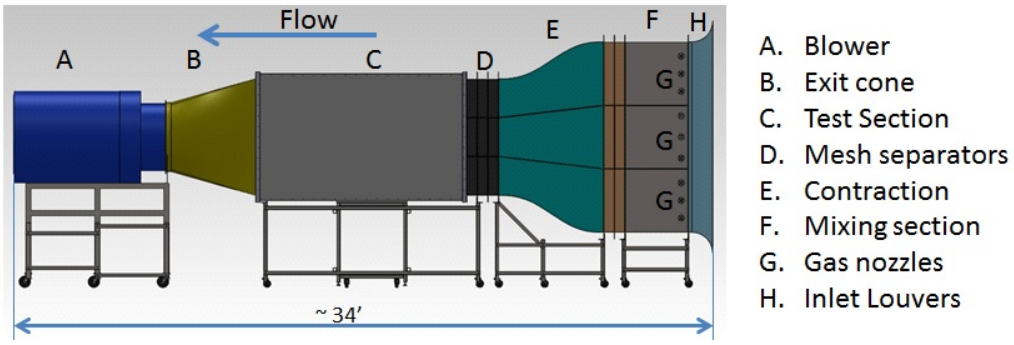

Figure 2.3: Front view of the new multi layer gas tunnel facility.

- The mixing section of the gas tunnel is too restrictive and the blowers operating at these larger pressure drops provide very small flow rates. The maximum stream velocities that can be obtained are less than 2 m/s. This velocity limitation has put a restriction on the maximum Atwood number at which the tunnel can be operated. Smaller velocities at higher Atwood numbers cause faster mixing and gives less area to operate and perform diagnostics.

- The wire screen meshes are mounted on a plastic grid of $\frac{3}{4}$'' spacing and $\frac{1}{8}$'' thickness. This provided a characteristic wavelength to the flow in the span-wise direction.

2.2.2 Multi layer gas tunnel facility

A new multi layer gas tunnel facility is built at Shock Tube and Advanced Mixing Laboratory. The facility can handle up to eight streams of fluids with different densities separated by partitions. This facility can also be used a two layer RTI facility.

- It is a suction type facility where a single fan draws air through the entire system. The velocity of the air through the system can be controlled by adjusting the pitch angle of the fan blades. Another control parameter is the distance between the test section exit and fan inlet.

- Velocities up to 20 m/s can be obtained when the fan is run at full capacity.

- The back flow problem is absent and the fluids are drawn into the test section by the fan.

- The modular design gives flexibility to add or remove sections of the facility easily.

- This multi layer facility can handle up to eight streams of different fluids with different densities. The streams height can also be adjusted by simply adding or removing the partitions.

- The wire screens are placed in between the mesh separators, removing the longer wavelength perturbations in the span-wise direction.

- The velocity difference between the streams is provided by adjusting the louver opening at the entrance of the tunnel.

The CAD model front view of the new multi layer gas tunnel facility is shown in Figure 2.3. All the sections of the facility are mounted on a carbon steel stand with rollers. The rollers give the flexibility to move the section around. Section A is the fan section which draws the air through all the other sections. The blower is a pitch-adjustable axial vane fan manufactured by Joy Manufacturing Company, which can provide air flow rates up to 33,600 cubic feet per minute (cfm). The fan blade angle can be adjusted using a pneumatic control relay, which operates using a pressure differential on both sides of a piston sliding inside a cylinder. Generally, the fan is not operated at its fully capacity and the coarse adjustment of velocities is done either by moving the fan away from test section with the help of rollers, or by adjusting the blade pitch angle through a pneumatic controller. The fan needs to be lubricated frequently using a grease gun.

Section B is an exit cone that connects the rectangular test section (Section C) to the circular entrance of the fan. It has a three inch collar on the fan side in which a 36'' diameter honeycomb structure is mounted to prevent the swirl from the fan being propagated upstream. Section B is extended on the test section side by 4 feet to increase the distance between the fan and the test section so that the effect of swirl that is being propagated to the test section is small. This extension section is a

rectangular wood box with a door which is, 66'' tall, 24'' wide, and 48'' long, and is used as an access point to enter into the test section.

Section C is the test section made out of $\frac{1}{2}$'' thick plexiglass. It is a 10 feet long, 6 feet tall and 2 feet wide rectangular section with slots made on top for providing access to hot wire probes. The plexiglass has higher than 99% transmittance in the visible wavelength range and less than 20% transmittance in the UV wavelength range. For acetone PLIF (Planar Laser Induced Fluorescence), separate slots have to be made to let the UV (Ultra Violet) light enter into the test section. Backlighting made out of LED panels is placed behind the test section. This LED light panel is 10 feet long, 6 feet tall, and mounted on a wooden stand. A large matte Acetate paper sheet, generally used for diffusing light in photography applications, is attached on the back of the test section to diffuse the light coming from the LED panel. The test section is also mounted on a separate steel frame with rollers.

In this multi layer setup, the configuration is set for a three layer system for the present work. Each section on the upstream side of the test section consists of four subsections made of $\frac{1}{8}$'' thick sheet metal and two partitions made of $\frac{1}{8}$'' thick Aluminum. The four subsections include closed bottom and top subsections and two middle subsections. All of the subsections are joined by bolts with partitions sandwiched between them. The middle subsections have seven slots in them, and the partitions can be placed in those slots to create streams of different heights.

Section D consists of wire mesh screens to manipulate the flow turbulence. The screens are characterized by a pressure drop coefficient (K) and velocity refraction coefficient α_θ [84]. The mean velocity non-uniformity reduction and the turbulence fluctuation reduction can be related to the pressure drop coefficient through simplified theory and empirical relations [85]. The screens will develop secondary instabilities that will contribute to spatial non-uniformity, if their solidity is greater than 0.5

[85, 86]. Tan-Atichat *et al.* [87] proposed that the Reynolds number based on the wire mesh diameter (Re_d) should be larger than 50 for the turbulence reduction to be independent of the free stream velocity. Groth and Johansson [88] found that cascading of two different screens with smaller wire diameter on the downstream side provided larger turbulence fluctuation reduction. They also suggested that the spacing between them should be greater than the initial turbulence decay region, at least $100 - 150$ mesh sizes. For the present experimental setup, the three screens used are a 36×36 mesh with 0.0065'' diameter wire, a 50×50 mesh with 0.0055'' diameter wire, and a 60×60 mesh with 0.0045'' diameter wire, respectively. The spacing between them is six inches. A full screen mesh was used by Koop [89] in a stratified shear layer water channel experiment to reduce the effect of boundary layers at the end of the splitter plate. The third mesh serves that purpose in the present case. The meshes are sandwiched between mesh separator sections made out of $\frac{1}{8}$'' thick sheet metal.

Section E is a contraction section connecting the settling/mixing section to the mesh screen separators. The cross sectional area at the start of the contraction is 36'' $\times$36'' and at the end of the contraction is 24'' $\times$22'', providing an area ratio of 2.5 which is smaller than wind tunnels used for planar mixing layer experiments [90]. Space and manufacturing budget constraints limited the area ratio in the present scenario. A fifth order polynomial ($y = 6x^5 - 15x^4 + 10x^3$) is chosen for the contraction shape [90] in the transverse direction y, and the span-wise reduction in size followed linear variation with stream-wise distance x. This section also mounted on a separate steel stand with rollers.

Another set of mesh separators are placed in between the contraction and settling section. A 10×10 screen with 0.0280'' diameter wire is placed at the contraction interface. This wire screen is placed on the downstream side of the flow straightener.

A honeycomb core of 36'' $\times$36'' and 3'' thick with $\frac{1}{4}$'' cell size is placed close to the wire mesh following the recommendations of Loehrke and Nagib [91]. This flow straightener breaks down the large scale structures and suppresses the lateral velocity component. Shear instabilities further develop on the downstream side of the honeycomb structure and those instabilities are suppressed by the wire screen placed on the downstream side.

Section F is the settling/mixing section. The gases are injected into the system using gas nozzles G. The mixing section has holes to mount the gas nozzle sections inside the mixing section. The gas nozzle sections are PVC pipes with $\frac{1}{4}$'' diameter holes along the length and perimeter of the pipe. Each section has nine PVC pipes across, and each PVC pipe has $12-15$ holes for injecting the gas. Helium coming out the holes is spread over the entire section using baffles and circulating fans. Helium is the most common gas injected through these holes for generating density difference between the streams. It is noticed that, for low Atwood number experiments, when the Helium flow rates are small, Helium is not uniformly distributed throughout the section. As Helium is lighter than air, it settles at the splitter plate, and the actual Atwood number at the splitter plate is higher than the Atwood number calculated based on the total air and Helium flow rates. The resulting Atwood number at the splitter plate can be 100% higher than the average Atwood number for an experiment at Atwood number 0.06. This difference becomes smaller (around 35% at Atwood number 0.18) for higher Atwood number experiments. To avoid this problem, Helium is mixed with Nitrogen before being injected through the gas nozzles. This almost nullified the Helium non-uniformity issues even at Atwood number 0.06. The density profiles obtained with two different Helium flow rates with and without N_2 mixing are shown in the figure 2.4. At higher flow rates of Helium, the mixture is relatively uniform compared to smaller flow rates without N_2 mixing. With N_2 mixing, the

density profile is uniform throughout, even for the smaller flow rate of Helium.

Section H contains louvers to adjust the velocity of the streams, and are used for finer adjustment of the velocity. By moving the louvers, the velocities can be increased or decreased in increments as small as 0.05 m/s. These louvers play an important role in creating shear between the streams. Velocity profile and fluctuation rms (root mean square) measurements are made inside the tunnel without baffles or mixing nozzles at a mean velocity of 2.5 m/s. The mean velocity variation in the transverse direction in a stream is $\approx 4\%$ of the mean velocity and the turbulent intensity value is around 0.4% of the mean velocity measured at a point.

Although this multilayer gas tunnel is built for experiments with more than two streams of fluids, it is currently setup for three streams. In the present work, only the bottom and the middle streams are used as working streams. During the experiments, the top stream velocity is set equal to the middle stream velocity so that the mixing between the top and middle streams does not affect the mixing between the middle and the bottom streams. Hereafter, the actual middle stream is referred to as the top stream.

2.3 Diagnostics

Three types of diagnostics are used in the present work for making mixing height and velocity statistics measurements. A visualization technique combined with digital imaging is used to make mixing height measurements. The second diagnostic is based on hot wire anemometry. In this diagnostic, a newly designed density probe is combined with a set of velocity and temperature probes to make instantaneous density and velocity measurements. The third diagnostic is the Particle Image Velocimetry (PIV) technique implemented for the first time in RTI experiments to make velocity measurements at Atwood numbers greater than 0.01.

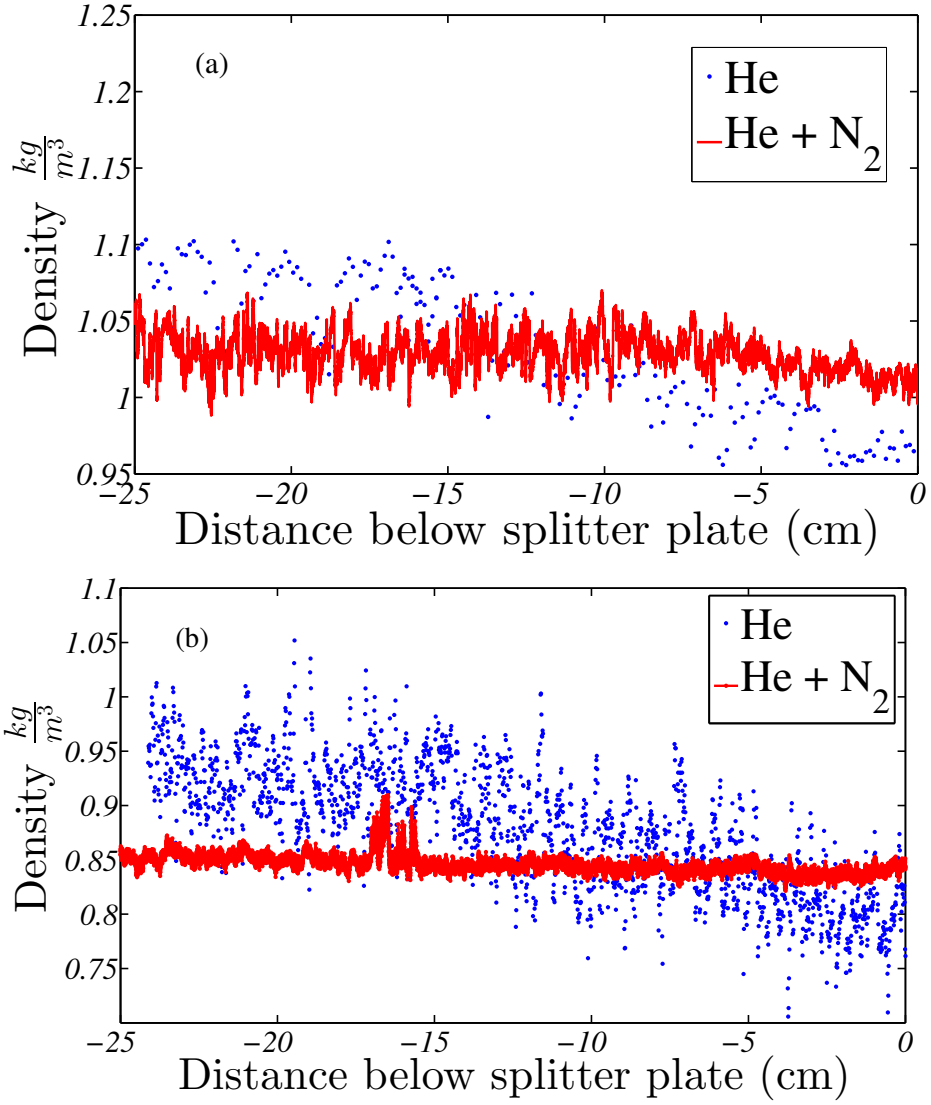

Figure 2.4: (a) Density profiles measured with the new density probe, with Helium injection rate = 0.0234 lbm/s (b) Density profiles with Helium injection rate = 0.062 lbm/s.

2.3.1 Visualization

For flow visualization, the test section is backlit using LED panels mounted on wooden board (same size as the test section). Seven panels of 4 feet $\times$ 2 feet and one panel of size 2 feet $\times$ 2 feet (from LEDWHOLESALERS.com) are tiled together to cover the entire area. The light from these panels is diffused further through acetate paper sheets attached to the backplate of the plexiglass test section. Fog particles, composed of condensed ethylene glycol droplets (ATMOSPHERES fog fluid, High End Systems), are injected into one of the streams. The fog density is approximately four times air density at room temperature, and the addition of fog to a fluid stream changes the fluid density. This effect is more prominent at small Atwood numbers ($A_t < 0.05$). The fog flow rate is approximately 2 grams per second, changing the Atwood number by 2% at Atwood number 0.07. The injected fog is used as a light extinction medium for the light coming from the back-lit LED panels. Before the experiment, it is ensured that the absorption due to fog is linearly proportional (thin medium approximation of the Beer - Lambert's law [92]) to the volume fraction of the fog for that camera settings and the fog flow rate, using wedge calibration technique [55]. This calibration is necessary for obtaining the volume fraction contours from the visualization. After injecting the fog particles, images are taken at a rate of $60 - 300$ images per minute. The rate chosen during an experiment depends on the velocity and Atwood number for the experiment. For larger Atwood numbers ($A_t > 0.2$), the flow rates inside the test section are relatively high and the images can be captured at a higher rate. The total number of images per experiment depends upon the number of structures convected past a particular location. The number of structures needed per averaging, so that the mixing width information obtained from the image analysis is statistically convergent, is roughly around 200. At $A_t \sim 0.5$, the chosen convective

velocity ($U = 2.3\ m/s$) is three times the convective velocity ($U = 0.8\ m/s$) chosen for the $A_t \sim 0.05$ experiment. Thus for the $A_t \sim 0.5$ case, the images can be captured at a rate three times faster than the $A_t \sim 0.05$ case, making a reasonable assumption that the number of large scale structures formed would be same for both the cases.

Experiments are repeated two times for each visualization run, the first time with fog injected into the bottom stream, and the second time with the fog injected into the top stream. This is needed as the signal from the fog injected stream is less compared to the other stream. For example, the signal for bubble mixing width is less when the fog is injected into the top stream and vice versa. The Spike width is obtained when the fog is injected into the top stream and the bubble mixing width is obtained when the fog is injected into the bottom stream. The density profiles across the mixing layer can be calculated with either of the cases. A Nikon® D90/D4 camera is used for obtaining the images during an experiment with an aperture f8, ISO sensitivity of 100 and a shutter speed of 1/100 seconds.

Images obtained for each case are ensemble averaged over all the images and corrected for non-uniformities in the background using $I_{corr} = \frac{I_m}{I_0} I_0^{uniform}$ [55], where I_{corr} is the corrected image pixel intensity, I_m is the measured average pixel intensity, I_0 is the actual background pixel intensity, and $I_0^{unfiorm}$ is the background intensity for which the correction need to be made.

From the corrected image, the 95% pixel intensity contour line is taken as the bubble mixing height or the spike mixing height. The MATLAB ® contour function is used for obtaining the 95% pixel intensity curve for both bubble and spike height curves.

2.3.2 Hot wire diagnostics

As most RTI experiments are performed in box type systems, velocity measurement diagnostics are difficult to implement due to short experimental run times. Very few RTI experiments have measured velocity statistics. Dalziel *et al.* [28] used particle tracking methods to quantify the initial conditions due to the removal of the barrier between the heavier and lighter stream fluids. Ramaprabhu [51] implemented the SPIV technique in their convective type water channel facility to make instantaneous measurements of velocity and density. The SPIV technique is a PIV technique with more particles in one of the streams than the other to measure density by correlating the number of particles at a particular location with the volume fraction of the fluids. Kraft *et al.* [58] discussed the hot-wire diagnostics used in RTI mixing layers. They implemented the MPMO single wire technique to measure velocity, and density time averaged statistics. They also used temperature as a marker for one of the fluid streams and demonstrated its validity for the instantaneous measurement of density in air-helium mixture RTI mixing layers. They coupled this temperature marker technique (S3WCA) with a three wire hot wire probe, operating on Constant Temperature Anemometry (CTA), to make instantaneous velocity and density measurements. In the present work, this S3WCA technique is used to make the instantaneous density and velocity measurements. More details about the temperature marker technique combined with the three wire probe are explained by Kraft [59].

A new density probe is developed to make instantaneous measurements of Helium concentration at a particular location. The working principle of the probe, its validation and its measurements in an RTI mixing layer are shown in the next section. This new probe is used to primarily validate the temperature marker technique. The demonstration experiment shown by Kraft *et al.* [58] makes the measurements when

the air-Helium mixtures are completely mixed, rather than making measurements when they are partially mixed. In the actual scenario, the heat diffuses much faster than the Helium and the temperature markers had to be adjusted to compensate for this faster diffusion of heat. The present probe measurements are compared to the temperature marker technique measurements in the next section. The temperature technique poses problems at large Atwood numbers because expanding Helium reduces the bottom stream temperature significantly (more than 7 °C for the $A_t \sim 0.6$ case) [59]. Moreover, the temperature distribution is not very uniform compared to low Atwood numbers. The new density probe measurements are independent of the temperature and this probe gives accurate values for density. The density probe can detect slightly higher amount of molecular mixed fluid due to the sleeve in front of the probe. This sleeve construction can further be improved to measure correct density values inside the mixing layer. This density probe is placed next to the S3WCA probes to make instantaneous measurements of the Helium concentration.

2.3.2.1 Density Probe

A new X-hot wire probe was designed in-house to measure Helium volume fraction in the developing flow field. Way and Libby [93] used an X-probe to make Helium concentration measurements in air-Helium mixtures. To avoid interference, they first used a larger separation between the sensors and lower overheat for the wire, and they found that the voltage relationship between the two is very weak. Providing interference between the wire and the film actually made the relationship stronger with helium concentrations. In their follow on work, Way and Libby [94] used the probe to make concentration and velocity fluctuation measurements in an air-Helium jet entering into quiescent air. They mentioned that interference probes can not perform well at low velocities and higher concentration of Helium if the influence

of the film on the wire is excessive. On the other hand, if the interference is low, it becomes difficult to differentiate between helium concentration and velocities. Stanford and Libby [95] used another film on the downstream side of the wire and made cross component velocity measurements. Sirivat and Warhaft [96] used a similar probe successfully combined with a temperature probe to make stream-wise velocity, concentration, and temperature fluctuation measurements simultaneously. Panchapakesan and Lumley [97] used another X-wire probe in combination with an interference probe to make stream-wise, cross stream and concentration fluctuation measurements. All these measurements are made for lower concentrations of Helium less than 40% by volume.

In contrast to Way and Libby, Harion *et al.* [98] found that the interference is not actually necessary if the wire is more overheated than the film, for making Helium concentration measurements. They successfully made measurements inside a turbulent boundary layer using this probe. Mazur *et al.* [99] also used the probe suggested by Harion for making Helium concentration measurements. These probes have to be custom made and sufficient infrastructure including a microscope, is needed. In the present case, a probe similar to the probe suggested by Harion et.al. is used. A TSI number 1240 cross flow probe is used with a -T1.5 sensor on the downstream side of the film -T20 film sensor. This X-wire is mounted onto the TSI 1155-18 X-wire probe mount. The wire is operated at 250°C and the film is operated at 80°C using a Dantec MiniCTA 54T42 constant temperature anemometers. The probe is calibrated with different concentrations of air-helium mixtures by exposing it to a nozzle mounted at the exit of a pipe flow with a fully developed velocity profile. The film is relatively insensitive to the helium concentration compared to the wire. This feature, as pointed out by Harion, can be used to make Helium concentration measurements in our experiments at higher volume fractions of He.

A typical calibration curve is shown in Figure 2.5. As can be seen from the graph, for the current range of calibration velocities up to 3 m/s, and volume fractions, the calibration curves are well conditioned. The wire response is high for Helium concentration compared to the velocity. The film response is the same for both velocity and Helium concentrations. This difference in sensitivities can be used to find the volume fraction and velocity at a particular point in a air-Helium mixture. The X probe is exposed to an air jet from the calibration nozzle at a larger distance and air-Helium mixtures during RTI mixing. The measurement points obtained from these measurements overlaid onto the calibration map are shown in figure 2.6. The blue background lines represent the calibration curves up to the expected helium volume fractions for jets. The red line with circles are the measurements in an air jet. The air jet has large cross stream and span-wise velocity fluctuations and the conditions are very different from the calibration where these components are absent. Due to these velocity components, the measurements are out of the calibration range. During RTI mixing, the probe is placed close to the splitter plate where the mixing starts between the air and air-Helium streams. As the cross stream and span-wise components are small compared to the stream-wise velocity the measurement points (green dots) are all inside the calibration curves and predicted helium volume fractions very well. When the probe is moved to a location further downstream of the splitter plate, the cross stream and span-wise velocity components become comparable to the stream-wise velocity, as the mixing layer develops. The measurement points at that location are in black. The measurement points are spread over very large range of velocities and are out of the calibration range, again due to the presence of significant cross stream and span-wise velocities.

Stanford and Libby [95] used swept film in front of the interference probe to make radial velocity component measurements. They also checked the validity of the

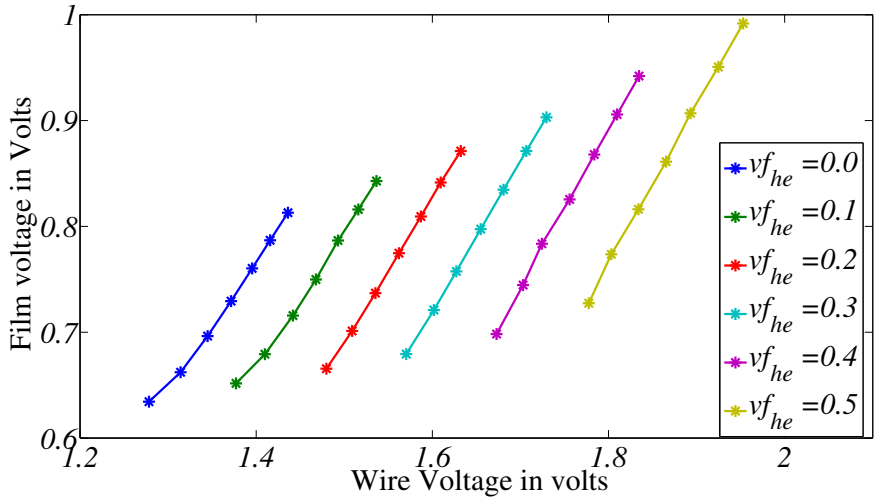

Figure 2.5: Typical calibration curves of X-wire density probe exposed different volume fractions of Helium. Each data point on each curve represents different velocity

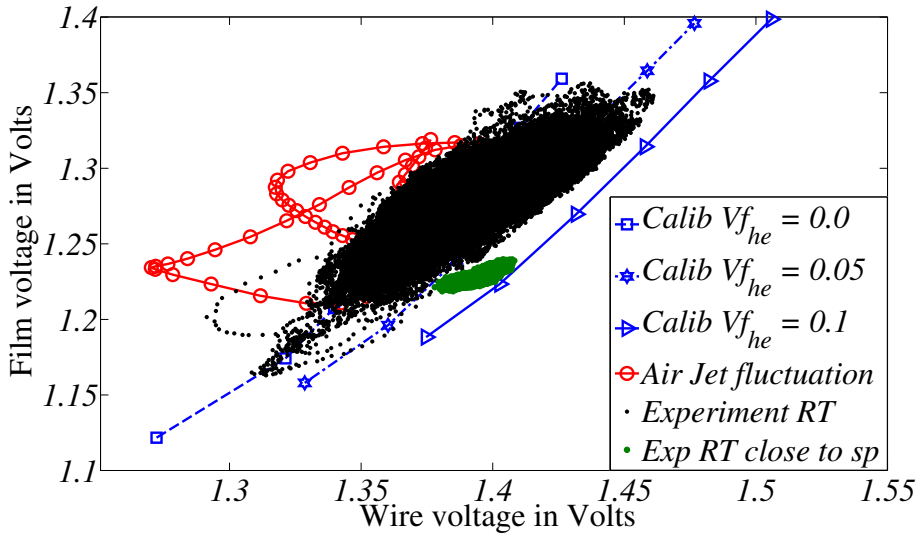

Figure 2.6: X-wire density probe signal for different experiments without any sleeve surrounding it. The background lines are the calibration curves. The red line with circle markers indicate the signal when the probe is placed in a turbulent air jet. The black dots indicate the density probe signal in the late time RTI mix. The green (gray) dots indicate the signal at early time RTI mixing.

assumption made by Way and Libby [93] that the density probe is not responsive to small velocity angles, i.e., traverse and span-wise velocity components. From their calibration data at an velocity angle of 10 degrees, they found that the interference probe measurement error is less than 1%. LaRue and Libby [100, 101] used the interference probe and made measurements inside of a turbulent boundary layer slot injected with Helium. The maximum transverse velocity fluctuation they measured is about 12% of the mean velocity. They reported accuracy problems in high turbulent intensity regions. Harion *et al.* [98] repeated the slot injection experiments and reported intensity measurements similar to LaRue and Libby [100] using a simpler probe without any interference. As explained above, the current probe is similar to the probe used by Harion *et al.* [98]. The current probe performed relatively well closer to the plate where the turbulent velocity intensities are relatively small (less than 5%). At a location where the turbulent intensity is about 20% of the mean stream-wise velocity and the measurement points are out of the calibration range.

For the present scenario, the measurements have to be made in a region where the turbulent intensities are more than 20% of the mean convective velocity. To make the probe work in that situation, it has to be isolated from these cross stream and span-wise fluctuations. A thin copper sleeve is built around the probe and any fluid sensed by the probe will travel through the tube for about 2 inches. The fluctuations would be damped by the time the fluid is sensed by the probe. The velocity measurement by the probe would be wrong, but the probe can still measure the instantaneous density if the mass diffusion is small. The scatter of measured points inside of the mixing layer along with the calibration curves for the density probe are shown in figure 2.7. With the installation of the sleeve, all the measurement points fell inside of the range of the calibration curves. By using the MATLAB ® curve fitting tool, a two dimensional curve fit is made between wire, film voltages

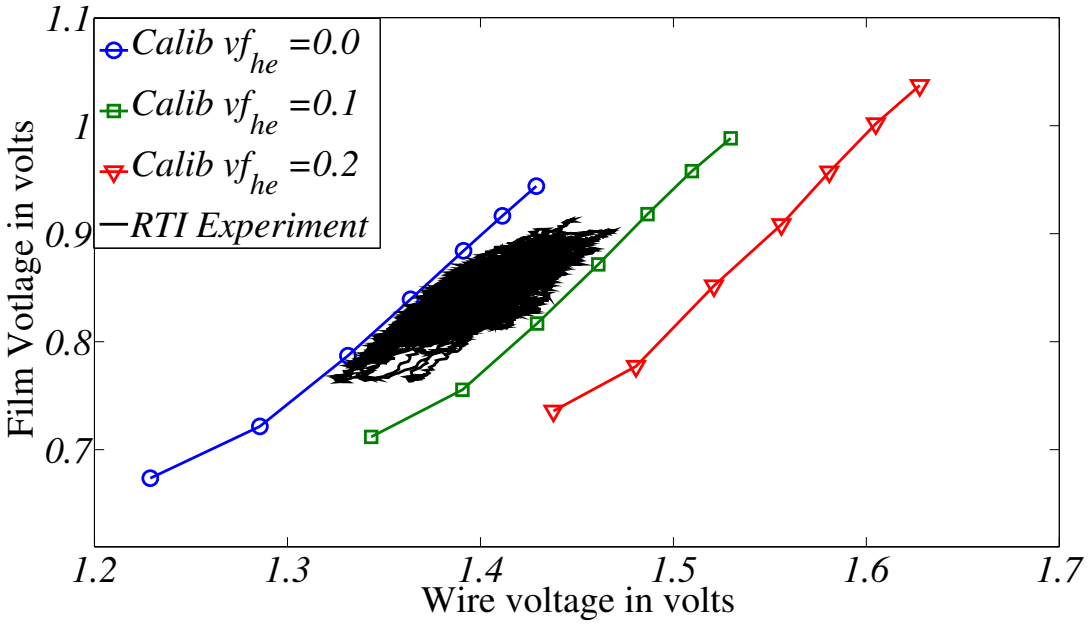

Figure 2.7: X-wire density probe signal from the experiment superposed on the calibration curves for the probe with a sleeve built around it to suppress the vertical and span-wise velocity components

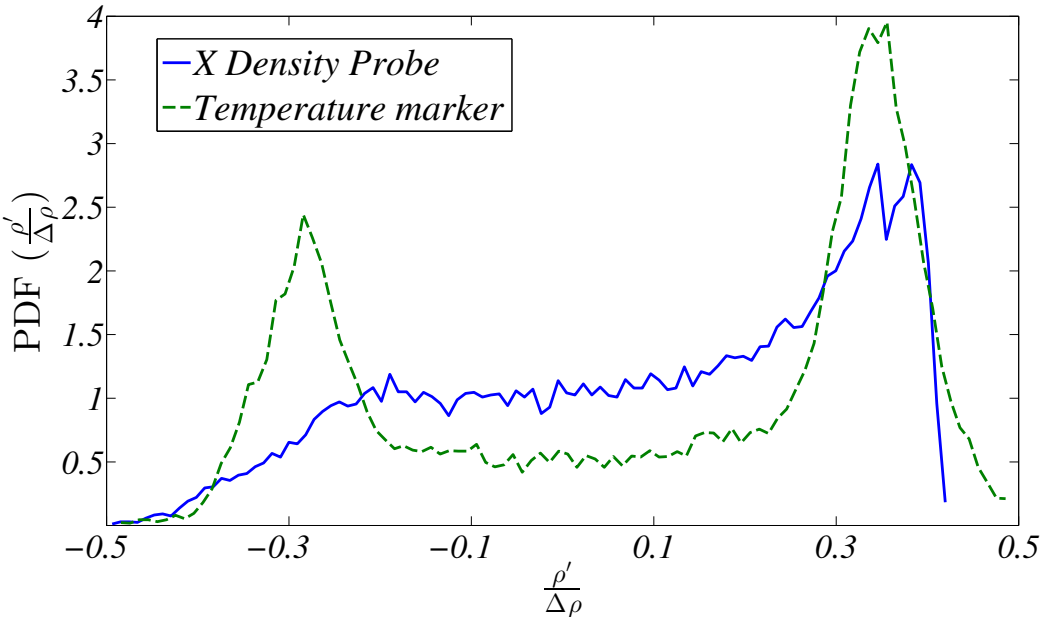

Figure 2.8: Density PDF comparison from X-wire density probe, and temperature marker technique at a particular location in the mix layer.

and helium volume fractions from calibration data. The curve fit is exported as a function, and that function is used to evaluate the helium volume fraction using the wire and film voltages measured from experiments. When the calibration data is fed back to this function, the root mean square (rms) difference between the evaluated helium volume fraction and the actual actual helium fraction is less than 1.5 %.

Until now, the gas tunnel (convective type RTI) facility used a temperature marker technique to measure the volume fraction of each stream at a particular point in the mixing layer. One of the streams (preferably bottom as it improves the Atwood number due to heating) is heated by $2 - 5^{\circ}$C depending upon the Atwood number. As the Schmidt number of the flow is close to 1 [59], heat and mass diffuse at the same rate. Thus, the measured temperature in the mixing layer can be correlated with the volume fraction of the stream through mass and energy balance. Kraft [59] validated this technique by mixing different volumes of Helium into a hot air stream, and measuring the temperature of the mixture after both the streams are well mixed. This mixture temperature followed exactly the temperature predicted by the temperature marker technique. But this demonstration experiment does not validate the fact that heat and mass are diffusing at same rate as the measurements were made when the fluids are very well mixed.

In the temperature marker technique, the maximum and minimum temperatures measured by the temperature probe at the center of the mixing layer is not equal to the free stream temperatures at that location, indicating that the temperature diffuses faster than the mass. The temperature values have to be shifted close to maximum and minimum values measured by the temperature probe to obtain reasonable values of molecular mixing parameter and density statistics. The new density probe can also be used to validate whether the shifting technique for correcting the data in the temperature marker technique. This probe can also be used to replace the temperature

marker technique for density measurement. Figure 2.8 shows the Probability Density Function (PDF) of the density fluctuations measured just above the center of the mixing layer at a distance of 120 cm from the splitter plate in an Atwood number 0.07 experiment with convective velocity of 1.3 m/s. The region is spike dominated and the PDF distribution shows a larger peak on the positive side. The peak on the left side correspond to bubbles and it is smaller is magnitude compared to spikes as the probe is above the center of the mixing layer. The curve between the peaks represents the amount of molecularly mixed fluid available at that location. For the temperature marker technique, the free stream temperatures are adjusted to maximum and minimum temperatures sensed for the PDF calculation. Both the distributions from the temperature marker technique and the density probe show similar features. Even with the shifting of the temperatures, the locations of the peaks measured by both techniques is approximately the same. The magnitude of the peaks indicated by both techniques is different. The density probe measured more molecularly mixed fluid compared to the temperature marker technique, as can be seen from the smaller peaks for pure fluids and higher plateau in between the peaks. The shifting of the temperatures for the temperature marker technique might have taken out the tail of the curve on the left side of the density PDF. The residence time of the fluids inside the sleeve is relatively small, and the molecular mixing due to the sleeve should be small. The molecular mixing parameter θ values measured by the temperature marker technique and the density probe are 0.69 and 0.78, respectively, although the qualitative nature of the PDF is similar.

One other use of the density probe is to measure density profiles close to the splitter plate to see whether the helium injected into the air stream is well mixed or not. The density profiles close to the splitter plate are shown in the next section. The density probe can not be used in conjunction with other probes to measure the

cross correlations as the probe is two inches into the sleeve. The density probe can not be mounted two inches upstream of the other probes as the sleeve is considerably larger and other probes would be in the wake of the density probe.

2.3.3 Particle image velocimetry

Particle image velocimetry (PIV) is a common technique used for making velocity measurements in experimental fluid dynamics. Unlike hot wire anemometry, the PIV technique is non-intrusive. Velocity measurements can be made over particle of size of order of micrometers that are seeded into the flow and illuminated using a laser sheet. Two laser pulses separated by time Δt are used to illuminate the particles. The movement of the particles is captured by a camera. Cross correlation analysis is applied between these two images, by dividing the image into different windows. The correlation peak in each window corresponds to the average movement of the particles in that window. This average movement of particles is used to calculate the velocity in that window.

For the current PIV setup, two or three different laser sheets are used to illuminate the PIV particles at different locations in the test section. A Litron LPU 550 dual head laser with 120 mJ pulse at a maximum frequency of 15 Hz is used with laser sheet optics to form a laser plane at two different locations inside the test section. A beam splitter splits the beam in to two different sets of laser sheet optics. Each set of laser sheet optics contain a converging lens (convex lens focal length 1000 mm), a diverging lens (focal length -15/-12.7 mm), and a reflecting mirror (2'' size) to reflect the beam to the measurement area in the test section. Another laser (Newwave, model GEMINI 15Hz, dual head, 120 mJ per pulse) is also used for some of the experiments closer to the splitter plate. Flash lamps of both the lasers are triggered by a National Instruments DAQ card PCIe-6321. The Q-switch output signal from Litron laser 1

is taken and fed into a BNC model 555 pulse delay generator (Berkeley Nucleonics Corporation). The pulse delay generator in turn triggers both the Q-switch and the flash lamp of Laser 2 of both the lasers. The images are captured by dual frame CCD cameras (TSI model 630157), equipped with 50 mm focal length Nikon lenses. The camera delay between each frame is controlled by TSI INSIGHT4G® software. The cameras are connected to a frame grabber mounted on the motherboard of the image acquisition computer. The Random Access Memory (RAM) of the computer is increased to 24 GB, so that the images can be captured for longer times at the highest possible frame rate of 15 Hz. For each experiment 1200 images are acquired

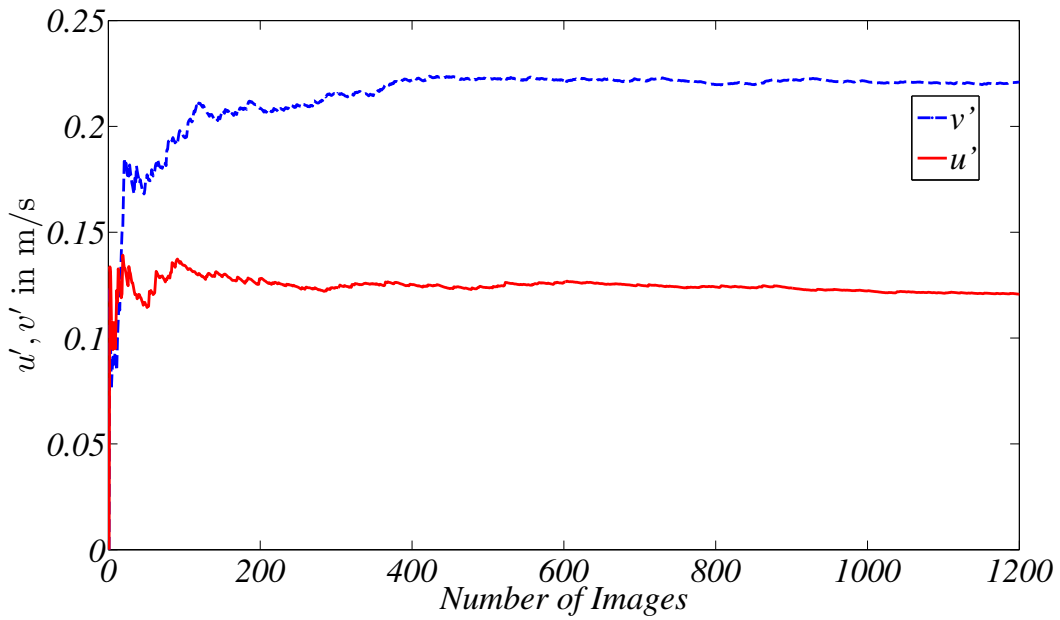

Figure 2.9: Turbulence quantities u', v' variation with the number of images taken at 15 Hz for the experiment at Atwood number 0.07, at a stream-wise distance of 2.4 m from the splitter plate.

at the rate of 15 Hz. The root mean square (rms) value of turbulence fluctuations reach a statistically steady state value after 600 images. The variation of turbulence

fluctuation rms with the total number of images is shown in Figure 2.9. The variation after 600 images is less than 3% of the value. Thus, the 1200 images taken for each experiment should represent statistically steady statistics of the flow field.

Images are captured and processed using TSI INSIGHT4G® software. Processing of the captured PIV images is done using the default PIV engine, with Recursive Nyquist grid engine and a cut-off signal to noise ratio (SNR) of 1.5. In almost all cases, the number of vectors which passed the SNR test are greater than 95%. Most of the vectors that did not pass the SNR test are at the edges. All of the processed image output in INSIGHT4G .vec form is exported into MATLAB®, and further processing is done, including the calculation of mean velocity profiles, turbulence statistics, and probability density functions (PDF). Typical PIV images obtained during the experiment, and their corresponding vorticity contours are shown in figure 2.10. The structures are visible due to the difference in the seeding intensities in the top and bottom streams. The dots are the particles in the flow field and their size is between $0.2 - 1\mu$ m. Figure 2.10 (a) shows the PIV image obtained with KHI only, i.e., there exists only the velocity difference with no density difference. Typical span-wise vortical rollup is clearly visible from the particle seeding. The corresponding vorticity contours are shown in figure 2.10 (b). Similar sets of images are shown in figure 2.10 (c-d) for RTI. The rising bubbles, and falling spikes can be clearly seen due to the seeding difference in both the streams. The shear between two structures forms the rollups shown in the figure. Corresponding vorticity contours show the direction as well as the strength of these rollup structures.

PIV technique is validated for Kelvin - Helmholtz instability (i.e., shear only instability). Velocity profile comparison with the analytical solution for the self-similar planar mixing layer problem [47] is shown in figure 2.11,with $\zeta = \frac{Y - Y_{0.5}}{\delta}$, $f(\zeta) = \frac{U - U_c}{U_s} = \frac{1}{2}\text{erf}(\frac{\zeta}{\sigma\sqrt{2}})$, where U_c is the average velocity of the two streams, U_s is

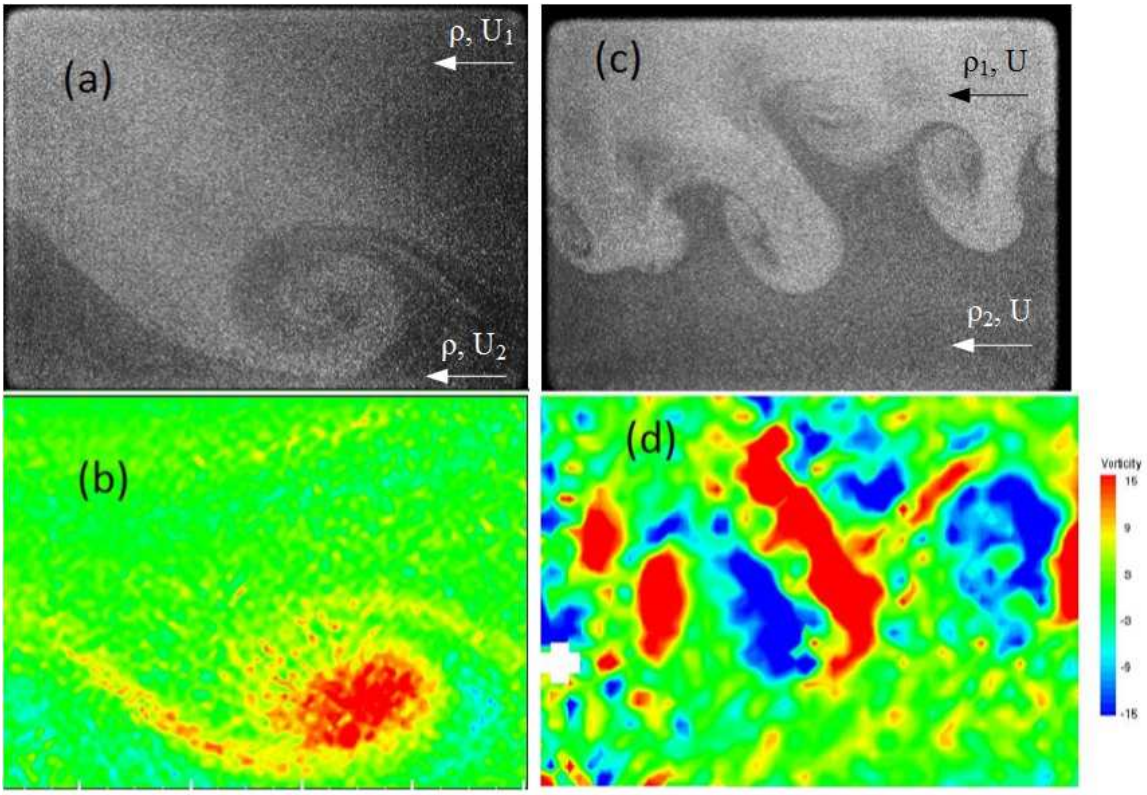

Figure 2.10: (a) Typical PIV image taken during a Kelvin - Helmholtz (shear only) experiment with top stream in the image moving faster than the bottom stream. (b) Vorticity contours corresponding to the image in a calculated from Insight 4G. (c) Typical PIV image taken during a RTI experiment, the bottom stream is air+Helium mixture. (d) Vorticity contours corresponding to the image in (c) calculated from Insight 4G. For all cases, both streams are seeded with PIV oil particles (Glycerine). The imaging area is roughly 6'' ×4''.

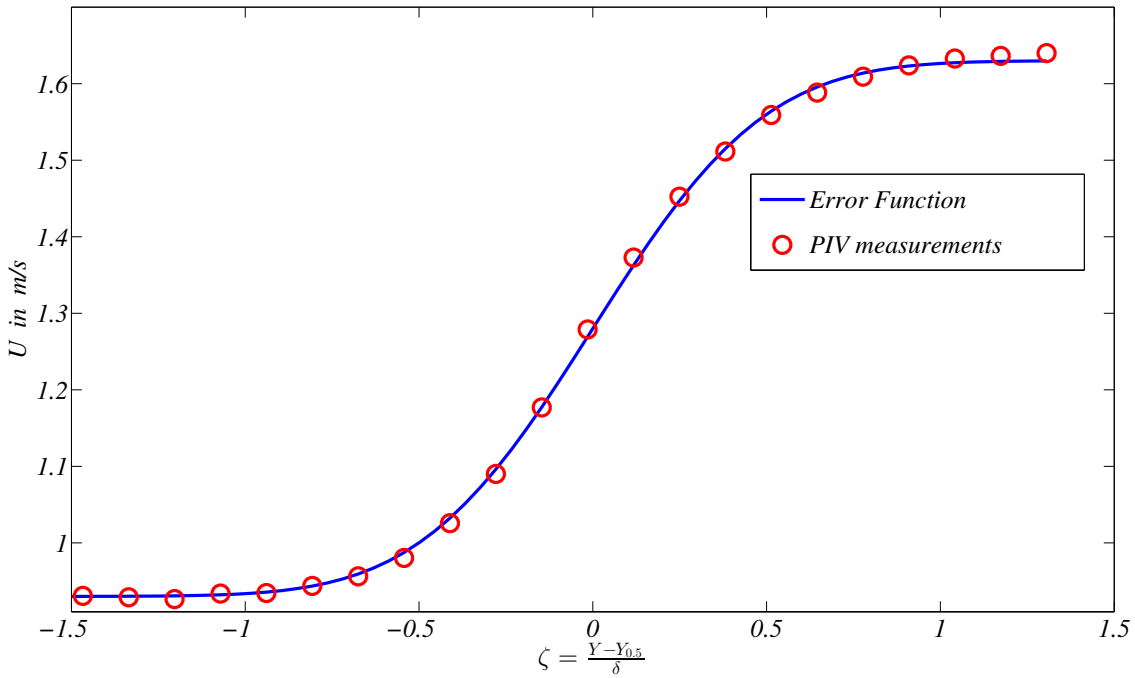

Figure 2.11: Velocity profile comparison between PIV measurements and analytical self-similar error function profile.

the difference in the velocity of the two streams, $\sigma = 0.3902$, $Y_{0.5}$ is the location of the cross stream point where velocity $U = U_c$, and δ in the distance between the two cross stream points $Y_{0.1}$ [where $f(\zeta) = -0.4$], and $Y_{0.9}$ [where $f(\zeta) = 0.4$]. For the current case, $U_l = 0.93\ m/s$, and $U_h = 1.63\ m/s$. This profile is measured during the early development of the mixing layer at 18 '' away from the splitter plate. The top stream is the fast moving stream with a velocity of 1.63 m/s and the bottom stream velocity is 0.93 m/s. The velocity profile is obtained by averaging over 1200 images at 15 Hz.

The profile agrees very well with the self-similar analytical profile. The turbulence statistics measured are also compared with the hot wire measurements from [58] and the experimental results of Bell and Mehta [64]. The turbulence quantities

Table 2.1: Different turbulence quantities measured for the shear only case with $U_l = 0.93\ m/s$ and $U_h = 1.63\ m/s$, i.e., $U_s = 0.7\ m/s$ $U_c = 1.28\ m/s$.

	$\frac{\overline{u'^2}}{U_s^2}$	$\frac{\overline{v'^2}}{U_s^2}$	$\frac{\overline{u'v'}}{U_s^2}$
PIV	0.031	0.026	0.010
hotwire	0.030	0.025	0.012
Bell and Mehta [64]	0.032	0.019	0.012

measured by Bell and Mehta [64] are at very high Reynolds numbers (defined based on velocity difference, δ, and kinematic viscosity 10^4) and the present measurements have not reached such a high Reynolds number. Current measurements are made at a location (x = 1.45 m), where the Reynolds number is 7500. The turbulence quantities measured here compare well with hot wire measurements. In our experiment, we have used PIV to accurately set the initial velocities.

3. HIGH ATWOOD NUMBER EXPERIMENTS

In this chapter results obtained from the experiments conducted at Atwood number 0.75 are discussed. In these experiments, we have implemented all three diagnostics discussed previously in the experimental diagnostics section. The section has been divided based on the results using the three diagnostics. The coordinates x, y, z are defined in the stream-wise, cross stream, and span-wise directions respectively. The origin is located at the edge of the splitter plate and half way along the edge in the span-wise direction. The y direction is considered positive upwards and the z direction is considered positive away from the observer standing in front of the test section.

3.1 Visualization results

Visualization is performed using two different methods, light extinction technique and Mie-scattering technique. In both methods, fog (oil particles made from Ethylene glycol) is injected into one of the flow streams. In the case of light extinction measurements, a back-lighting system built using LED light panels, is placed on the back side of the test section. This is used to illuminate the fog particles. The signal is collected on the front side of the test-section using a digital camera. For the Mie-scattering measurements, a planar laser sheet (plane containing both stream-wise direction and cross stream direction) is used to illuminate the fog particles. The Mie-scattering technique gives the flow structure details and the mixing height in a particular plane, whereas the back-lighting technique gives the span-wise average of the mixing height averaged over the entire width of the test section.

3.1.1 Visualization: Back-lighting

The louvers on the front of the tunnel are closed enough to allow only a small amount of air into the system. This air is used for seeding the bottom stream with oil particles for the PIV measurements. This air entering into the bottom stream also introduces the uncertainty in the Atwood number. The amount of air entering the bottom stream is $\approx 2\%$, which changes the Atwood number by 3% at the present Atwood number. This amount of air is not enough to give good signal for the visualization experiments. Thus, the fog is injected into the top stream for the visualization experiments.

For the current experiment, both the flow streams are moving at an average velocity of $U = 3\ m/s$. Two hundred images are acquired at the rate of seven images per second using a Nikon ® D4 camera f/8 focal length, 1/125 second shutter speed, and ISO sensitivity of 100. All the images are rotated, cropped, and corrected using the formulation prescribed by Banerjee and Andrews [55]. The 95% and 5% volume fraction contours are extracted from the corrected average image. The spike and bubble widths are measured as the distance of the corresponding volume fraction contours from the geometric centerline. The mixing width evolutions for the present case is shown in figure 3.1. The blue line corresponds to the 5% volume fraction contour of the bottom stream fluid, indicating the bubble width h_b. The red line corresponds to the 95% volume fraction contour of the bottom stream fluid, indicating the spike width h_s. It has to be noted that in the case of convective type system, the down stream distance x is related to the time from the onset of the instability using the relation $x = Ut$. At early times, the mixing width is very small and has higher uncertainty. Both bubble and spike widths have shown similar evolution with distance during the initial times. The overall behavior appears to be quadratic in

time.

At later times, the spike width is much higher than the bubble width. This asymmetry is a characteristic of high Atwood number RTI, reported previously in the experiment of Dimonte and Schneider [20]. Dimonte and Schneider [20] quantified this asymmetry using the ratio $\frac{\alpha_s}{\alpha_b}$, as a function of density ratio, using a power law shown in equation 1.3. For a density ratio of 6.4, corresponding to an Atwood number of 0.73, the Dimonte correlation predicts a value of 1.84 ± 0.16.

3.1.2 Growth rate parameters

The mixing growth rate parameters α_b, and α_s are defined by equation 1.2. These parameters can be calculated using different methods, namely the virtual-origin (VO) method [25] and Ristorcelli - Clark (RC) method [102]. The VO method has been used for the plane mixing problem to evaluate the spreading rate parameter [64]. To implement the VO method in the current scenario, equation 1.2 is modified to the form shown in equation 3.2 to take care of the initial mixing before self-similarity. In the RC method, $\alpha_{b,s}$ are calculated using equation 3.1. The VO method gives a single $\alpha_{b,s}$ value for the total time, whereas the RC method can capture the local fluctuations in $\alpha_{b,s}$ with time. For the RC method, the $\alpha_{b,s}$ value is obtained by averaging the parameter over the last quarter of the test section. The variation of $\alpha_{b,s}$ with time is shown in figure 3.2. Initially, the $\alpha_{s_{RC}}$ value is ≈ 0.3 and fluctuates around the mean value of 0.077 from $t = 0.4$ seconds. This drop in α_s represents the transition regime between the linear regime, where the growth rate is exponential, and the self-similar regime, where the growth rate is parabolic.

$$\alpha_{b,s_{RC}} = \frac{(dh_{b,s}/dt)^2}{4A_t g h_{b,s}} \tag{3.1}$$

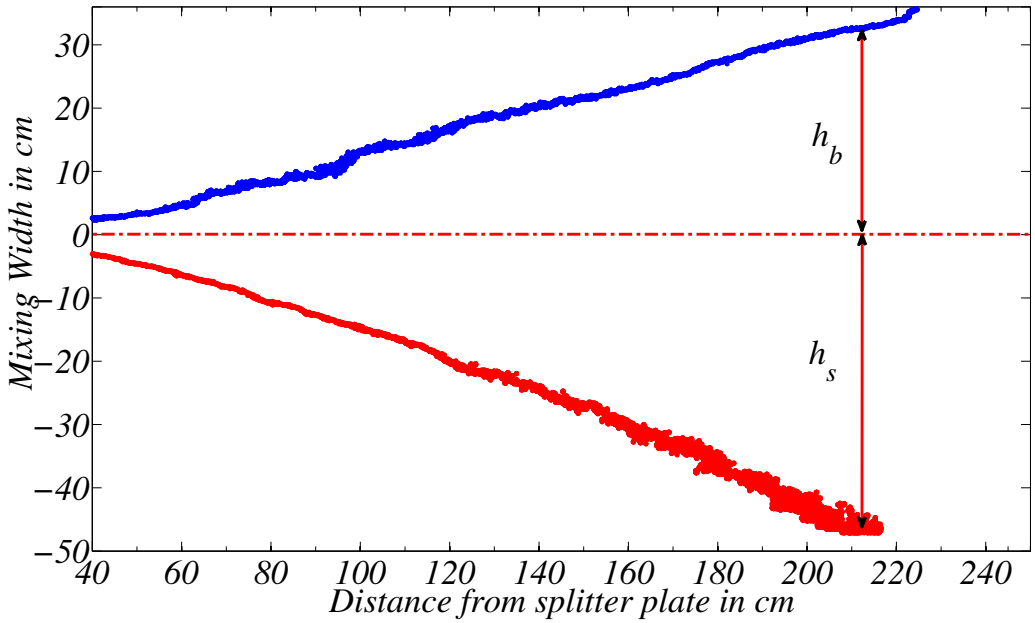

Figure 3.1: The bubble and spike mixing height evolution with downstream distance calculated from the ensemble average of 220 images, for an experiment at Atwood number 0.75, $U = 3\ m/s$.

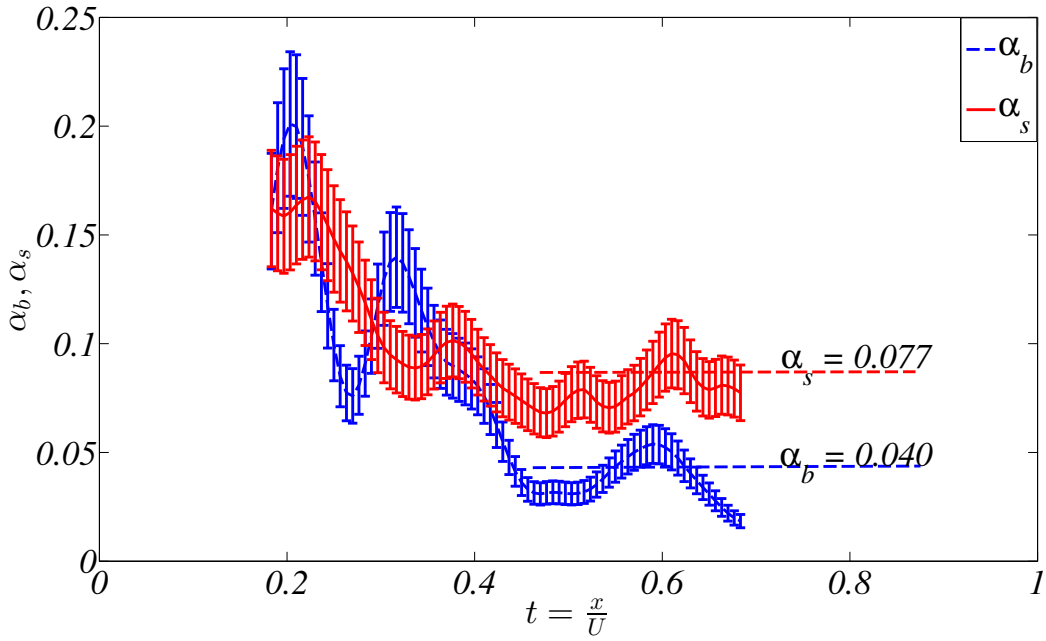

Figure 3.2: The bubble and spike mixing growth rate constant (α_b, and α_s) evolution with time t from the onset of instability for an experiment at Atwood number 0.75, $U = 3\ m/s$.

$$h_b = \alpha_b \; A_t \; g(t - t_0)^2 = \alpha_b \; A_t \; g \; \left(\frac{x - x_0}{U}\right)^2 \tag{3.2}$$

Including the uncertainties due to choosing the correct normalization factor for the volume fraction calculations ($\approx 3\%$ for the bubble, and $\approx 3\%$ for the spike in the mixing width evaluation), the measured asymmetry for the present experiment, $\frac{h_s}{h_b}$ is around 1.6 ± 0.07. The ratio $\frac{h_s}{h_b}$ is different from the actual asymmetry ratio definition $\frac{\alpha_s}{\alpha_b}$. Table 3.1 shows the parameters obtained using both the VO method and the RC method. The asymmetry ratio obtained using the VO and RC method is 1.54 and 1.90, respectively. Mie scattering measurements have shown that the instability growth is quite different close to the walls, and the bubble width observed near the walls is higher compared to the core region in the span-wise direction. Thus, the asymmetry value obtained is small as the mixing width information is span-wise averaged for the visualization technique. The RC method predicted smaller values of $\alpha_{b,s}$ compared to the VO method, as it only considers the local gradients. The VO method fits a parabolic curve for the total time, including the initial regions where the mixing width growth rate is very large. If the mixing width information is available for longer times, the VO method will predict values closer to RC method [57].

3.1.3 Mie scattering

Planar Mie scattering measurements are performed to obtain information about the structure of the developing flow field. It is measured at a plane normal to z (at z = 0.05 m), at two different stream wise locations x = 150 cm and x = 240 cm. Typical flow structures observed at x = 150 cm, are shown in figure 3.3. In this case, the fog is injected into the top stream only. The intensity values are inverted for the image shown in figure 3.3. The black color indicates pure air, the white color indicates pure Helium, and the gray color indicates mixed fluid. The spike structure

is very narrow compared to the bubble structure. The shear created between the narrow falling spikes and wider rising bubbles, leads to the rolling up of the structures. Some of these roll up structures are well defined and some of them are turbulent.

Table 3.1: Growth rate parameter $\alpha_{b,s}$ obtained using both the VO method and the RC method for the experiment at Atwood number 0.73

	α_b	α_s	$\frac{\alpha_s}{\alpha_b}$
VO method	0.061	0.094	1.54
RC method	0.040	0.076	1.90

The shear roll up structure is the main mechanism for molecular mixing between these two fluids. The narrow falling spikes look like dendrites observed in crystal growth. Note that the spike width to the bubble width ratio is very high at this location compared to the span-wise averaged values from the visualization. The plane under consideration is very close to the center of the test section, and far enough from the front and back walls of the test section.

3.2 PIV results

Particle Image Velocimetry (PIV) is implemented for the first time at these Atwood numbers to perform velocity measurements and obtain velocity statistics. The details about the implementation of the technique and the validation procedure is discussed in the Diagnostics section. In these experiments, three cameras (TSI 2 MP PLUS CCD cameras, with 2 Mega Pixel resolution) are mounted on top of each other, so that the measurement window size is large at a particular stream-wise location, as each camera can only focus well on the particles, when the window area is smaller than 35 square inches. This limitation comes from the oil particle size used

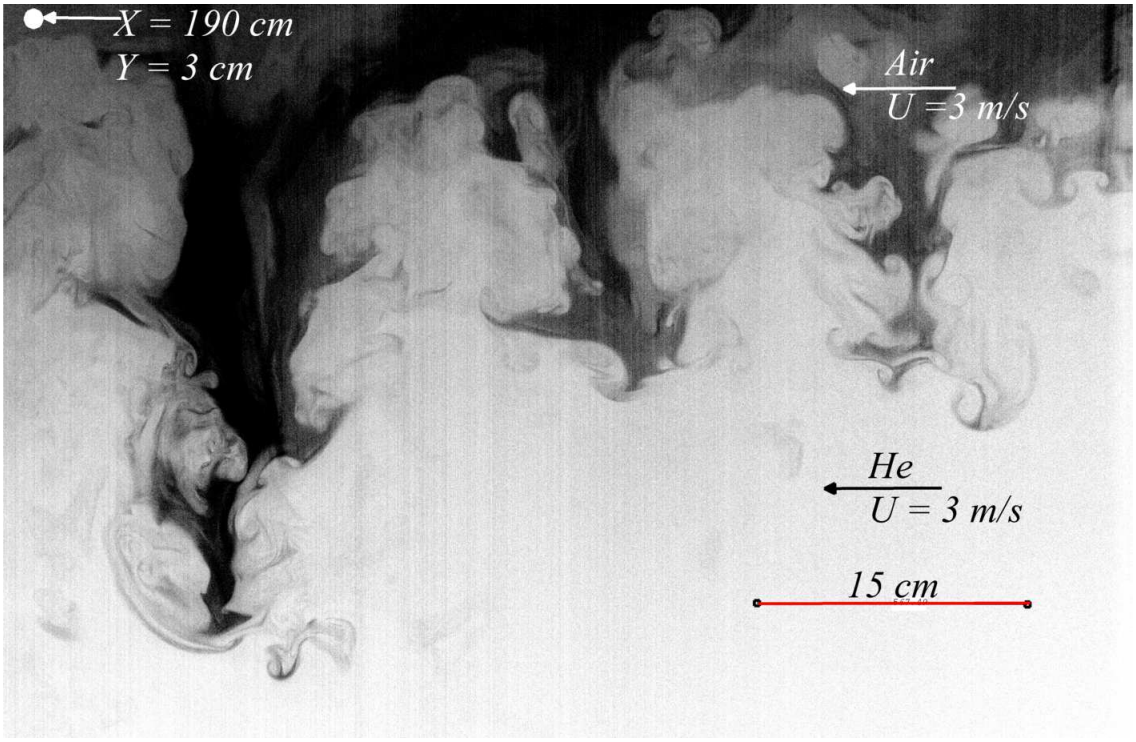

Figure 3.3: Typical instantaneous image taken at x = 150 cm, during an experiment with Atwood number 0.75, and $U = 3\ m/s$.

in the present experiments, and the camera resolution. PIV is performed at four different stream-wise locations (stations), x = 45 cm, 135 cm, 185 cm, and 240 cm named x1, x2, x3, and x4 respectively. At each station, three 2 Mega Pixel Powerview Plus cameras are mounted on each other are used to capture the particle positions for PIV. This provides a window size of 70 square inches approximately (6 inches by 11.5 inches). For each camera, some of the vector information is lost at the edges of the imaging area; thus, some overlapping has to be performed to obtain the vectors at all locations in the mixing layer at that particular station.

3.2.1 Qualitative features

A typical PIV image taken during the Atwood number 0.75 experiment is shown in figure 3.4. The image shown in the figure is a stitched image, acquired using two different cameras with an overlapping field of view. The line across the image is the place where two camera pictures are stitched. The combined imaging area of the two cameras is $\approx$ 7.5 inches tall and 4.5 inches wide. The flow is moving from right to left at the rate of 3 m/s. The imaging location is approximately in the left quarter of the Mie scattering picture shown in figure 3.3. The structure shown in the Mie Scattering image is different than the structure shown here, as both the pictures are taken at different times during different experimental runs. Both flow streams are seeded with glycerin oil particles. The top air-only stream is seeded with more particles than the bottom stream, making it appear brighter in the image. This difference in seeding was not intentional. The bottom stream is almost sealed from the ambient air, and it takes a very small amount of oil particles that are injected just before the sealed louvers on the inlet side of the facility. Ramaprabhu and Andrews [51] used the PIV-S technique, in which they intentionally seeded both the streams with different concentrations of the seeding particles and correlated the measured concentration of seeding particles with the volume fraction. The same principle can be used here. The reduction in light intensity can be correlated with the mixing between the streams. The spike structure shown here has a dendrite like structure as in the Mie-scattering image.

Two consecutive images are taken with a time difference Δt of 250 μs. The second image almost looks like the first image shown in figure 3.4, with some particle movement (order of pixels) due to the time difference. The two images are correlated to obtain the velocity field and other velocity statistics. The vorticity field superimposed

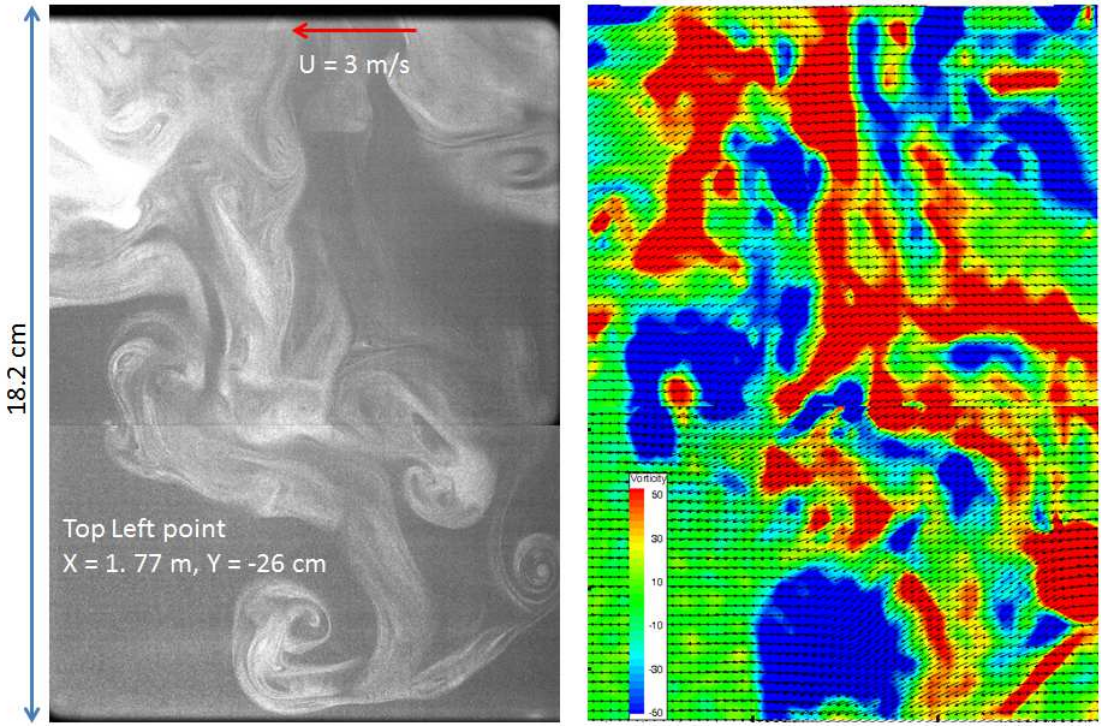

Figure 3.4: PIV image stitched from two cameras at x = 170 cm, during an experiment with Atwood number 0.75, and $U = 3\ m/s$. This location approximately corresponds to the left quarter of figure 3.3

over the vector field for this particular image is shown on the right side of figure 3.4. The vorticity field correlates very well with the structures that appear in the actual image. On the side of the falling spike, three pairs of counter rotating roll-ups are observed at three different cross stream locations. These roll-ups are the result of the deposition of the baroclinic vorticity in the flow field. Almost every clock-wise rotating roll-up structure (blue) has a corresponding counter clock-wise rotating roll-up structure (red) on the other side of the spike. Even the small scale structures (< 1 cm) are resolved relatively well. This fragmented vorticity field clearly outlines the dendrite spike structure in the flow field.

3.2.2 Velocity statistics

In order to obtain velocity statistics for this problem at every station, up to 600 sets of images are taken at the rate of 15 Hz. As discussed in the Diagnostics section, the number of image pairs acquired here are enough to have convergence in the velocity field statistics. The stream-wise velocity u, and cross stream velocity components v are obtained from each image set and velocity statistics, including u', v', $\overline{u'v'}$, and anisotropy tensor b_{ij} are obtained over the entire field of view. The statistics are done over time, and the time co-ordinate in the present convection-type setup corresponds to the spatial coordinate along the mix in the box type conventional systems. Thus the u', v' values correspond to the variation 'along' the mix for the conventional box-type setups.

The u', v' values obtained for the first three stations at x1, x2, and x3 are shown in figure 3.5. All three stations show approximately similar profile shapes for u' , and v', a peak at the center and Gaussian like distributions across the mix. However, it should be noted that the location of the peak of the velocity fluctuation shifts towards the bottom stream as the flow moves downstream. This is another clear indication of the asymmetry observed in the higher Atwood number experiments. The ratio of v' to u' is small during earlier stage at x1, and the ratio is ≈ 2 at the x2, and x3 stations. This type of distribution without asymmetry is observed for small Atwood number experiments [51].

As the vertical velocity fluctuation is the main contributor for mixing growth, the peak values of the vertical (cross stream) velocity fluctuation rms v' at a particular station (x location) can be correlated with the mixing growth rate α, through $v' = \frac{dh_x}{dt}$ [51]. As the mixing width grows quadratically in time, v' has to increase linearly with time. The v' and u' peak fluctuation rms quantities observed at different stream-wise

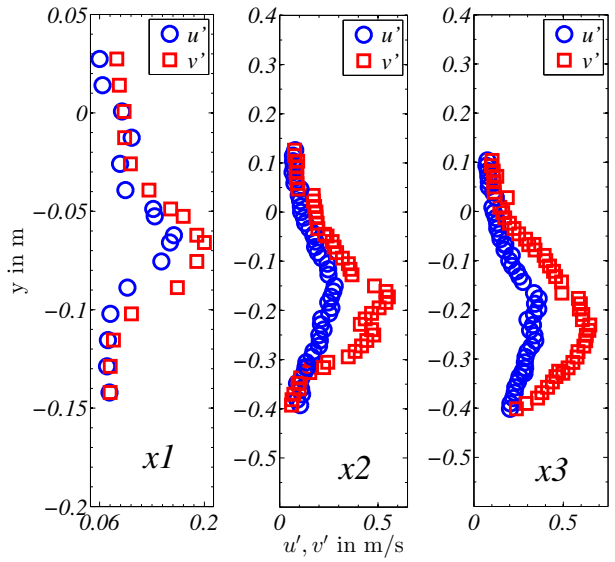

Figure 3.5: Variation of u', v' across the mixing layer at three different stream-wise locations x1 = 45 cm, x2 = 135 cm and x3 = 170 cm from the splitter plate.

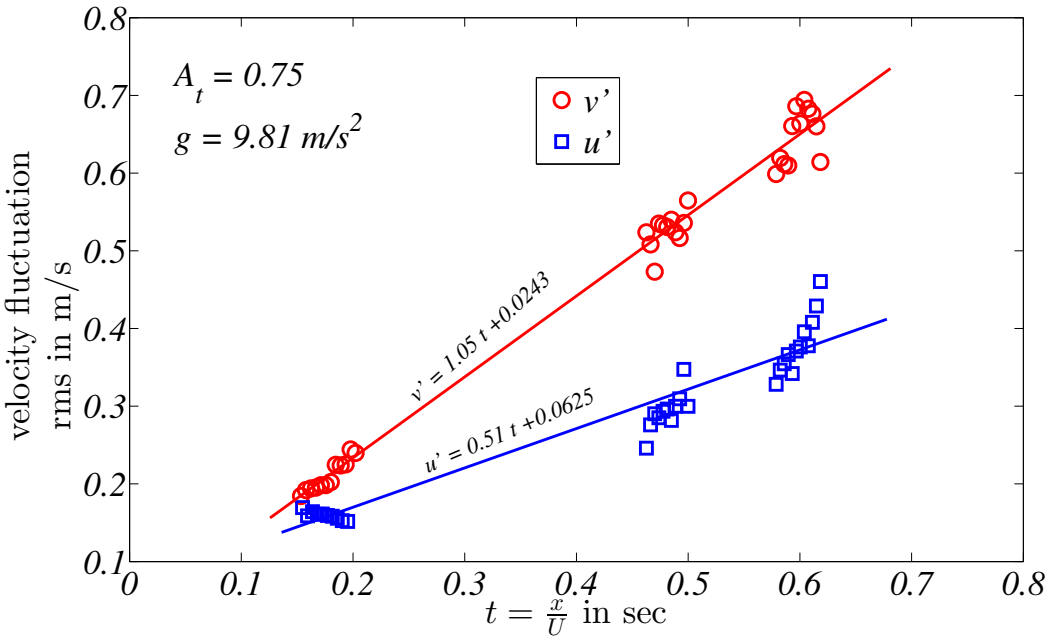

Figure 3.6: Variation of u', v' along the mixing layer at three different stream-wise locations. The curve fit lines for these peak values are also shown.

locations are plotted in figure 3.6. The points correspond to the stations x1, x2, and x3. At each station, the uncertainty in the rms quantities is high at the edges of the PIV image as some particles might have left the area of interest by the time the second laser pulse is generated for PIV. The lines are drawn in the figure to highlight the linear trend of u' and v' in time. The slope of the lines is proportional to the mixing growth rate. The slope of v' is more than two times the value of u', indicating the dominance of the vertical velocity fluctuation over the other fluctuation components in the RTI development.

Using the equations 1.2 and $v' = \frac{dh_x}{dt}$,

$$v' = 2\ \alpha\ A_t\ g\ t = 2\ \alpha\ A_t\ g\ \frac{X}{U} \tag{3.3}$$

The α value calculated from equation 3.3 is the average value of both bubbles and

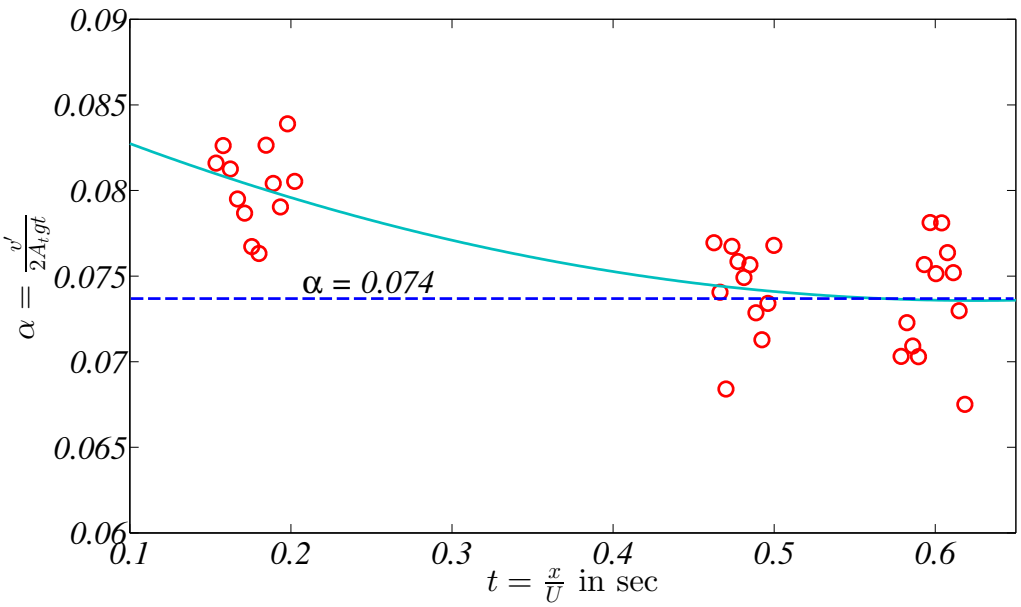

Figure 3.7: Variation of α calculated from $v' = 2\alpha A_t gt$, along the stream-wise direction

spikes. The time t is equated to $\frac{x}{U}$ for the current convective type system. The α value calculated from equation 3.3 is shown in figure 3.7. The value obtained at later times varied between 0.07 to 0.079, with an average value of 0.074. The value obtained here is same as the average value obtained from the VO method. At the station x1, the v' value is slightly higher than the late-time constant value, indicating that the flow has not become self-similar yet at station x1. This trend is also observed in the visualization experiments and in previous low Atwood number experiments [51, 57].

3.2.2.1 Reynolds numbers

Ramaprabhu and Andrews [51] provided different types of length and velocity scales used in defining the Reynolds number

$$\begin{aligned} Re_a &= \sqrt{\frac{gA_t}{6}}\ \frac{2{h_x}^{3/2}}{\nu_{mix}} \\ Re_b &= \frac{h_x v_\infty}{\nu_{mix}} \\ Re_{v'} = \frac{(h_s+h_b)v'}{\nu_{mix}}, h_x &= \frac{h_s+h_b}{2}. \end{aligned} \tag{3.4}$$

$$v_\infty = 0.7\ \sqrt{\frac{A_t\ g\ h_x}{2}} \tag{3.5}$$

Table 3.2: Measured Reynolds numbers at Atwood number 0.75

	Re_a	Re_b	$Re_{v'}$
x1	135	154	176
x2	3640	4170	3950
x3	7920	9080	8100
x4	16850	19300	17380

The mixture kinematic viscosity ν_{mix} is calculated using the equation developed by Wilke [103]. The Reynolds numbers calculated based on the current measurements are shown in table 3.2. At present, the velocity statistics available in the literature are limited to $Re_{v'} < 6000$. The turbulent statistics measurements performed in the current work for the RTI driven flow, are at Reynolds numbers much greater than what has been reported so far.

3.2.2.2 Self Similarity

The terminal bubble velocity v_∞ defined by equation 3.5 is used for normalizing the velocity statistics at small Atwood numbers $< 10^{-3}$ by Ramaprabhu and Andrews [51]. This velocity is calculated by extending the Layzer theory [14] on terminal bubble velocities at infinite density ratios to finite density differences [104]. For finite density differences, Birkhoff [105] showed that the terminal bubble velocity is $v_\infty = 0.5\sqrt{\frac{\rho_1-\rho_2}{\rho_1}gR} = 0.5\sqrt{A_t gR(1+\frac{1}{r})}$, where R is the radius of the cylinder and r is the density ratio $\frac{\rho_1}{\rho_2}$. When $r \sim 1$ for small Atwood numbers less than 10^{-03}, $v_\infty = 0.7\sqrt{A_t gR}$. For higher Atwood numbers, $r \sim \infty$, $v_\infty = 0.5\sqrt{A_t gR}$. Birkhoff's theory [105] predicts how the coefficient of the term $\sqrt{A_t gR}$ varies from 0.7 to 0.5 depending upon the density ratio r. For the present Atwood number, this coefficient value is 0.54. Thus for the current measurements, after replacing the cylinder radius with half the average mixing width $h_x = \alpha A_t g t^2$ [106], the terminal bubble velocity $v_\infty = 0.54\sqrt{A_t g h_x} = 0.38\sqrt{\alpha} A_t g t$ is used as the scaling factor. For the cross stream location at each station, the half mix width h_x, is used a scaling parameter.

The variation of u' and v' across the mix layer at four different stations x1 to x4, normalized with the bubble saturation velocity v_∞ is shown in figure 3.8. As the bubble saturation velocity is constant at a particular station, the variation across the mixing layer would be similar to the profile shown in figure 3.5. All profiles

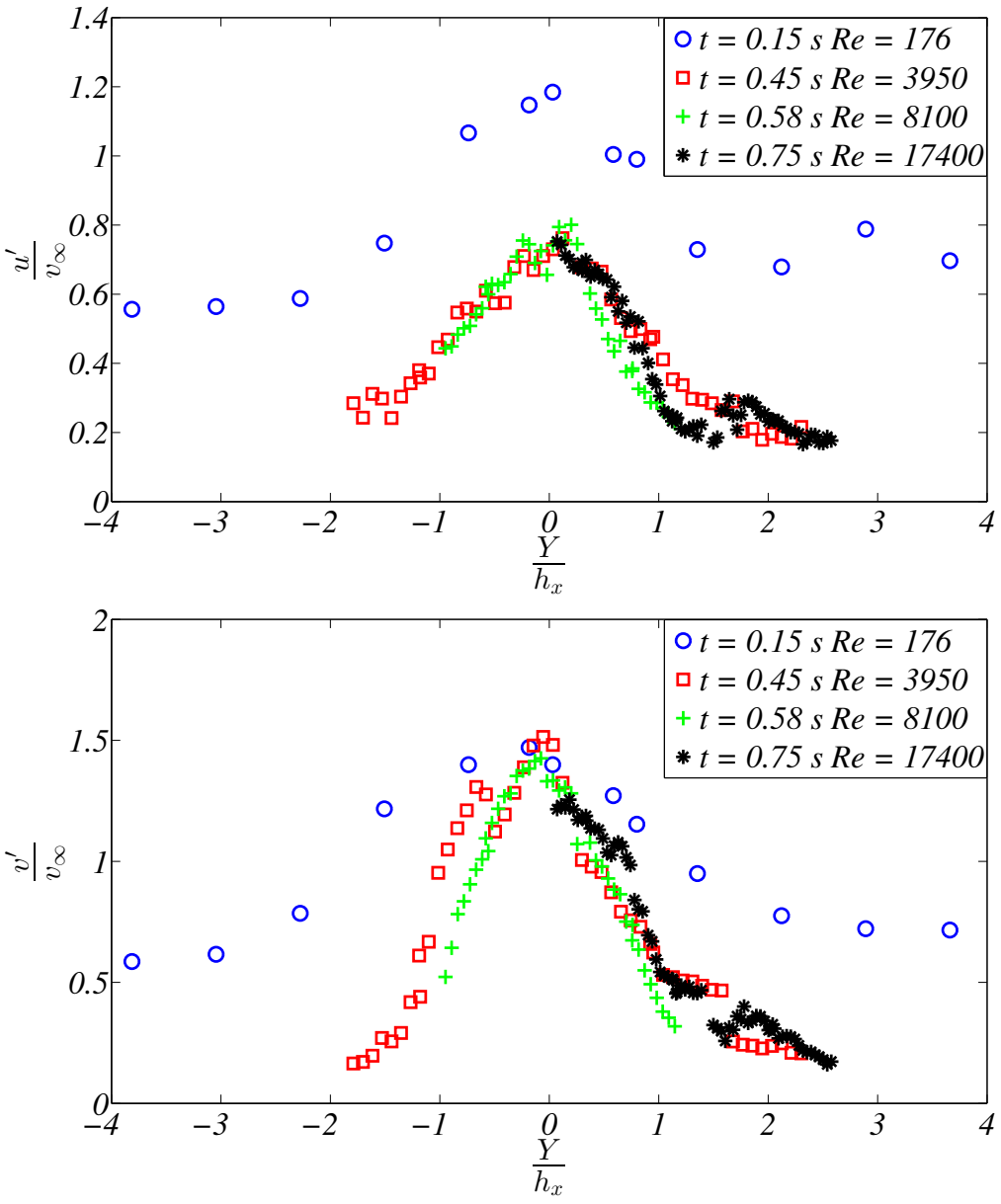

Figure 3.8: u', and v' velocity fluctuations normalized by $v_\infty = \sqrt{\frac{A_t g h_x}{2}}$ variation across the mixing layer, at four different stations along the stream-wise direction x1 to x4.

are Gaussian shaped with a peak at the center of the mixing layer. The x-axis in the figure is translated for each curve, so that the peak of the Gaussian profile is located at $y = 0$ to show the collapse of the curves. For both u' and v' curves, the fluctuation rms measured at station x1 did not collapse well with the other curve. As discussed earlier, at this station the flow has still not developed enough to be considered self-similar. The magnitude of normalized u' fluctuation is also quite high compared to other stations. Overall, the u' variation is little broader compared to the v' variation. This is due to flattening of the Gaussian shaped curve at the edge of the mix layer, because of the presence of larger u' fluctuation in the free stream compared to the other directions. Very good collapse among the u' and v' distributions is observed at stations x2, x3, and x4, indicating the parameters chosen for the scaling analysis seems to be accurately reflecting the self-similar flow characteristics. The normalized peak value for v' is ≈ 1.5 for most of the stations. This value indicates that the spike contribution to the v' is twice as much than the bubble, so that the average is 1.5. For small Atwood numbers, v' values normalized by the Birkhoff relation (equation 3.5), have shown a peak value of 1.0 indicating equal contributions from bubbles and spikes [51].

3.2.2.3 Probability Density Functions, Skewness, and Kurtosis

The probability density function (PDF) indicates the probability of a variable having a particular value. The PDF is defined such its the integral is equal to one for the values from $-\infty$ to $+\infty$. The velocity PDF indicates the scale contribution to the total rms fluctuation at that location. The PDF shown here correspond to fluctuations in time at a particular spatial location. In the conventional box-type systems, this PDF will indicate the probability of finding a particular velocity fluctuation scale along the mix. Figure 3.9 shows the PDFs measured at three different cross stream

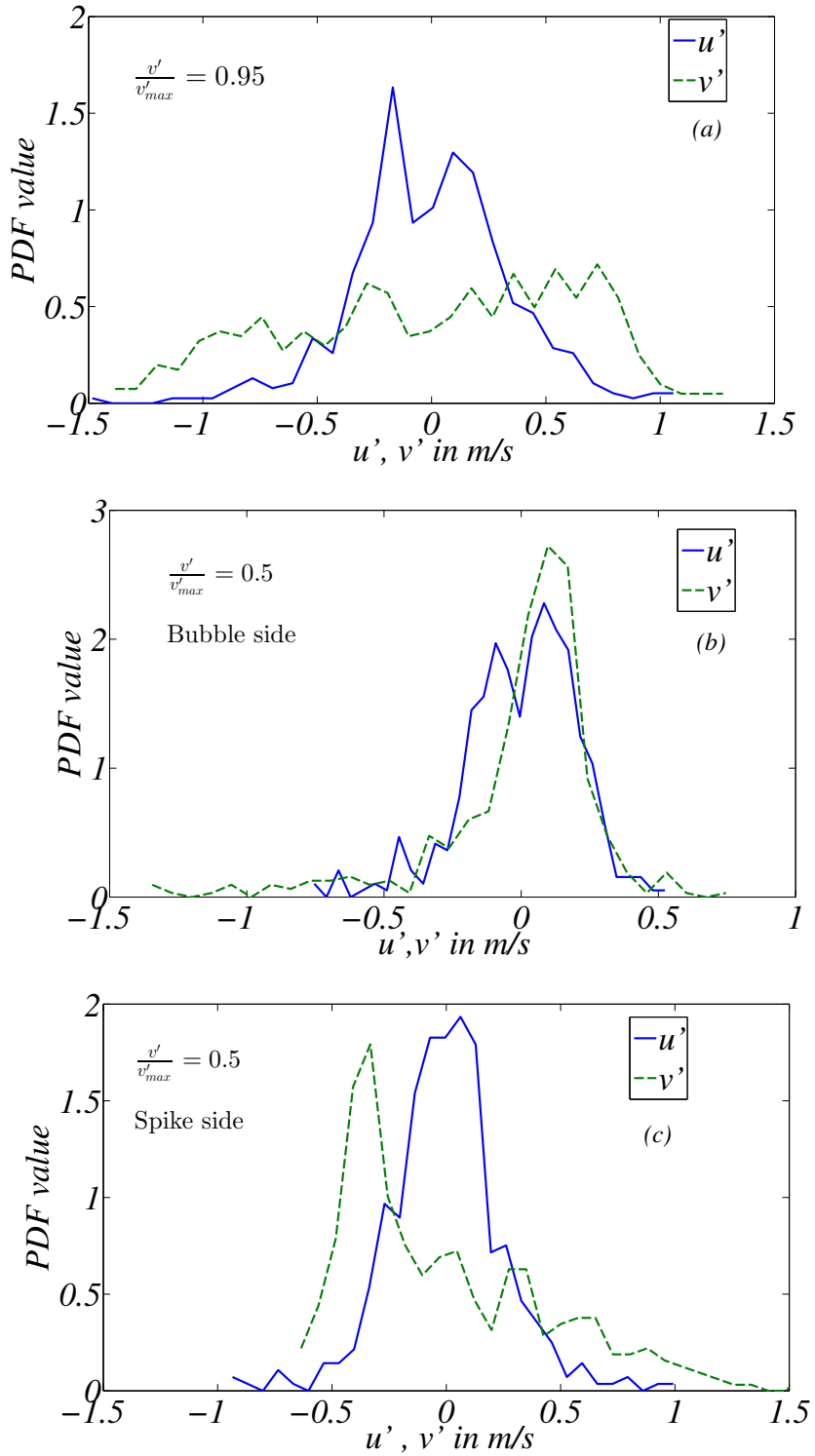

Figure 3.9: Probability Density Functions (PDF) of the u', v' velocity fluctuations at three different cross stream locations across the mixing layer at the x3 station, (t = 0.58 s, $Re_{v'} = 8100$).

(y) locations at the station x3. Figure 3.9 (a) shows the PDF distribution of the velocity fluctuations at a location close to the point where the fluctuation rms is maximum. At this point, the u' velocity PDF has a Gaussian distribution with a peak near zero. The v' velocity PDF has a plateau like distribution, with each scale contributing equally to the rms fluctuation. The u' PDF has a Gaussian like behavior at all three locations. The v' PDF is skewed towards the side, depending upon where the measurement is made. For example, on the bubble side, the v' PDF peak is skewed towards the positive side of the fluctuation and it is skewed towards the negative side of the fluctuation on the spike side. Figure 3.9 shows two such distributions on the bubble and spike side of the mix at station x3. Both the v' PDFs have long tails on the opposite side.

This behavior of u' and v' velocity fluctuations can be quantified through the statistical parameters called skewness, and kurtosis. skewness (S) and kurtosis(K) are the third and fourth order moments of a statistical quantity about its mean. For the variable u', skewness and kurtosis are defined as $S_u = \frac{\overline{u'^3}}{\sigma_u^3}$ and $K_u = \frac{\overline{u'^4}}{\sigma_u^4}$, where σ_u is the standard deviation of u'. Similar definitions can be made for other variables. Skewness indicates how the PDF is biased towards one side, i.e., it is positive when the left side of the PDF has a longer and fatter tail, and it is negative when the right of the PDF has a longer and fatter tail. For a Gaussian distribution, the skewness is equal to zero. Similarly, kurtosis indicates the peakedness of the PDF distribution. If the PDF has a wider and smoother peak, the kurtosis would be $\approx$ of 3. If the PDF has a sharper peak, it kurtosis value would be very high. If the PDF has a broader plateau like distribution, the kurtosis would be smaller than 3. For a Gaussian distribution, the kurtosis is equal to 3.

The skewness and kurtosis values for the u', and v' velocity fluctuations across the mixing layer at station x3 are shown in figure 3.10. For u' the skewness ≈ 0,

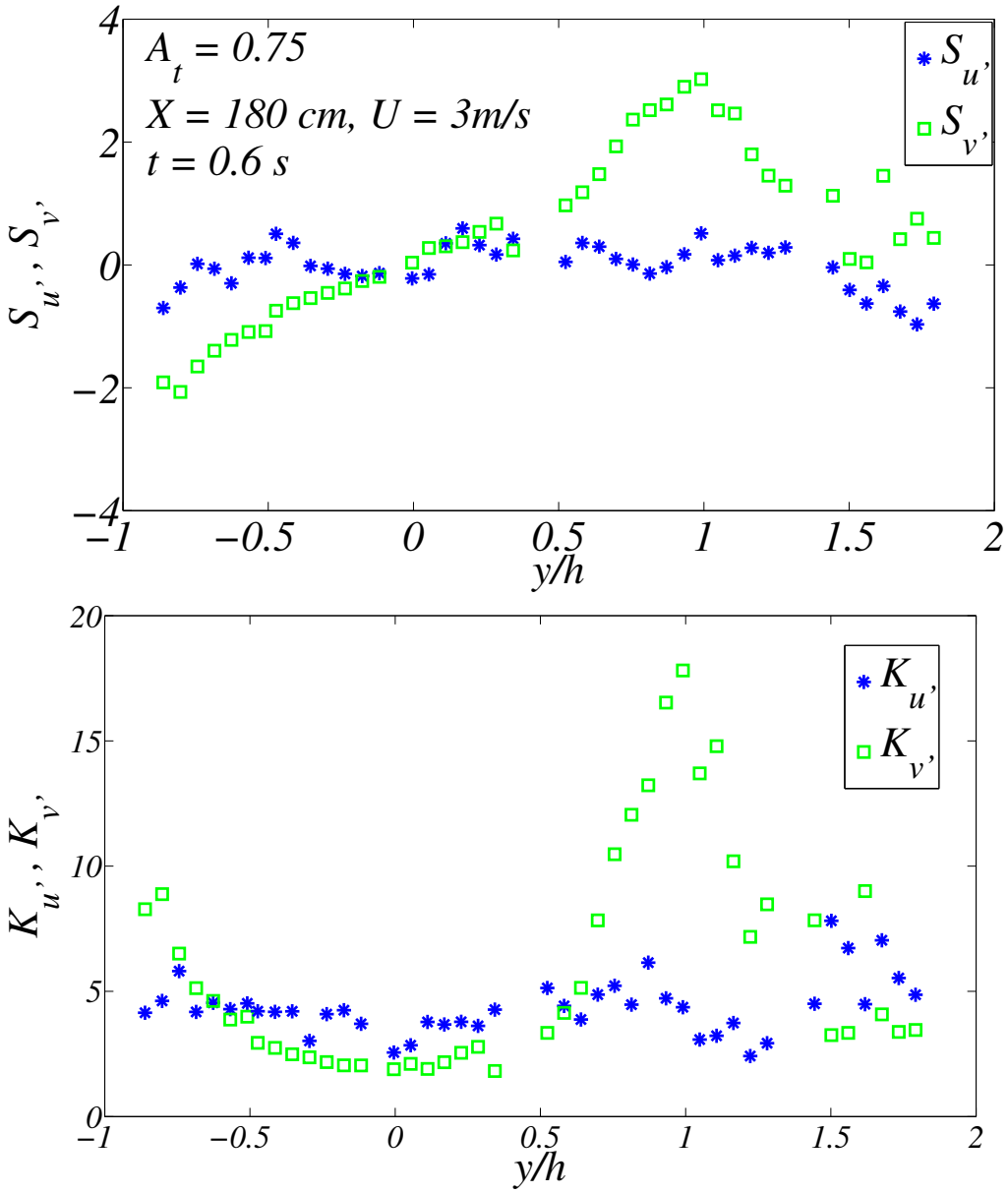

Figure 3.10: Skewness and kurtosis of the velocity fluctuations across the mixing layer at x3 station, (t = 0.58 s, $Re_{v'} = 8100$).

and the kurtosis value is ≈ 3 throughout the mixing layer, indicating a Gaussian like distribution everywhere. For v', the skewness is negative on the on the spike side and is positive on the bubble side. The skewness is close to 3 at the edges of the mix layer. The skewness falls to zero away from the edge of the mixing layer towards the free stream. The kurtosis value for v' at the center of the mix, where the fluctuation rms is high, is ≈ 1.9, confirming a plateau-like distribution of the PDF. Like skewness, the kurtosis peaks at the edges of the mix due to the sharpness of the PDF. Again this peak in kurtosis falls to the value of 3 in the free stream.

3.2.2.4 Anisotropy

The anisotropy tensor, $b_{ij} = \frac{\overline{u_i u_j}}{\overline{u_l u_l}} - \frac{\delta_{ij}}{3}, k = \frac{1}{2}(\overline{u'^2} + \overline{v'^2} + \overline{w'^2})$, is an important parameter for turbulence modeling purposes [47, 107]. The individual components b_{uu}, b_{vv}, b_{uv} are defined

$$b_{uu} = \frac{\overline{u'^2}}{2k} - \frac{1}{3}, b_{vv} = \frac{\overline{v'^2}}{2k} - \frac{1}{3}, b_{uv} = \frac{\overline{u'v'}}{2k}. \tag{3.6}$$

Figure 3.11 shows the anisotropy tensor components measured across the mixing layer at two different stations x2 and x3. For the calculation of these components, the span-wise velocity fluctuation rms (w') is assumed to be equal to the stream-wise velocity fluctuation rms (u'). This assumption is made in the earlier investigation and shown to be true [51, 57]. The hot wire measurements made at these stations using a three wire probe also confirm this assumption at stations x2 and x3. At x1, the flow is very two-dimensional and this assumption is not valid. The b_{vv} value stays constant around 0.35 in the core of the mixing layer and drops to zero at the edges of the mix. This trend for b_{vv} is observed at stations x2 and x3. The component b_{uu} also remained constant at a value of -0.15 in the core of the mixing layer and

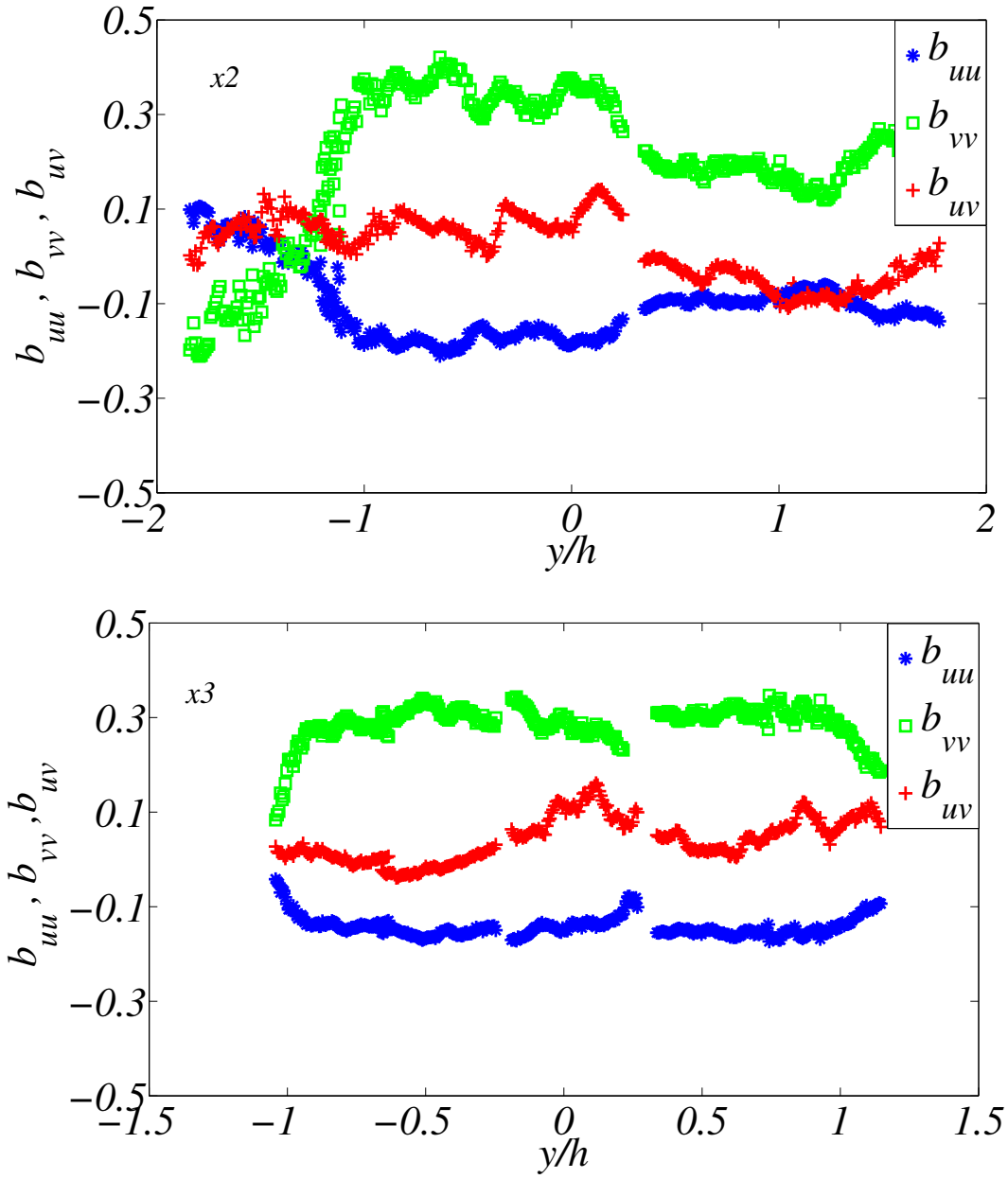

Figure 3.11: Anisotropy tensor components b_{uu}, b_{vv}, and b_{uv} across the mix layer at station x3 , (t = 0.58 s, $Re_{v'} = 8100$)

started rising at the edge of the mix layer, as u' is large in the free stream compared to all other components. The component b_{uv}, which is large in shear flows, is zero throughout the mixing layer except at the center, where it shows a marginal increase and drops back to zero quickly.

3.3 Hot wire results

The present hot wire diagnostic has been explained in the Diagnostics section. This technique measures the instantaneous density and velocity component values simultaneously at a particular point in the mixing layer. The PIV technique only gave the detailed field-wise information about velocity components. The hot wire technique measures the velocity and density components simultaneously, which enables us to make turbulent mass flux calculations, which would be the main driving potential for the RTI flows. In this section, we focus on the density statistics measured from the density probe. Although other information including mass fluxes can be calculated with the available information, that part of the work is left for future investigation for these high Atwood number experiments.

3.3.1 Density PDF

Instantaneous density values are obtained from the density probe. At stations x2 and x3 the probe is moved in steps of one inch during the experiment. The density PDF observed at three different cross stream (y) locations at the x3 station are shown in figure 3.12. The $Vf_2 = 0.5$ curve is the PDF curve at a location where the density is the average of both streams. This location has not coincided with the location where the velocities are maximum. This location is ≈ 2.5 inches above the maximum fluctuation point at this station. The volume fraction of the bottom stream fluid is denoted by Vf_2. The $Vf_2 = 0.65$ PDF curve is at a location where the velocity fluctuation is highest at this station. At this location, it is more bubble dominant.

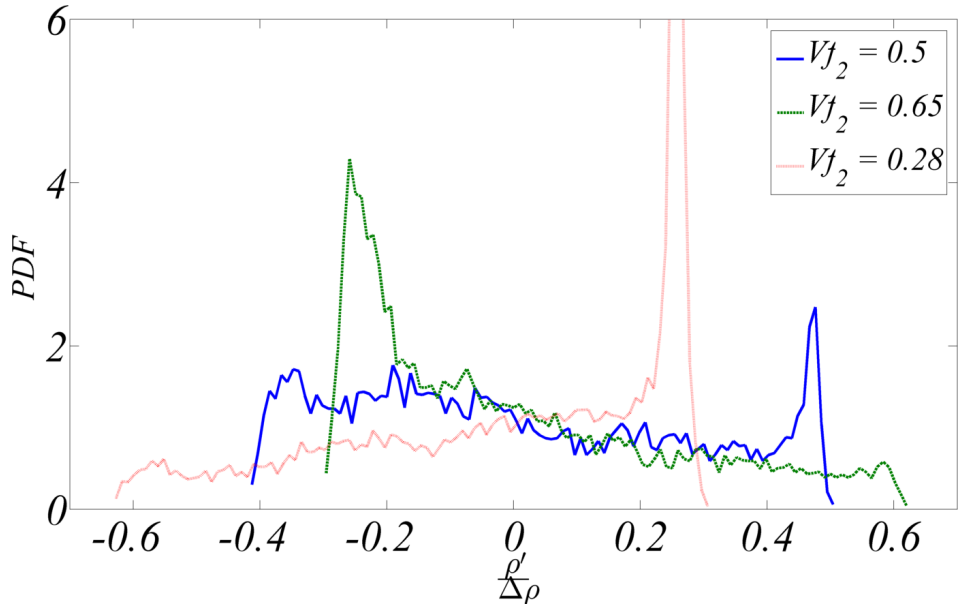

Figure 3.12: Density PDF calculated at three different y locations at the x3 station, (t = 0.58 s, $Re_{v'} = 8100$)

The red $Vf_2 = 0.28$ curve corresponds to a location where the flow is spike dominated. For the $Vf_2 = 0.5$ location, the PDF distribution shows two small peaks at the edges, similar to small Atwood number experiments. The distribution of the mixed fluid is relatively flat in the middle of the curve, indicating that the probability of finding a fluid pocket with any volume fraction is same.

3.3.2 Molecular mixing parameter

Danckwerts [108] quantified the amount of molecular mixing between two different materials by the intensity of segregation $1 - \theta$. The parameter θ is defined by

$$\begin{aligned} \theta &= 1 - \frac{B_0}{B_2} \\ B_0 = \lim_{T\to\infty} \frac{1}{T}\int_0^T \frac{(\rho-\overline{\rho})^2}{(\Delta\rho)^2}dt; \qquad B_2 &= \overline{f_1 f_2} \\ \overline{f_1} = \frac{1}{T}\int_0^T \frac{\rho-\rho_2}{\Delta\rho}dt; \qquad \overline{f_2} &= 1 - \overline{f_1}. \end{aligned} \tag{3.7}$$

and was first adapted to RTI flows by Youngs [109], and subsequently used by others to quantify molecular mixing. Inside the mixing layer, θ is equal to 1 when both fluids are completely molecularly mixed, and θ becomes zero when two fluids are immiscible. In equation 3.7, ρ is the instantaneous density at a location, whereas $\overline{\rho}$ is the time-averaged density for a total measurement duration of T. The instantaneous density values are obtained from the density probe. The top stream volume fraction f_1 is defined by equation 3.7, and ρ_2 is the bottom stream fluid density. The parameter B_0 is the non-dimensional autocorrelation of the density, and B_2 is the same auto correlation for immiscible fluids. In the equation 3.7, $\overline{f_1}$ is the time averaged top stream volume fraction and $\overline{f_2}$ is the time averaged bottom stream volume fraction. The value of B_2 is typically close to its maximum of 0.25 at the mixing layer centerline for RTI mixing, as equal amounts of molecularly mixed top stream and bottom stream fluids are observed; B_0 measures the rms density fluctuation, and becomes equal to zero either when the fluids are completely mixed, or at the edge of the mix where only one fluid is available.

Table 3.3: Measured molecular mixing parameter θ at the x3 station at Atwood number 0.75.

	$\overline{f_2}$	B_0	B_2	θ
Y1 = 5”	0.30	0.067	0.227	0.71
Y2 = 3”	0.44	0.077	0.250	0.70
Y3 = 2”	0.50	0.070	0.247	0.71
Y4 = 1”	0.56	0.068	0.240	0.72
Y5 = 0”	0.62	0.051	0.220	0.76

For the present case, the measured values of θ and the related parameters are tabulated in table 3.3. The distances from the maximum velocity fluctuation point

are indicated in inches at this station. The mean volume fraction seems to vary linearly with distance by correlating the increase in $\overline{f_2}$ values with distance. Both B_0 and B_2 values are highest at the $\overline{f_2} = 0.5$ location. The value of B_2 is 0.25 at this point, indicating that the probe sensed both the streams an equal number of times. The value of θ remained constant through out the mix, showing a similar behavior to small Atwood number experiments [57].

4. COMBINED RAYLEIGH - TAYLOR AND KELVIN - HELMHOLTZ INSTABILITY [1]

The third objective of the present study is to obtain mixing growth rates and velocity statistics the combined shear (Kelvin - Helmholtz instability or KHI), and buoyancy (Rayleigh - Taylor instability or RTI) experiments. The effect of KHI on the development of RTI is studied at four different Atwood numbers ($A_t < 0.2$). The details of the experiments performed with their names for this combined instability (KH + RT) are shown in table 4.1.

Table 4.1: Experimental parameters for the different sets of combined Rayleigh - Taylor and Kelvin - Helmholtz (KH + RT) instability experiments performed in the present work

Case	A_t	U_1 (in m/s)	U_2 (in m/s)	ρ_1 (in kg/m^3)	ρ_2 (in kg/m^3)
A1S0	0.035	0.63	0.63	1.180	1.1
A1S1	0.035	0.85	0.63	1.180	1.1
A1S2	0.035	1.03	0.63	1.180	1.1
A2S0	0.073	1.31	1.34	1.188	1.027
A2S1	0.078	1.66	1.26	1.186	1.014
A2S2	0.078	2.02	1.26	1.186	1.014
A3S0	0.122	1.51	1.61	1.190	0.931
A3S1	0.127	1.98	1.55	1.195	0.926
A4S0	0.157	1.71	1.75	1.185	0.864
A4S1	0.159	2.39	1.71	1.191	0.865

Experiments A1S0, A1S1 and A1S2 are performed in the two layer gas tunnel facility, and all other cases are performed in the multi layer gas tunnel facility. For

[1]Parts of this section including figures 4.1, 4.4, 4.11 have been reprinted with permission from "Effect of shear on Rayleigh-Taylor mixing at small Atwood number" by B. Akula, M. J. Andrews, and D. Ranjan, 2013. Physical Review E *87*, 033013, Copyright [2013] by American Physical Society.

the experiments in the multi-layer gas tunnel, the setup is for three layers. The middle and bottom layer are used for the current experiments. The top layer velocity is set equal to the middle layer velocity, so that it does not effect the mixing between the other two streams. Visualization and S3WCA are used to measure the mixing width as well as instantaneous velocity and density fluctuations for cases A1S0, A1S1, and A1S2. In addition to these two diagnostics, two dimensional PIV measurements are conducted to acquire the flow field information of the stream-wise (u) and cross stream (v) velocity fluctuations for all other cases. For all the experiments presented here, Helium is injected into the bottom stream to provide the density difference between the streams. Before the start of the experiment, the velocity of the bottom stream is intentionally kept smaller than the indicated value in table 4.1 to compensate for the velocity increase due to injection of Helium and Nitrogen mixture. The velocity increase due to Helium and Nitrogen mixture injection is estimated priori by Amagat's law [110], and the actual measurements agree with the Amagat's law estimation. A large number of measurement points are considered in the cross stream direction for the small Atwood number cases $A1S0 - S2$, as it required a lesser amount of Helium to perform those experiments.

In the next section, the visualization results are discussed for the combined KH+RT instability. In the section after that, the velocity statistics obtained including histograms, spectra, and turbulent budgets are discussed.

4.1 Visualization results

4.1.1 Effect of fog injection

The details of the visualization diagnostic are given in section 2.3.1. The signal from the fogged stream is small at the edge of the mixing layer and it is difficult to obtain the 95% volume fraction point location. Therefore, each experiment is

repeated two times with fog particles in a different stream each time. Fog injection has a small effect on the Atwood number. For the present cases, fog injection in different streams brings an extra uncertainty of 5% for $A1$, 2.8% for $A2$, 2.3% for $A3$, and 1.9% for $A4$, respectively. These percentages are calculated based on the difference in the Atwood number change divided over the average Atwood number. The Atwood number is calculated based on Amagat's law by measuring the mass flow rate of fog fluid and converting it into volumetric flow rate (≈ 4.6 kg/m^3).

4.1.2 Flow structures

Typical images taken during RTI, KHI and combined instability experiments at Atwood number of 0.035 are shown in figure 4.1. These experiments are performed in the two layer gas tunnel facility. The bottom stream is injected with fog particles and illuminated from the back using diffused light from rows of fluorescence tube lights. The 5% and 95% volume fraction contours of the bottom stream are shown on the right hand side of figure 4.1. The distances to these contours from the center of the mixing layer are the bubble width h_b, and spike width h_s respectively. The total mixing width is the sum of these two widths.

The volume fraction profile across the mixing layer is linear in the core and varies like the error function distribution at the edge of the mixing layer [20, 111]. The criterion for calculating the mixing width is very important, as mixing width value is very sensitive to the choice of threshold values at the edge of the mixing layer. Kucherenko *et al.* [112] noticed a difference of 20% change in the α_b value by choosing 2% - 98% levels instead of 0% - 100%. Choosing between 1% and 5% can cause a difference as high as 28% in obtaining the h_s and h_b values. This difference goes down to 15% between 5% and 10% choice of cut-off value. For the present study, 95% and 5% volume fraction points are chosen as the criterion for calculating the

mixing width.

For the buoyancy only RTI case 4.1 (a), the mixing layer is very diffuse and not many structures are observed at early times closer to the splitter plate. This region, which starts from the edge of the splitter plate to the location 30 - 36 cm downstream of the splitter plate where the first large mushroom-like structure is visible, corresponds to the linear growth regime and part of the bubble merger/bubble competition regime. By the end of this region, longer wavelength structures tend to dominate the mixing either through merging of smaller wavelength structures [19, 113], or through the acceleration in the growth of longer wavelength structures in the initial conditions [26]. As discussed in later, the two layer gas tunnel facility has initial wavelength spectra dominated by wavelengths corresponding to splitter plate vibrations and the plastic perforated plates which are used for mounting wire screens. After the initial diffuse region, successively larger structures develop and dominate the mixing region through non-linear interactions. The flow at later times (80 - 100 cm away from splitter plate) is characterized by the presence of vertical plume like structures in the flow field. These plumes contain mushroom-like structures arising from the shear between falling spikes and rising bubbles. Small scale features appear on these large scale structures at late times, and eventually leads to fragmentation of the large coherent structures. The flow also becomes three dimensional after 80 - 100 cm away from splitter plate, and the large scale structures are not clearly visible in the visualization image due to the span-wise averaging of the structures. At the edge of the splitter plate, $\approx$ 25-30 wavelengths are visible in the span-wise width of 60 cm (not shown). These structures grew independently until 70 - 80 cm downstream of the splitter plate. After this point, these wavelengths become large enough to combine with each other and make the flow three dimensional. At the end of the tunnel, only 3 - 4 large scale wavelengths are visible in the span-wise direction, and

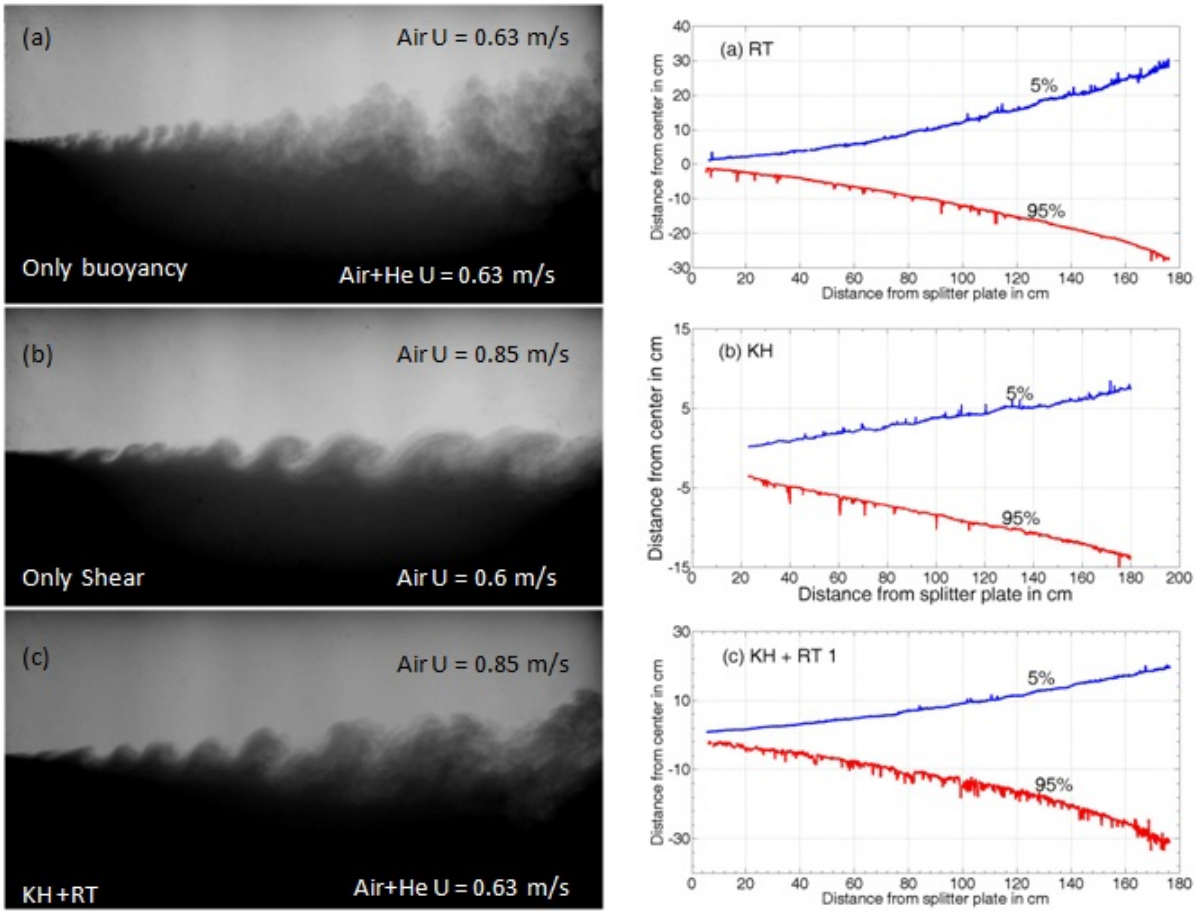

Figure 4.1: Typical images taken during the visualization experiments with fog injected into the bottom stream with corresponding stream velocities indicated on the images (a) RTI only experiment A1S0 (b) KHI only (c) RTI + KHI experiment A1S1. Both bubble and spike mixing widths obtained from an ensemble average of 200 images is also shown on the right side of the corresponding case. The fluids are moving from left to right, with the left most side of the image 20 cm from the splitter plate. The image size is 160 cm $\times$ 80 cm.

contain many more small scale structures on them.

For the shear only case or the KHI case 4.1 (b), the span-wise roll-ups are the main characteristic of the flow. The structures are referred to as the span-wise roll-ups, as the rolling structure's vorticity is aligned with the span-wise direction or the direction perpendicular to the plane of the image. The number of structures are large closer to the splitter plate and the number of these roll-ups is reduced with downstream distance through 'vortex-pairing' [65]. The vortex size increases with downstream distance due to this vortex-pairing phenomenon. Although, the flow has three dimensional features on top of these vortex roll-up tubes [69], they are not large enough to affect the vortical roll-up structures. These structures are largely two dimensional throughout the length of the channel for the present experiments. After long enough time, the stream-wise vortices start to affect the roll-up structure causing the flow to develop three dimensionality and finally transition towards turbulence. Another characteristic that is apparent from the image analysis is related to the flow asymmetry. As the flow moves downstream, the fast moving top stream constantly pushes on the slow moving bottom stream, causing the mixing centerline to move below the geometric centerline.

For the combined KHI+RTI, the flow is initially dominated by the vortical roll-ups and the flow evolves into RTI type structures at later times. When the shear value is small, the rollup structures get stretched and the bubble and spike evolution of RTI is observed.

For the combined instability experiment A1S1, KHI + RTI at $A_t = 0.035$, the flow is initially dominated by the span-wise vortical roll-ups formed due to the shear between the streams. Closer to the splitter plate, these structures are larger in size compared to the case with the same amount of shear present in the flow. These structures are stretched faster due to buoyancy, and three dimensionality is noticed

earlier than in the KHI only case with same amount of shear. The vortical structures are stretched apart by the buoyancy force and the plume-like structure dominates after a certain point. From this point onwards, the flow structures and their growth exhibit RTI-like characteristics. When the shear is high enough, the roll- up structure persists for longer in time and the transition to RTI might not be observed. In this scenario, applying the same terminology of bubbles and spikes for RTI is not strictly correct. For RTI, the bubble mixing width is defined as the distance between the geometric centerline and the 5% volume fraction contour. The same definition is extended to the combined (KH+RT) instability experiments.

The next set of combined instability experiments (A2S1-A2S2) are performed in the new multi-layer gas tunnel facility. The details about the back-lighting system and other details about the new tunnel visualization technique were presented in the Diagnostics section. Typical images taken during the experiment, after correcting for the background variation are shown in figure 4.2. The structures show very similar characteristics as in the old two layer gas tunnel facility. For the RTI only case (A2S0) in figure 4.2 (a), the diffuse layer (the initial mixing region, before any structures start to appear) is longer than the diffuse layer seen in the older setup 4.1 (a). Unlike, the older setup, this setup does not have any splitter plate vibrations, and the major source of perturbations are the screens which will induce very small perturbations in the flow in accordance with the mesh size.

4.1.3 Mixing widths

4.1.3.1 Growth rate parameter for KHI

In the case of KHI, the mixing widths are defined based on the visualization. As explained in Section 1.3, the mixing width obtained through visualization δ_{viz} is more than twice the value obtained from velocity measurements or the vorticity thickness

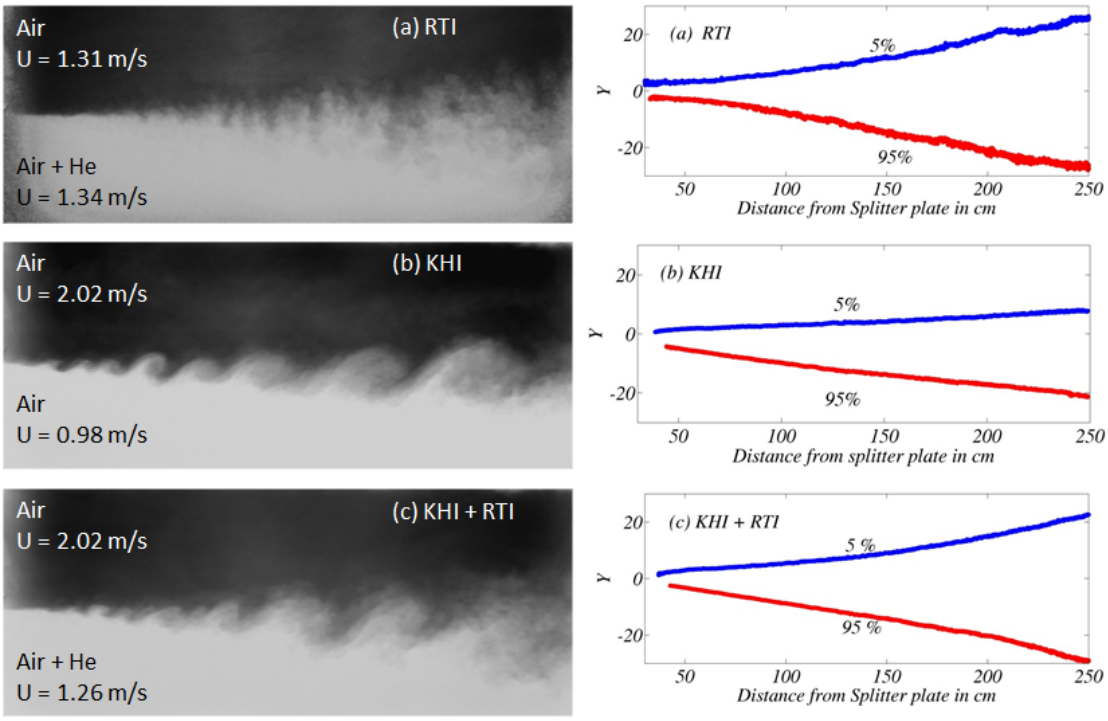

Figure 4.2: Typical images taken during the visualization experiments with fog injected into the bottom stream with corresponding stream velocities indicated on the images (a) RTI only (b) KHI only (c) RTI + KHI. Both bubble and spike mixing widths obtained from the ensemble average of 120 images at 2 images per minute for (a), 500 images at 7 images per second for (b) and (c), are also shown on the right side of the corresponding case. All the experiments with RTI correspond to an Atwood number of 0.075 (A2). The left most side of the image location is 20 cm away from the splitter plate. The image shown is cropped to 250 $cm \times 92$ cm.

δ_w. The self-similar mixing width δ_{viz} can be correlated to stream-wise distance from the splitter plate x, velocity difference $\Delta U = U_1 - U_2$, mean velocity U, and the growth parameter β through equation 4.1.

$$\delta_{viz} = \beta \frac{(x - x_0)\Delta U}{U} \Rightarrow \beta = \frac{d\delta_{viz}}{dx} \quad \frac{U}{\Delta U} \tag{4.1}$$

The virtual origin x_0 is eliminated from the mixing width expression by taking the derivative with respect to x. Many experimental and numerical investigations

reported different values for β, falling in the range $0.12 - 0.23$. Different sets of experiments are performed in the present setup to check for the value of β. The values obtained with different sets of U, and ΔU values are shown in table 4.2.

Table 4.2: Value of β for different KHI only cases with δ_{viz} calculated from 95% and 5% volume fraction contours using equation 4.1.

U	ΔU	$\frac{U}{\Delta U}$	β
Multilayer gas tunnel			
1.90	1.00	1.9	0.15
1.64	0.76	2.15	0.15
2.32	0.94	2.46	0.17
2.01	0.72	2.80	0.18
2.05	0.70	2.93	0.19
1.46	0.40	3.65	0.19
1.77	0.43	4.10	0.21
1.87	0.44	4.25	0.21
1.67	0.29	5.74	0.21
1.98	0.26	7.62	0.35
1.73	0.16	10.8	0.33
1.56	0.11	14.1	0.33
Two layer gas tunnel			
0.75	0.23	3.26	0.21
0.83	0.40	2.07	0.17

For most of the pure shear experiments (KHI case), when the ratio $\frac{U}{\Delta U}$ is less than 5, the value of β falls in the range $0.15 - 0.21$. At very high velocity ratios greater than 5, the value of β is very large. It is possible that the diffusion of fog particles might be dominating the mixing compared to the mixing due to the velocity difference, especially at these low average velocities less than 2.5 m/s. The value of β is in the range observed by other experimental investigations [72]. However, the δ_{viz} measured by other investigators is based on 99%, and 1% volume fraction contours.

If the same definition is extended to the current measurements, then the measured value of β would lie in the range $0.21 - 0.3$. This extension is done assuming the error function distribution of the volume fraction profile [70, 72], as it is difficult to obtain 99% and 1% volume fraction contours from the present experiments. The value of β increased with $\frac{U}{\Delta U}$. The range of values for β is consistent for both the experimental setups, even though the initial conditions are quite different for both setups.

4.1.3.2 Growth rate parameter for RTI

The two layer gas tunnel facility was used by previous researchers [55, 59] to obtain the mixing width information and the growth rates. Mixing growth rate parameters $\alpha_{b,s}$ can be calculated by different methods. The virtual origin method was used by Snider and Andrews [25] for the water tunnel facility. The equation for α_b (equation 1.2) is written again with the virtual origin x_0, as in equation 3.2. The parameters $x_0, and \alpha_b$ are chosen such that the mixing width becomes zero at x_0, and α_b fits the equation to the measured mixing width with least possible error through regression analysis. The value of x_0 is negative for their experiments. This virtual origin method account for the splitter plate wake effects. Ristorcelli and Clark [102] used a ordinary differential equation to calculate the growth rate parameter α_b. Banerjee *et al.* [57] have shown that both methods lead to the same value of α_b. The value of α_b obtained from two-layer gas tunnel facility is $\approx 0.07 \pm 0.008$ for Atwood numbers 0.04, 0.1, 0.26, and 0.47 [57].

Bubble and spike mixing widths are obtained using the same criterion used for two layer gas tunnel experiments. Bubble widths obtained for the cases A2S0, A3S0, and A4S0 are shown in figure 4.3 against the quantity $A_t g(t - t_0)^2$. The growth parameter α_b is calculated from the virtual origin technique. The values of t_0 are different for all of the cases. The value t_0 is calculated such that the error in making

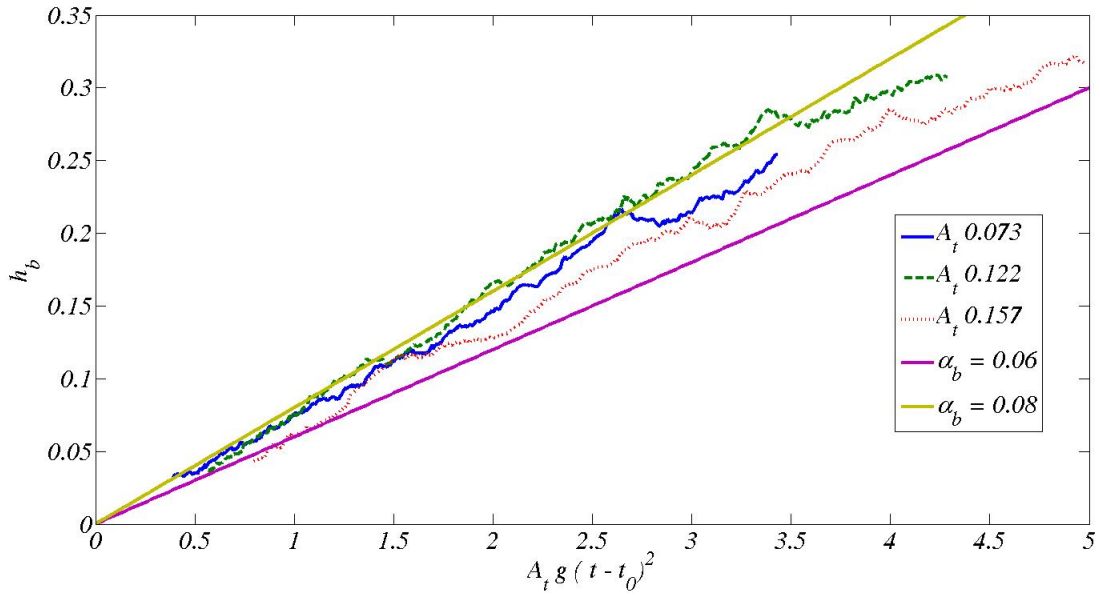

Figure 4.3: Bubble mixing width variation with $A_t g(t-t_0)^2$ for three different Atwood number experiments. Note that the value of t_0 is different for the three cases, and the time t is calculated using Taylor's hypothesis $t = \frac{x}{U}$. Lines corresponding to $\alpha_b = 0.06$ and $\alpha_b = 0.08$ are drawn for reference.

a linear fit to h_b and $A_t g(t - t_0)^2$ is small. The growth rate constant α_b is calculated using the slope of the fitted curve. The parameters obtained for these RTI cases are shown in table 4.3. The value of x_0 is negative for all of the cases, consistent with previous RTI experiments [46]. This value of x_0 accounts for the splitter plate wake effects and the initial transients before the flow transition into the self-similar mixing regime. Although the virtual origin method gives a constant value for $\alpha_{b,s}$, it is calculated based upon the total evolution of the mixing width rather than the local gradients. Overall, the new multi-layer facility gave similar $\alpha_{b,s}$ values as the old facility when used as a two layer facility. However, as discussed in the visualization of the experiments section, the evolution of the flow is little different due to initial conditions at the splitter plate.

Table 4.3: Growth rate parameters α_b, α_s, and x_0 obtained using the virtual origin technique for different RTI only cases using the new multi-layer gas tunnel facility. The uncertainties in the values of α_s and α_b are ± 0.005 calculated based on the maximum and minimum values of dependent parameters. This uncertainty drops to ± 0.0025 if the Kline - McClintock method is used for uncertainty analysis.

Case	α_b	$x_{0,b}$	α_s	$x_{0,s}$
A2S0	0.074	-0.48	0.076	-0.59
A3S0	0.078	-0.52	-	-
A4S0	0.067	-0.69	0.066	-0.74

4.1.3.3 Growth rate parameters for the KHRT instability

For the combined instability, it is proposed that the mixing layer will grow at a rate predicted by

$$h = \beta\ \Delta U\ t + \ 2\ \alpha_{khrt}\ A_t\ g\ t^2, \tag{4.2}$$

which combines the mixing width growth equation for KHI and RTI. In this equation β is the KHI growth rate parameter for the case with same ΔU without any density difference. In equation 4.2, $h = h_s + h_b$ is the total mixing width and $t = \frac{x}{U}$. For velocity ratios $\frac{U}{\Delta U} < 4$, it is reasonable to assume $\beta = 0.17$ (see Table 4.2). After substituting for the value of β, α_{khrt} can be calculated either using the VO method, or the RC method.

The α_{khrt} values obtained for different KHRT cases using both methods are shown in table 4.4. Except for the A1S2 case, all the other cases have α_{khrt} values in between 0.064 - 0.082. For the A1S2 case, the transition to the RTI regime occurs very near to the end of the tunnel. Thus, the α_{khrt} value is equal to the α value if the mixing layer transitioned into RTI like behavior. If the mixing layer is not transitioned into RTI like behavior, α_{khrt} is less than the pure RTI α value. It is interesting to note

Table 4.4: α_{khrt} calculated for the different cases using both VO method, and RC method, taking the β from the shear only experiments at the same set of parameters.

Case	β	$\alpha_{khrt,RC}$	$\alpha_{khrt,vo}$
A1S1	0.21	0.067	0.062
A1S2	0.17	0.032	0.032
A2S1	0.19	0.064	0.060
A2S2	0.15	0.081	0.077
A3S1	0.21	0.081	0.085
A4S1	0.19	0.082	0.079

that irrespective of the amount of the shear present initially for different Atwood numbers, the measured α_{khrt} value is in a smaller range and is equal to the RTI α value. The validity of the statement is true only after the mixing layer is transitioned into RTI like behavior. The next section discusses this transition criterion.

4.1.4 Transition from KHI to RTI

From the visualization study of the combined instability experiments, it is clear that the mixing layer exhibits KHI-like behavior at earlier times, and transitions into RTI-like behavior at a later time. Thus, it is important to quantify this transition point for different cases and determine any criterion for this transition. Then this criterion can be used for different turbulence models to 'switch on and off' a particular type of turbulence behavior. This criterion can also be used to predict the mixing growth rate as explained in the previous section.

Richardson number, quantifies the competition between buoyancy versus shear production for the turbulent kinetic energy in atmospheric and oceanic flows [114]. The Richardson number definition can be extended in the present scenario by integrating each term separately over the mixing width, to the form shown in equation 4.3.

$$Ri = \frac{-4ghA_t}{\Delta U^2} \tag{4.3}$$

The Richardson number can be used to quantify the transition between the two regimes in the combined instability cases.

As the shear mixing layer grows linear with time, the gradient of the mixing width with respect to time is a constant value. The RTI mixing layer grows parabolically in time, and the gradient of the mixing width with respect to time increases linearly with time. For the combined instability cases, the gradient is plotted with the stream-wise distance (time after coordinate transformation), and this transition point is identified by marking the shift from the constant value of the mixing width gradient to the linear variation. The gradient is calculated by a moving window technique, in which two windows of 100 pixels in size are placed side-by-side and traversed downstream. Mixing width values are averaged in each window and the gradient is calculated using the averaged values.

Figure 4.4 shows the mixing width gradients for different ΔU cases at Atwood number A1 ($A_t = 0.035$). Each case in figure shows the actual width gradient, and the corresponding trend lines drawn in black. For the RTI only case (A1S0) the width gradient is linear from figure 4.4 (a). This confirms the quadratic growth in time for RTI mixing layers. For the KHI only case, the mixing width gradient is constant with time confirming the linear growth of the mixing layer. For the combined case A1S1, the gradient has shown a transition in growth from a constant to a linear trend with respect to time. For this case, transition from the shear-dominated flow to the buoyancy-dominated flow is observed $\approx$ 70 - 100 cm downstream distance, which corresponds to a Richardson number range of -1.6 to -2.5. For the combined A1S2 case, this transition point moves further downstream side of the test section due to the larger amount of shear present in the flow initially. This transition occurred at a downstream distance of 150 - 170 cm, which corresponds to a Richardson number range of -1.5 to -1.8.

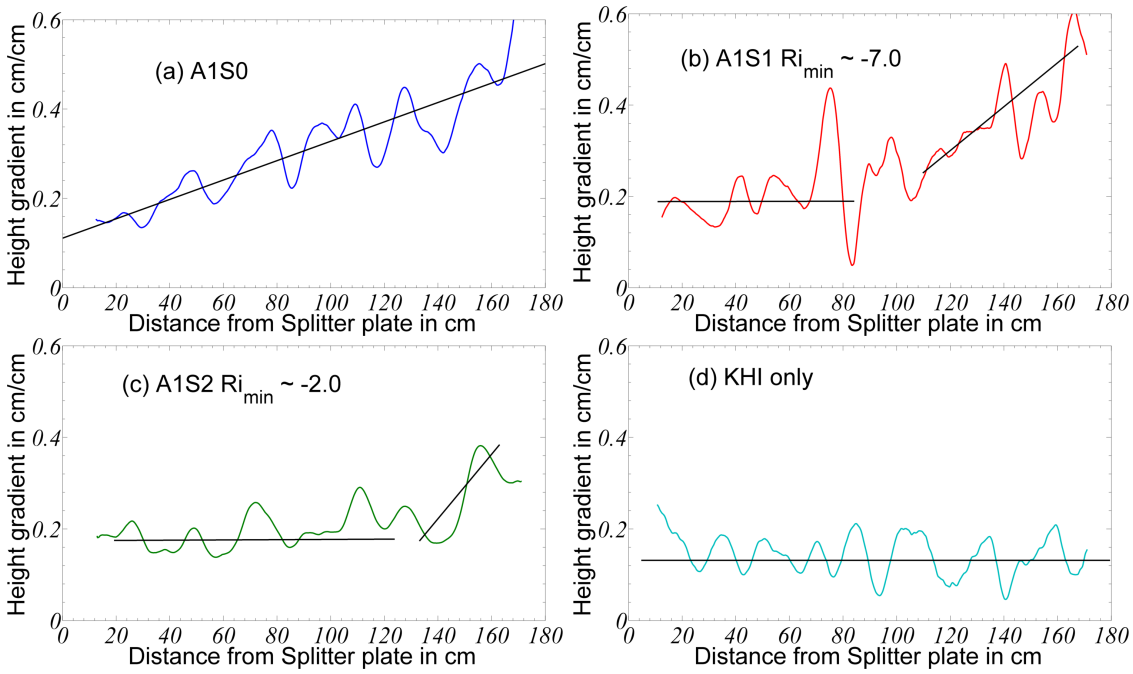

Figure 4.4: Mixing width gradient variation along the test section for different cases (a) A1S0 (b) A1S1 (c) A1S2, and (d) KHI only case.

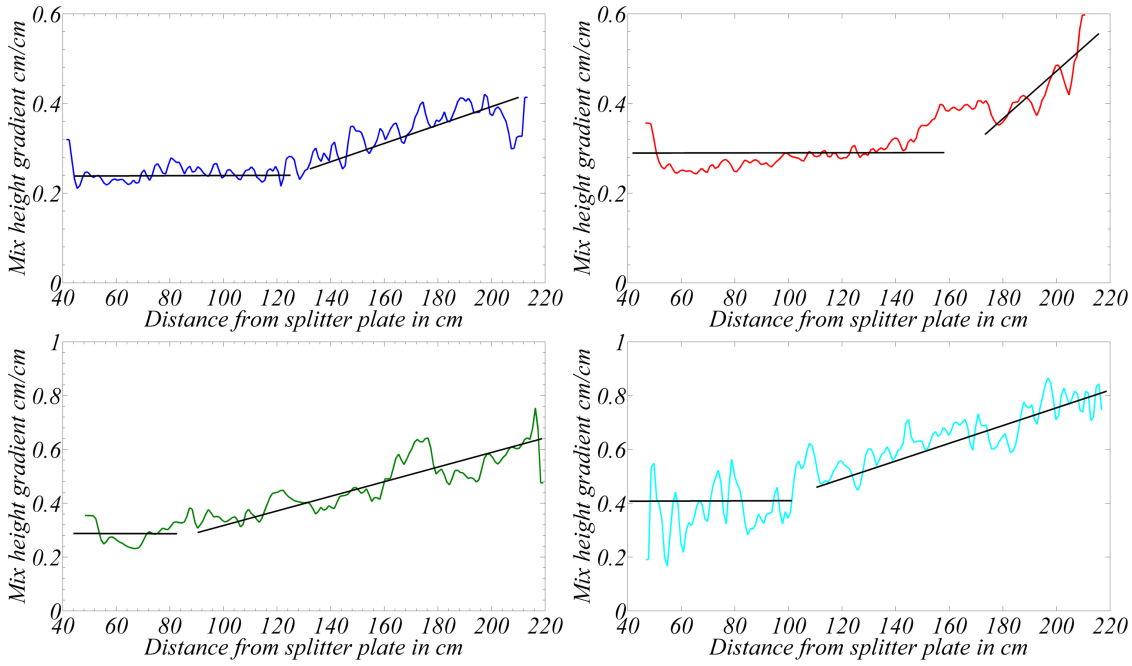

Figure 4.5: Mixing width gradient variation along the test section for different cases (a) A2S1 (b) A2S2 (c) A3S1, and (d) A4S1

All other combined instability A2S1, A2S2, A3S1, and A4S1 experiments are conducted in the new multi-layer gas tunnel facility. As indicated in the visualization section they also show a similar type of behavior as the A1 experimental sets. Figure 4.5 shows the mixing width gradient variation along the test section. The new facility is longer than the older facility. The transition location, the mixing width at that

Table 4.5: Transition location from KHI to RTI (X_{TP}), the total mixing width ($2h_{TP}$), and the Richardson number (Ri_{TP}) at the location for different KHRT cases

Case	X_{TP}	$2h_{TP}$	-Ri_{TP}
A1S1	90	20	2.5
A1S2	145	32	1.4
A2S1	125	19	1.8
A2S2	170	28	0.8
A3S1	75	10	1.3
A4S1	110	21	1.4

location, and the transition Richardson numbers for all the cases are shown in table 4.5. For all the shear cases, the transition Richardson number is in the range -0.8 to -2.5. By looking at the Richardson number ranges more closely for the same Atwood number (A1 and A2), higher shear ratios have shown transition at smaller Richardson numbers, indicating that the transition point is not scaling with the Richardson number definition chosen here. Similarly, the older gas tunnel KHRT experiments transitioned into RTI-like behavior at larger Richardson numbers. As discussed before about the characteristics of the new gas tunnel, the initial conditions are different for both setups. In the older setup, ordered longer wavelengths (corresponding to the rotational frequency of the motor) are present close to the splitter plate due to the vibrations coming from the motors attached to the tunnel. In the new tunnel,

although longer wavelengths are present due to the injection of Helium, the ordered longer wavelengths are absent in the new setup. This difference in initial conditions might have been attributed to the difference in the range of the transition Richardson numbers observed in both setups. The reason for the spread of the range of the Richardson number can also be attributed the definition of the Richardson number. Instead of assuming a constant gradient for ρ, U, if the actual measured value of the gradients are used, then this could lead to collapse in the transitional Richardson number. Although, instantaneous velocity and density information collected across the mixing layer at different stations for the combined instability flows, the analysis is not performed to check the collapse for the Richardson number.

4.2 Hot wire anemometry: Velocity statistics

In this section, results obtained from the hot wire measurements using the S3WCA technique for the A1S0, A1S1, and A1S2 cases are presented. For the S3WCA technique, temperature is used as a marker for density measurements, and a temperature probe is used as a density probe. The velocity probability density function (PDF), velocity spectra, density PDF, spectra, and molecular mixing parameter θ obtained from these combined instability experiments at Atwood number 0.035 (A1) are discussed. The non-dimensional time τ is defined as, $\tau = \frac{X}{U}\sqrt{\frac{A_t g}{H}}$, where H is the total channel width (1.2 m). In most of the numerical simulations for RTI, H is defined as the initial dominant wavelength [21]. The velocity PDF and spectra in the current setup are for fluctuation quantities varying with time at a particular spatial location, and this corresponds to the variation along the mixing layer for box-type conventional experiments. Thus for spectra, although the measurements are made for frequency, it corresponds to the wavenumber along the mixing layer, for the conventional setups.

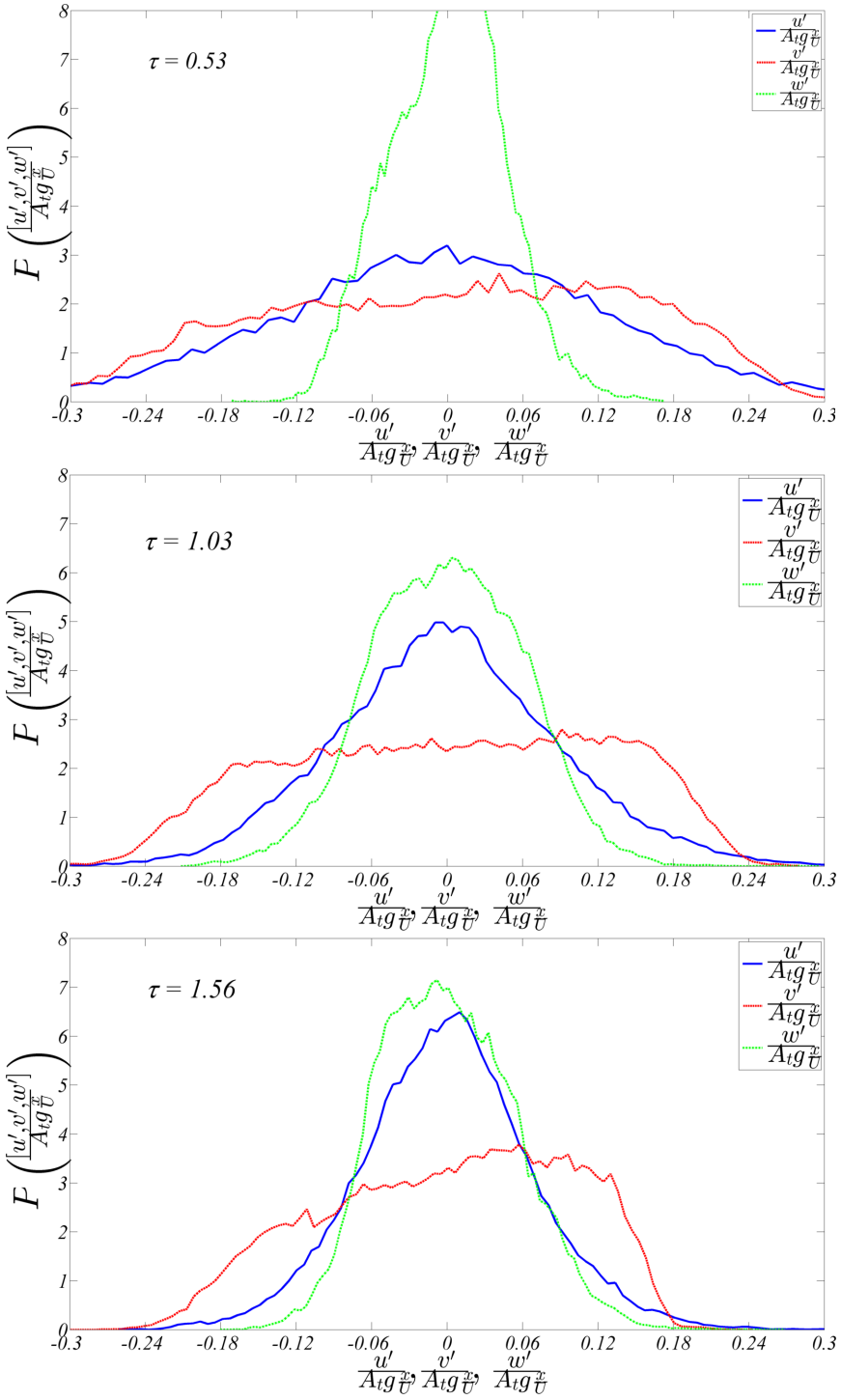

Figure 4.6: Velocity PDF at different stream-wise locations for a buoyancy only case at Atwood number 0.035 (A1S0). The non-dimensional time is $\tau = \frac{x}{U}\sqrt{\frac{A_t g}{H}}$.

4.2.1 Velocity PDF

Figure 4.6 shows the u', v' and w' velocity PDFs at different non-dimensional times, $\tau = 0.53, 1.03, 1.56$ for RTI only case A1S0. The normalization parameter used for all the velocities is $A_t g \frac{x}{U}$, consistent with the relation 3.3. During the initial times at $\tau = 0.53$, when the flow is not self-similar, the u, and v velocities have broader distributions, indicating that the normalized fluctuation velocities are higher than the corresponding self-similar values. This is in accordance with the higher values of $\alpha_{b,s}$ observed at the earlier times of the instability [92]. Also it can be seen that the w' PDF distribution has very large peak around the zero, confirming the two-dimensionality nature of the flow at early times. The u' and v' PDF distributions are similar, and the ratio $\frac{v'}{u'}$ is close to 1 at $\tau = 0.53$. By the time $\tau = 1.03$, the third directional component w' PDF is very much comparable to the u' PDF, indicating that the mixing has transitioned into a three dimensional flow regime. The ratio $\frac{v'}{u'}$ is more than 1.5 by this time, and the v' PDF appears broader than the u', w' PDFs.

Figure 4.7 shows the PDFs for the combined instability case A1S1 at different non-dimensional times $\tau = 0.37, 0.74$, and 1.12. The u' velocity profile, Gaussian shaped at all times, is similar to the one seen for RTI dominated flow. The width of the Gaussian is different at each time, due to the scaling of the velocity fluctuation. At an early time $\tau = 0.37$, when the flow is KHI dominated, the velocity fluctuation does not scale with $A_t g t$ and the Gaussian is much broader. Although, the flow is very two-dimensional at this time, the w' PDF looks much broader due to the choice of scaling. The two-dimensionality of the mixing layer at this time is appreciated when the width of the w' profile is compared with other velocity PDF widths. The ratio $\frac{v'}{u'}$ at this time is less than 1 which is a characteristic of KHI mixing layer [64]. The location $\tau = 0.74$ falls in the transition region from KHI to RTI, and the mixing

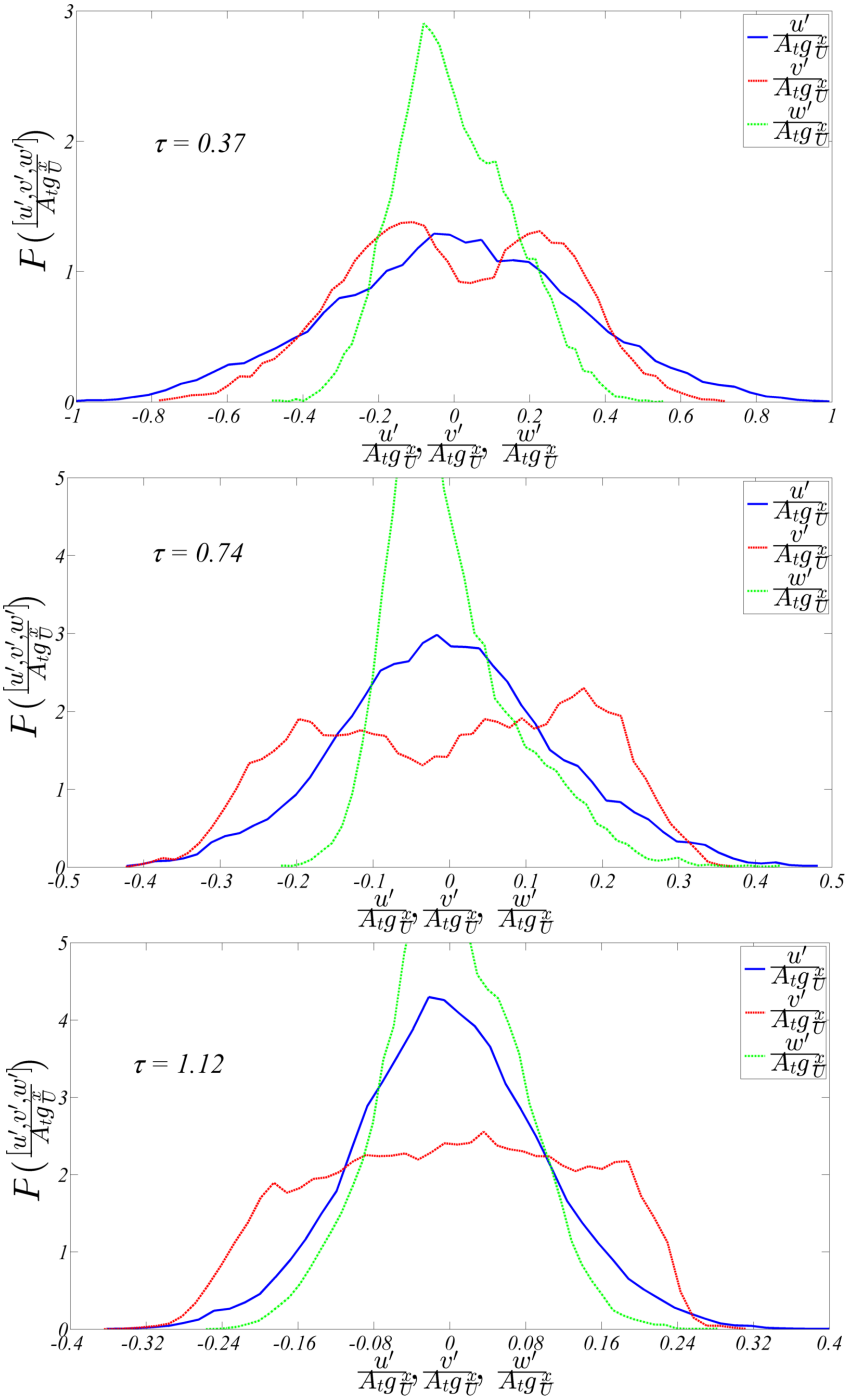

Figure 4.7: Velocity PDF at different stream-wise locations for a combined instability case at Atwood number 0.035 (A1S1), and $\Delta U = 0.23\ m/s$. The non-dimensional time is $\tau = \frac{X}{U}\sqrt{\frac{A_t g}{H}}$.

layer started to become three-dimensional by this point. The relative width of the w' PDF at $\tau = 0.74$ is slightly higher than the time $\tau = 0.37$, compared to other PDF profiles. The u' velocity PDF is still Gaussian shaped and symmetric about the zero fluctuation. The ratio $\frac{v'}{u'}$ is above 1 at this location, as the mixing layer started to show the characteristics of RTI mixing. At $\tau = 1.12$, the flow is RTI dominated and all the PDF and velocity fluctuation rms values show very similar characteristics as compared to self-similar RTI mixing layer at $\tau = 1.56$ in figure 4.6.

4.2.1.1 Vertical Velocity PDF

Although the vertical velocity PDFs are plotted in figures 4.6 and 4.7, they are given special attention due to their interesting behavior compared to other directional velocities. Detailed measurements of velocity, temperature and passive scalars in a plane mixing layer (KHI only flows) were performed by Batt [115]. He presented different turbulence quantities including Reynolds stresses, probability density functions, space-time correlations and spectra in a reactive and non-reactive mixing layer. Wygnanski and Fiedler [116] measured the skewness and kurtosis quantities in a plane mixing layer. Champagne and Wygnanski [117] also made measurements of skewness, kurtosis, probability density functions and presented up to eighth order moments. All these reported measurements are at high Reynolds number well above 100,000.

Figure 4.8 shows the v' velocity PDF at different times after the onset of instability for the A1S0, A1S1, A1S2, and KHI only cases. The skewness and kurtosis values measured at the center of the mixing layer at different stream-wise locations (at different Reynolds numbers), are shown in Figure 4.8. For the KHI only case, the v' PDF distributions are Gaussian shaped at smaller Reynolds numbers (at earlier times). The Reynolds number is defined based on the velocity difference, mixing

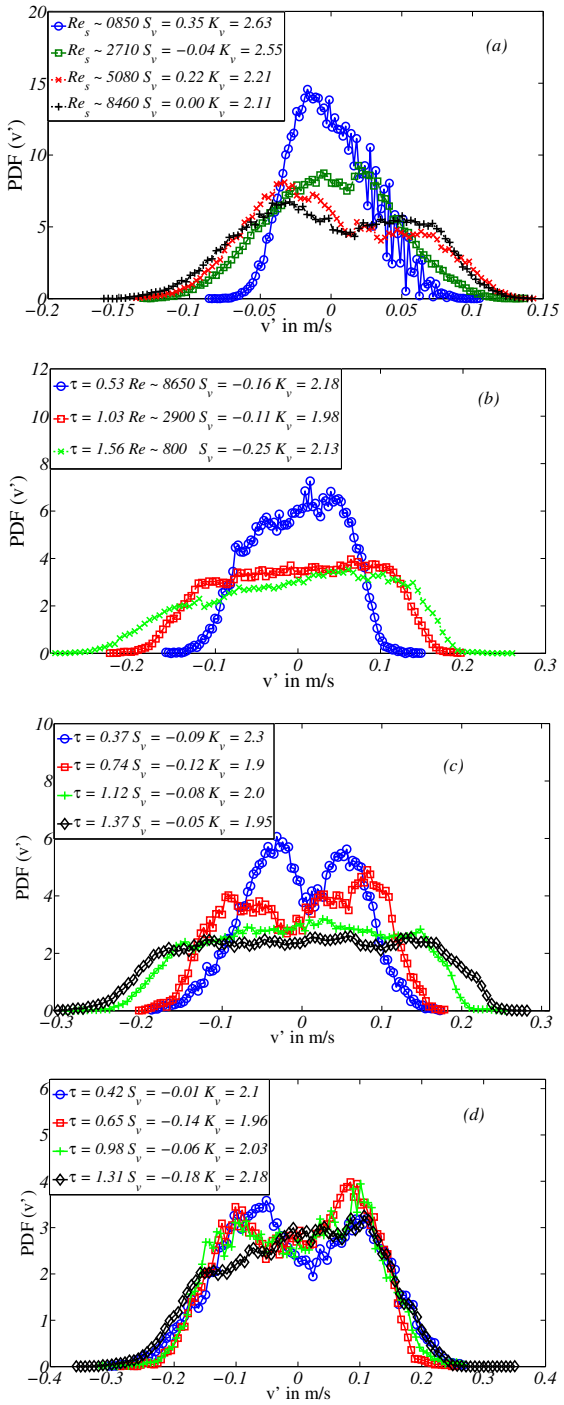

Figure 4.8: Vertical velocity probability density functions close to the center of the mixing layer at different Reynolds numbers (a) for a pure shear case with $Re_s = \Delta U \delta / \nu$ (b) for the A1S0 case with $Re_{RT_h} = (2h)^{3/2}\sqrt{gA_t/6}/\nu_{mix}$, (c) for A1S1 case (d) for A1S2 case, at different times, $\tau = \frac{x}{U}\sqrt{\frac{A_t g}{H}}$.

width and kinematic viscosity of the flow streams ($Re_s = \frac{\Delta U \delta}{\nu}$) for KHI flows. As the Reynolds number increases, the kurtosis value decreases, indicating that the PDF shape is no longer Gaussian. The skewness value is near zero, indicating the symmetric nature of the fluctuations from both streams getting entrained into the center of the mix. The PDF shape also became double peaked as the roll-up structure is developed at higher Reynolds numbers. Thus, the double peaked v' velocity PDF shape is characteristic of KHI flows.

For RTI flows, the Reynolds number indicated in figure 4.8 is according to the definition 3.5 (a). The vertical velocity probability density functions at the center of the RTI mixing layer at different times τ ($= \frac{x}{U}\sqrt{\frac{A_t g}{H}}$), have shown flatter distributions indicating an equal contribution from different range of scales for RTI development. The skewness value is close to zero, indicating the symmetry of the layer. The kurtosis value is ≈ 2.0 for RTI flows, due to the flatness of the PDF shapes. For KHI flows, although the shape of the v' PDF distribution is different compared to RTI, the kurtosis value is still ≈ 2.1 at higher Reynolds numbers.

For the two cases of combined instability flows, the vertical velocity fluctuation PDF is shown in figure 4.8. The PDF distributions have shown double peaked distributions at earlier times for the combined instability and flatter RTI like distributions at later time. The number of peaks increased with time, indicating the generation of structures due to non-linear interaction. The PDF shape eventually looked similar to the ones seen in RTI dominated flows at late times for both the A1S1 and A1S2 cases. The kurtosis value remained constant throughout this PDF evolution at ≈ 2.0. The skewness is always negative, but very close to zero at all times.

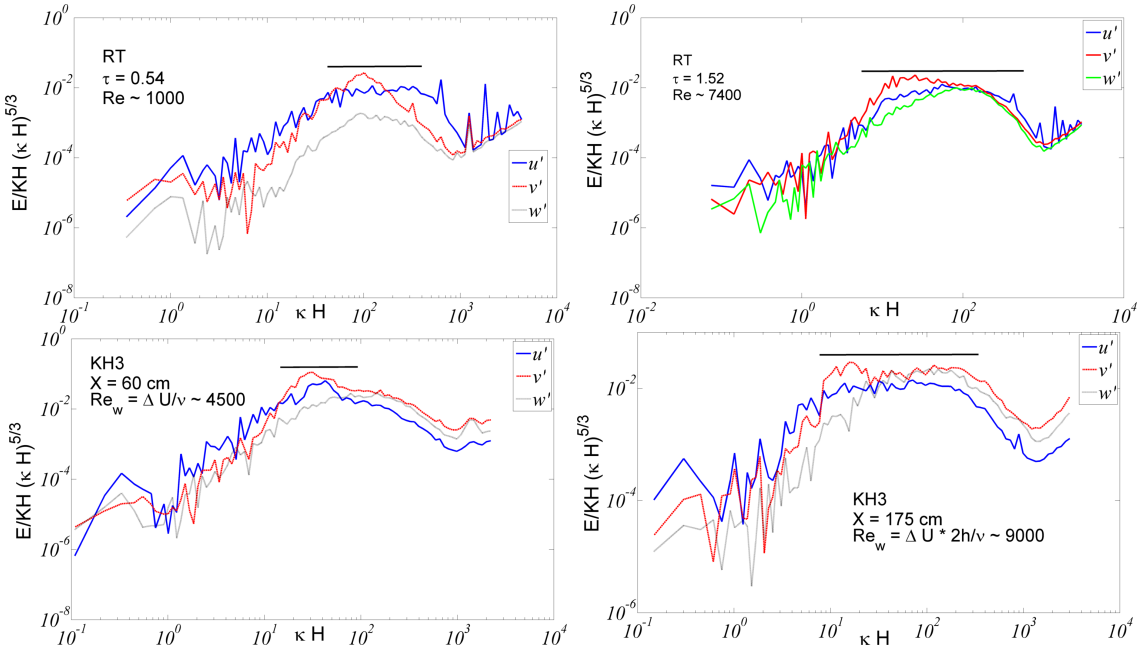

Figure 4.9: Velocity spectra at two different stream-wise locations for RTI at Atwood number 0.035 (A1S0), and KHI with $U1 = 1.25\ m/s$, and $U2 = 0.65\ m/s$. The non-dimensional time is $\tau = \frac{X}{U}\sqrt{\frac{A_t g}{H}}$.

4.2.2 Velocity spectra

Velocity spectra are obtained for all the three velocity component fluctuations, stream-wise velocity u', cross-stream velocity v', and span-wise velocity w'. These fluctuations are in time at a particular spatial location, representing the spatial fluctuations in non-convective box-type conventional systems. Therefore, the frequency measurement becomes wavenumber. This wavenumber is normalized by the total test section height, H (1.2 m). Discrete Fourier transforms are performed to obtain the amplitude of that particular wave for each velocity component, using equation 4.4

$$E_\phi(\kappa) = \left| \frac{1}{N} \sum_{n=1}^{N} \phi(n) e^{-i2\Pi(\kappa-1)(n-1)/N} \right|^2 \tag{4.4}$$

with $\phi = u', v', w', \rho'$. The wavenumber is defined as $\kappa = \frac{2\pi}{\lambda}$, where λ is the wavelength. The largest wavelength L (smaller wave number) is defined as the product of the sampling time T, and the average velocity U, $L = UT$. The smallest wavenumber corresponds to the Nyquist frequency of the sampling frequency (1000 Hz).

Figure 4.9 shows the compensated power spectra for all the velocity component fluctuations. The wavenumber energy is normalized with KH, where K is largest wavenumber, so that the area under the curve becomes unity. To see the inertial range on a horizontal line, the energy on the y axis is also multiplied by $(\kappa H)^{5/3}$. Figure 4.9 shows power spectra of the velocity components measured at two different stream-wise locations for the RTI only A1S0 case, and the KHI only case. For RTI at $\tau = 0.54$, when the instability is still in the early stages, neither v' nor w' have any inertial range, while u' has already has some inertial range. The small scales have not yet developed at this time. At a later time, $\tau = 1.52$, u' has shown inertial range scales for a few decades, and v' and w' have shown an inertial range for a

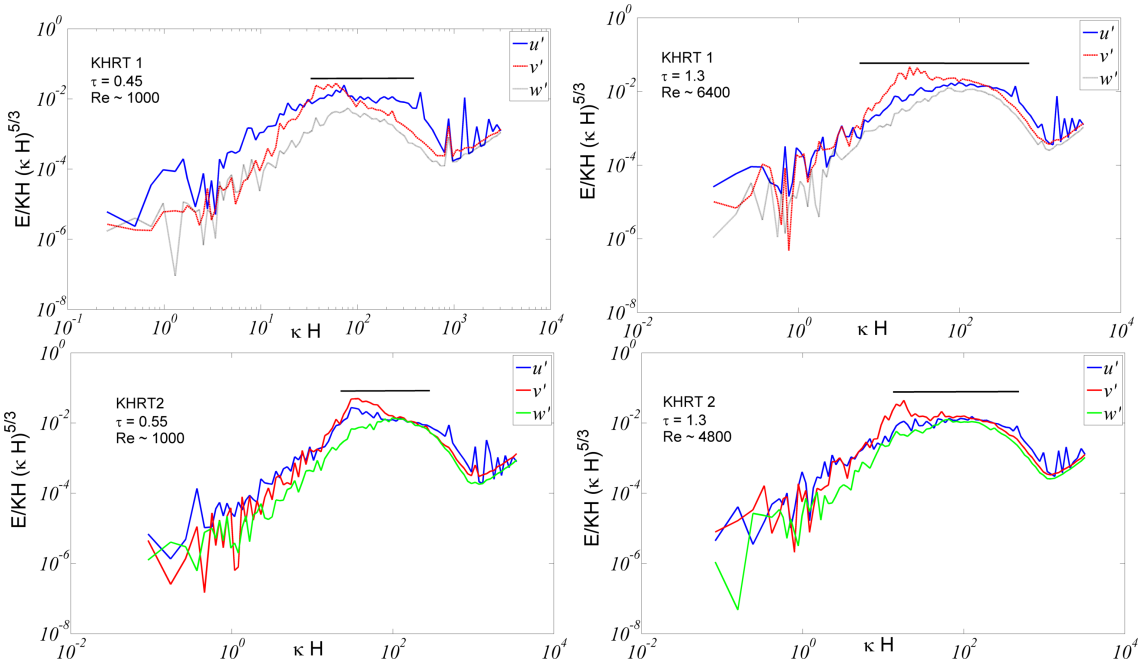

Figure 4.10: Velocity spectra at two different stream-wise locations for KHRT1 (A2S1) and KHRT2 (A2S2). The non-dimensional time is, $\tau = \frac{X}{U}\sqrt{\frac{A_t g}{H}}$.

decade or so. Figure 4.9 also shows the spectra for the KHI only case at two different stream-wise locations. For the KHI case, at an earlier time $Re_w = 4500$, the flow is mostly dominated by larger wavelength structures, with no inertial range. At the second location $Re_w = 9000$, the mixing layer has becomes three-dimensional, and has shown more than two decades a 5/3 inertial range, containing the scales for energy cascading.

Figure 4.10 shows the compensated power spectra of velocity fluctuations for the A1S1 and A1S2 cases, respectively. For these combined instability cases, the spectra evolution is very similar to the RTI case. Two decades of inertial range scales are observed, exhibiting many more scales compared to the RTI only case, indicating that the combined instability cases transition to turbulence faster than the RTI only case.

4.2.3 Molecular mixing and density spectra

The variation of θ, measured at the mixing layer centerline, with non-dimensional time τ for the A1S0, A1S1, and A1S2 cases is plotted in Figure 4.11. In the late self-similar regime ($\tau > 1$), θ value lie in between 0.72 - 0.74 for A1S0 and in good agreement with previously reported values [51, 57]. At $\tau = 0.83$, where the RT plume structures are smaller in size, the $\theta < 0.7$. At $\tau = 1.4$, $\theta \approx 0.73$ indicating that the fluids are well mixed compared with early times. This higher value of θ at late times is due to large secondary KH rollup structures developed between the bubbles and spikes, creating more interfacial area between the fluids. This trend in θ for A1S0 approximately follows the trend measured in water channel experiments [106] also shown in figure 4.11.

For the combined instability cases, the molecular mixing is higher at earlier times as indicated by higher values of θ from Figure 4.11. For KHI, the mixing layer is

dominated by span-wise vortical structures, and these structures create a higher contact area between the two streams compared with RTI structures due to the rolling up of one fluid around another. The larger contact area gives a higher amount of molecular mixing. RTI plume structures are primarily vertical and fine scale mixing is due to shear generated by the rising bubbles and falling spikes. As the flow is dominated by KHI type rollup structures at earlier times for the A1S2 case, $\theta \approx 0.81$ at $\tau = 0.3$ - 0.6, and it is higher than the θ value of the self-similar RTI layer. This early time θ value is ≈ 0.78 for the A1S1 case, which is smaller than the A1S2 case due to smaller span-wise vortices formed because of the smaller amount of shear. The transition from KHI to RTI happens between values of 0.97 - 1.2 for the KH+RT 2 case, and between 0.4 - 0.6 for the A1S1 case. For both combined instability cases, before the transition, the value is reasonably constant and starts dropping in the transition region. This drop in the value can be attributed to breakup of the rollup structure. The value of θ follows the RTI trend after the transition region, indicated by the values measured at the end of the test section that are close to the RTI values for the A1S1 case.

The combined instability cases show a completely different trend in molecular mixing evolution compared to the A1S0 (RTI only) case. The mixture is always well mixed at the center of the mixing layer instead showing the drop and rising trend of the pure RTI mixing layer. This observation has important implications in applications where one has to decide between global and local mixing. Introducing shear will reduce the total mixing width up to a particular time by delaying the quadratic growth to later times, but will introduce large amount of molecular mixing between the fluids.

Figure 4.12 shows the compensated density spectra for the A1 case with and without shear. The density spectra has shown the 5/3 inertial range from the earlier

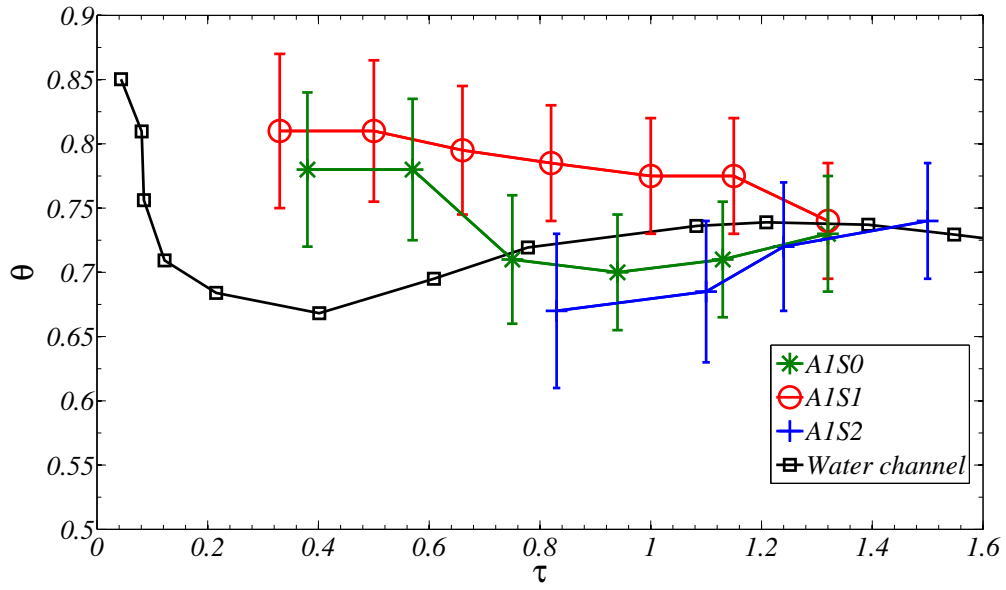

Figure 4.11: Molecular mixing parameter, θ variation with non-dimensional time $\tau = \frac{x}{U}\sqrt{\frac{A_t g}{H}}$, for cases A1S0, A1S1, and A1S2. Water channel measurements are also shown for comparison.

times. The density field seems to becoming turbulent earlier than the velocity field. It has shown at least two decades of wavenumbers in the inertial range for all the cases at later times. For their stratified wake simulation, de Stadler *et al.* [118] have also observed that their density field showed inertial range scales far too early compared to the turbulent kinetic energy k.

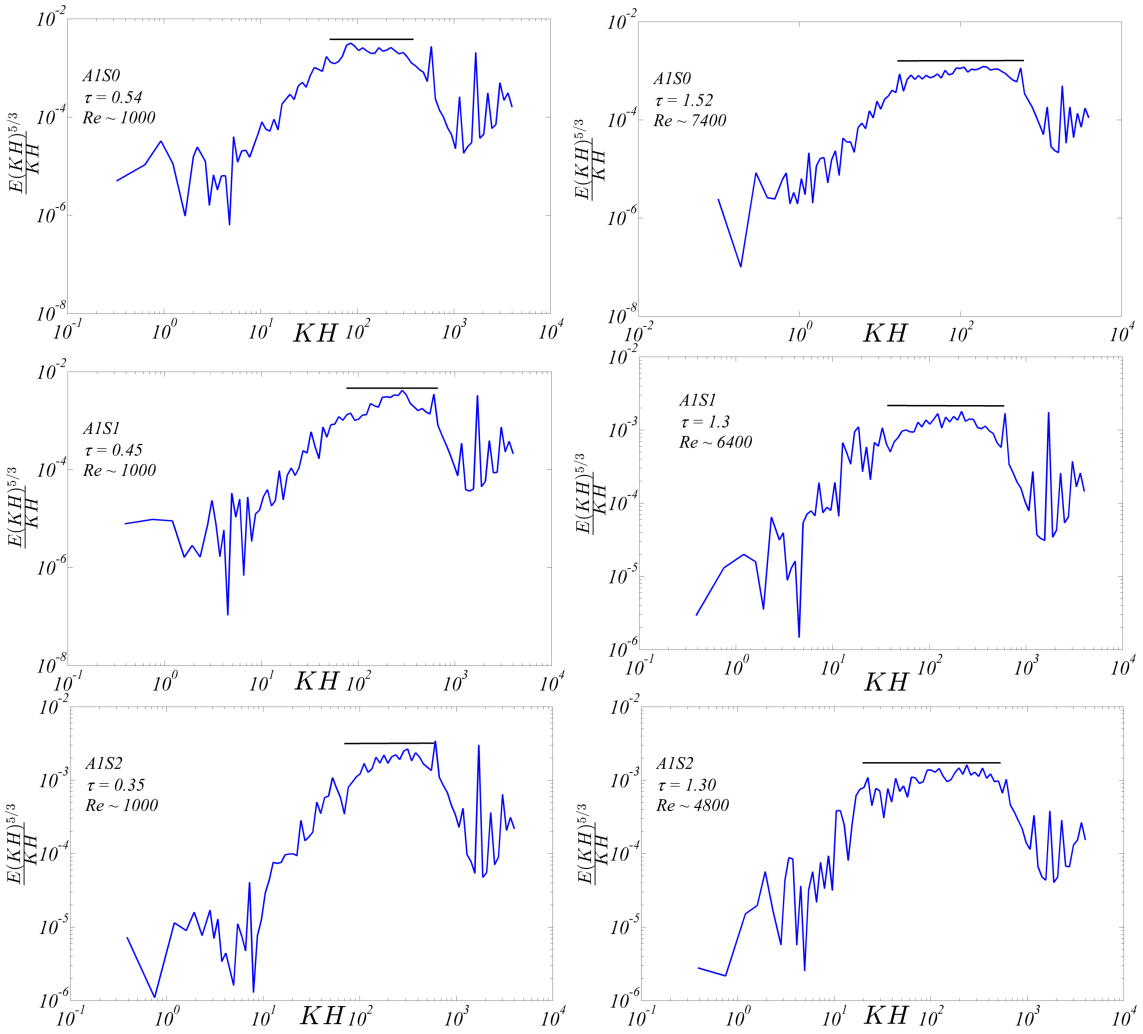

Figure 4.12: Compensated spectra of density fluctuation for A1S0, A1S1, and A1S2 cases.

5. CONCLUSIONS

The work presented in the thesis has three main objectives. The first objective is to construct a multi layer gas tunnel facility. The second objective is to obtain velocity and density statistics in a high Atwood number Rayleigh - Taylor mixing layer. The third objective is to combine the KHI instability with RTI and study the effect on mixing growth rates, velocity statistics, and molecular mixing. An existing two layer gas channel facility [56] is used to accomplish part of objective three. But this facility could not be used for higher Atwood numbers greater than (0.6) due to velocity limitations, back flows, PIV implementation, and space limitation around the facility [59]. Taking these limitations into account, a new multi layer gas tunnel facility was constructed to enable carrying out experiments required to complete objective 2 and the rest of objective 3. Although this facility can handle up to eight different streams, it is setup for three streams in the present work, and the middle and bottom streams are only used for these two layer experiments.

A new density probe was designed to measure the Helium volume fraction directly, instead of the temperature marker technique used previously [59]. This technique is based on hot wire anemometry with a X-wire probe.

5.1 Objective 1: High Atwood number experiments

1. For the first time, detailed instantaneous density and velocity measurements are made at Atwood number 0.75. The results available until now are based on visualization only. Field-wise measurements using PIV are performed for the first time at this Atwood number.

2. From the visualization experiments, large asymmetry in the flow field is noticed

at the present Atwood number of 0.75. The ratio of spike growth rate to bubble growth rate is$\approx$ 1.8. The measured asymmetry value is in good agreement with the empirical relation of Dimonte and Schneider [20].

3. The planar Mie scattering images and the PIV measurements highlight dendrite-like spike structures, with span-wise vortical roll-up structures developing at different points along the spike structure. PIV captured the small scale structures around these roll-ups very well.

4. Even at this high Atwood number, the vertical velocity fluctuation rms v' correlated well with the mixing growth rate and was equal to the average mixing growth rate calculated from visualization.

5. The velocity statistics u' and v' rms quantities have shown self-similar behavior at late time. They are self-similar with respect to normalized mixing width and terminal bubble velocities predicted by Birkhoff [105].

6. The turbulent statistics, including velocity probability density functions, skewness, kurtosis, and anisotropy tensor, variation across the mixing layer is similar to that in small Atwood number experiments ($A_t < 10^{-3}$) [51].

7. The molecular mixing parameter θ value is around 0.7 across the mixing layer, increasing to higher values at the edges of the mixing layer.

5.2 Objective 2: Combined instability experiments

1. For the combined instability KH+RT experiments, mixing during the initial times is dominated by shear and transitions into RTI-like behavior at later times. The mixing growth rate for the combined instability in the shear-dominated region is higher than measured mixing growth rates from the shear only experiments.

2. The transition point from KHI-like behavior to RTI-like behavior depends upon the amount of shear present in the flow, as well as on the Atwood number. If the flow transitions into RTI like behavior, the mixing width can be predicted by simply combining the shear only growth rate and RTI only growth rate.

3. An attempt has been made to quantify the transition point using the Richardson number. Experiments with four different Atwood numbers and different shear values have transitioned from initial KHI-like behavior into RTI like behavior around Richardson number values -0.8 to -2.3. This range is large and may be due to two different reasons. The experiments performed in the old gas channel facility have shown the transition to be on the higher side of this range, and the new facility experiments have shown the transition point on the lower side of this range. This shows that this transition is sensitive to initial conditions, which are different in both setups. The second reason is the simplification of the Richardson number definition itself.

4. The u' and w' velocity PDFs always show Gaussian type behavior for the combined instability experiments. Three-dimensionality is achieved faster in time compared to the RTI only cases. The v' PDF has shown multiple peaks in the transition region, changing from double-peaked KHI behavior to flat RTI behavior.

5. The spectra for the velocity fluctuations have shown a larger number of scales in the inertial range for the combined instability cases, showing that turbulence develops faster with the introduction of shear. The density spectra have shown a larger number of inertial range scales compared to velocity spectra, similar to the behavior observed in stratified wake flows.

6. The molecular mixing parameter θ evolution is also quite different compared to RTI only case. The introduction of shear leads to an increase in the molecular mixing at earlier times when compared to the RTI case.

The measurements of the turbulent statistics at this high Atwood number are important in validating turbulence codes for ICF capsule design. The understanding of the combined instability and transition between different regimes has important implications in combining the effect of laser drive asymmetry on RTI growth for ICF capsule design.

REFERENCES

[1] J. D. Lindl and W. C. Mead, Physical Review Letters **34**, 1273 (1975).

[2] S. W. Haan, Physical Review A **39**, 5812 (1989).

[3] B. A. Hammel *et al.*, High Energy Density Physics **6**, 171 (2010).

[4] A. Burrows, Nature **403**, 727 (2000).

[5] I. Hachisu, T. Matsuda, K. Nomoto, and T. Shigeyama, The Astrophysical Journal **368**, L27 (1991).

[6] J. Arons and S. M. Lea, The Astrophysical Journal **207**, 914 (1976).

[7] S. V. Sazonov, Planetary and Space Science **39**, 1667 (1991).

[8] W. S. D. Wilcock and J. A. Whitehead, Journal of Geophysical Research: Solid Earth **96**, 12193 (1991).

[9] K. O. Mikaelian, Physics of Fluids **6**, 1943 (1994).

[10] N. M. Hoffman, M. B. Hooper, and P. Osborne, Laser Plasma Interactions 5: Inertial Confinement Fusion , 105 (1994).

[11] J. W. S. Rayleigh, London Mathematical Society **14**, 170 (1883).

[12] G. Taylor, Proceedings of the Royal Society of London. Series A, Mathematical and Physical Sciences , 192 (1950).

[13] P. G. Drazin and W. H. Reid, *Hydrodynamic stability* (Cambridge Univ Pr, 2004).

[14] D. Layzer, The Astrophysical Journal **122**, 1 (1955).

[15] V. N. Goncharov, Physical Review Letters **88**, 134502 (2002).

[16] D. H. Sharp, Physica D: Nonlinear Phenomena **12**, 3 (1984).

[17] D. L. Youngs, Physica D: Nonlinear Phenomena **12**, 32 (1984).

[18] D. J. Lewis, Proceedings of the Royal Society of London. Series A, Mathematical and Physical Sciences , 81 (1950).

[19] G. Dimonte *et al.*, Physics of Fluids **16**, 1668 (2004).

[20] G. Dimonte and M. Schneider, Physics of Fluids **12**, 304 (2000).

[21] W. H. Cabot and A. W. Cook, Nature Physics **2**, 562 (2006).

[22] A. W. Cook and P. E. Dimotakis, Journal of Fluid Mechanics **443**, 69 (2001).

[23] A. Banerjee and M. J. Andrews, International Journal of Heat and Mass Transfer **52**, 3906 (2009).

[24] K. I. Read, Physica D: Nonlinear Phenomena **12**, 45 (1984).

[25] D. M. Snider and M. J. Andrews, Physics of Fluids **6**, 3324 (1994).

[26] G. Dimonte, P. K. Ramaprabhu, D. L. Youngs, M. J. Andrews, and R. Rosner, Physics of Plasmas **12**, 056301 (2005).

[27] P. K. Ramaprabhu, G. Dimonte, and M. J. Andrews, Journal of Fluid Mechanics **536**, 285 (2005).

[28] S. B. Dalziel, P. F. Linden, and D. L. Youngs, Journal of Fluid Mechanics **399**, 1 (1999).

[29] N. J. Mueschke, M. J. Andrews, and O. Schilling, Journal of Fluid Mechanics **567**, 27 (2006).

[30] N. J. Mueschke and O. Schilling, Physics of Fluids **21**, 014106 (2009).

[31] N. J. Mueschke and O. Schilling, Physics of Fluids **21**, 014107 (2009).

[32] M. J. Andrews and S. B. Dalziel, Philosophical Transactions of the Royal Society A: Mathematical, Physical and Engineering Sciences **368**, 1663 (2010).

[33] H. W. Emmons, C. T. Chang, and B. C. Watson, Journal of Fluid Mechanics **7**, 177 (1960).

[34] M. Ratafia, Physics of Fluids **16**, 1207 (1973).

[35] R. L. Cole and R. S. Tankin, Physics of Fluids **16**, 1810 (1973).

[36] J. T. Waddell, C. E. Niederhaus, and J. W. Jacobs, Physics of Fluids **13**, 1263 (2001).

[37] G. Dimonte and M. Schneider, Physical Review E **54**, 3740 (1996).

[38] Y. A. Kuchrenko *et al.*, Laser and Particle Beams **21**, 369 (2003).

[39] M. J. Andrews and D. B. Spalding, Physics of Fluids A: Fluid Dynamics **2**, 922 (1990).

[40] S. B. Dalziel, Dynamics of Atmospheres and Oceans **20**, 127 (1993).

[41] J. White, J. Oakley, M. Anderson, and R. Bonazza, Physical Review E **81**, 026303 (2010).

[42] Z. Huang *et al.*, Physical Review Letters **99**, 204502 (2007).

[43] V. Tsiklashvili, P. R. Colio, O. A. Likhachev, and J. W. Jacobs, Physics of Fluids **24**, 052106 (2012).

[44] B. A. Remington *et al.*, Physical Review Letters **73**, 545 (1994).

[45] K. Budil, B. Remington, S. Weber, T. Perry, and T. Peyser, Lawrence Livermore National Lab report, UCRL-JC-127732 (1997).

[46] D. M. Snider, *A study of compound buoyancy and shear mixing*, PhD thesis, Texas A& M University, 1994.

[47] S. B. Pope, *Turbulent flows* (Cambridge Univ Pr, 2000).

[48] P. N. Wilson, M. J. Andrews, and F. Harlow, Physics of Fluids **11**, 2425 (1999).

[49] P. N. Wilson and M. J. Andrews, Physics of Fluids **14**, 938 (2002).

[50] P. N. Wilson, *A study of buoyancy and shear driven turbulence within a closed water channel*, PhD thesis, Texas A&M University, 2002.

[51] P. K. Ramaprabhu and M. J. Andrews, Journal of Fluid Mechanics **502**, 233 (2004).

[52] P. K. Ramaprabhu and M. J. Andrews, Experiments in fluids **34**, 98 (2003).

[53] N. J. Mueschke, *Experimental and numerical study of molecular mixing dynamics in Rayleigh-Taylor unstable flows*, PhD thesis, Texas A&M University, 2008.

[54] N. J. Mueschke, O. Schilling, D. L. Youngs, and M. J. Andrews, Journal of Fluid Mechanics **632**, 17 (2009).

[55] A. Banerjee and M. J. Andrews, Physics of Fluids **18**, 035107 (2006).

[56] A. Banerjee, *Statistically steady measurements of Rayleigh-Taylor mixing in a gas channel*, PhD thesis, Texas A& M University, 2004.

[57] A. Banerjee, W. N. Kraft, and M. J. Andrews, Journal of Fluid Mechanics **659**, 127 (2010).

[58] W. N. Kraft, A. Banerjee, and M. J. Andrews, Experiments in fluids **47**, 49 (2009).

[59] W. N. Kraft, *Simultaneous and instantaneous measurement of velocity and density in Rayleigh-Taylor mixing layers*, PhD thesis, Texas A&M University, 2008.

[60] H. H. Bruun, *Hot-wire anemometry: principles and signal analysis* (Oxford Press, 1995).

[61] H. Gortler, ZAMM - Journal of Applied Mathematics and Mechanics **22**, 244 (1942).

[62] C. M. Sabin, Journal of Basic Engineering **87**, 421 (1965).

[63] H. W. Liepmann and J. Laufer, NACA TN **1257** (1947).

[64] J. H. Bell and R. D. Mehta, AIAA Journal **28**, 2034 (1990).

[65] C. D. Winant and F. K. Browand, Journal of Fluid Mechanics **63**, 237 (1974).

[66] F. K. Browand and P. D. Weidman, Journal of Fluid Mechanics **76**, 127 (1976).

[67] G. L. Brown and A. Roshko, Journal of Fluid Mechanics **64**, 775 (1974).

[68] M. M. Koochesfahani and P. E. Dimotakis, Journal of Fluid Mechanics **170**, 83 (1986).

[69] J. C. Lasheras and H. Choi, Journal of Fluid Mechanics **189**, 53 (1988).

[70] M. M. Koochesfahani, *Experiments on turbulent mixing and chemical reactions in a liquid mixing layer*, PhD thesis, California Institute of Technology, 1984.

[71] M. M. Rogers and R. D. Moser, Physics of Fluids **6**, 903 (1994).

[72] P. E. Dimotakis, High Speed Flight Propulsion Systems **137**, 265 (1991).

[73] J. S. Turner, *Buoyancy effects in fluids* (Cambridge Univ Pr, 1980).

[74] S. A. Thorpe, Journal of Fluid Mechanics **32**, 693 (1968).

[75] S. A. Thorpe, Journal of Fluid Mechanics **61**, 731 (1973).

[76] S. A. Thorpe, Boundary-Layer Meteorology **5**, 95 (1973).

[77] F. K. Browand and C. D. Winant, Boundary-Layer Meteorology **5**, 67 (1973).

[78] C. G. Koop and F. K. Browand, Journal of Fluid Mechanics **93**, 135 (1979).

[79] U. Shumlak and N. F. Roderick, Physics of Plasmas **5**, 2384 (1998).

[80] G. A. Lawrence, F. K. Browand, and L. G. Redekopp, Physics of Fluids A **3**, 2360 (1991).

[81] D. M. Snider and M. J. Andrews, Journal of Fluids Engineering **118**, 55 (1996).

[82] D. M. Snider and M. J. Andrews, Journal of Fluids Engineering **118**, 370 (1996).

[83] B. J. Olson, J. Larsson, S. K. Lele, and A. W. Cook, Physics of Fluids **23**, 114107 (2011).

[84] E. M. Laws and J. L. Livesey, Annual Review of Fluid Mechanics **10**, 247 (1978).

[85] R. I. Loehrke and H. M. Nagib, AGARD Report No. 598 (1972).

[86] G. B. Schubauer, W. G. Spangenberg, and P. S. Klebanoff, NACA TN 2001 (1950).

[87] J. Tan-Atichat, H. M. Nagib, and R. I. Loehrke, Journal of Fluid Mechanics **114**, 501 (1982).

[88] J. Groth and A. V. Johansson, Journal of Fluid Mechanics **197**, 139 (1988).

[89] C. G. Koop, NASA STI/Recon Technical Report N **77**, 16303 (1976).

[90] J. H. Bell and R. D. Mehta, NASA Report JIAA TR - 89 (1989).

[91] R. I. Loehrke and H. M. Nagib, Journal of Fluids Engineering **98**, 342 (1976).

[92] B. Akula, M. J. Andrews, and D. Ranjan, Physical Review E **87**, 033013 (2013).

[93] P. A. Libby and J. Way, AIAA Journal **8**, 976 (1970).

[94] P. A. Libby and J. Way, AIAA Journal **9**, 1567 (1971).

[95] R. A. Stanford and P. A. Libby, Physics of Fluids **17**, 1353 (1974).

[96] A. Sirivat and Z. Warhaft, Journal of Fluid Mechanics **120**, 475 (1982).

[97] N. R. Panchapakesan and J. L. Lumley, Journal of Fluid Mechanics **246**, 225 (1993).

[98] J. L. Harion, M. Favre-Marinet, and B. Camano, Experiments in Fluids **22**, 174 (1996).

[99] O. Mazur, P. Jonáš, J. Šarboch, and V. Uruba, PAMM **2**, 336 (2003).

[100] J. C. LaRue and P. A. Libby, Physics of Fluids **20**, 192 (1977).

[101] J. C. LaRue and P. A. Libby, Physics of Fluids **23**, 1111 (1980).

[102] J. R. Ristorcelli and T. T. Clark, Journal of Fluid Mechanics **507**, 213 (2004).

[103] C. R. Wilke, The Journal of Chemical Physics **18**, 517 (1950).

[104] B. J. Daly, Physics of Fluids **10**, 297 (1967).

[105] G. Birkhoff and D. Carter, Journal of Rational Mechanics and Analysis **6**, 769 (1957).

[106] P. K. Ramaprabhu, *On the Dynamics of Rayleigh-Taylor mixing*, PhD thesis, Texas A&M University, 2003.

[107] S. S. Girimaji, Journal of Fluid Mechanics **422**, 91 (2000).

[108] P. V. Danckwerts, Applied Scientific Research **3**, 279 (1952).

[109] D. L. Youngs, Physics of Fluids A **3**, 1312 (1991).

[110] M. J. Moran and H. N. Shapiro, *Fundamentals of engineering thermodynamics* (Hoboken: Wiley, 2000).

[111] A. Banerjee, R. A. Gore, and M. J. Andrews, Physical Review E **82**, 046309 (2010).

[112] Y. A. Kuchrenko, L. I. Shibarshov, V. I. Chitaikin, S. I. Balabin, and A. P. Pylaev, in Proceedings of the Third International Workshop on the physics of Compressible Turbulent Mixing , 427 (1991).

[113] J. A. Zufiria, Physics of Fluids **31**, 440 (1988).

[114] R. Lyons, H. A. Panofsky, and S. Wollaston, Journal of Applied Meteorology **3**, 136 (1964).

[115] R. G. Batt, Journal of Fluid Mechanics **82**, 53 (1977).

[116] I. Wygnanski and H. E. Fiedler, Journal of Fluid Mechanics **41**, 327 (1970).

[117] F. H. Champagne, Y. H. Pao, and I. J. Wygnanski, Journal of Fluid Mechanics **74**, 209 (1976).

[118] M. B. de Stadler, S. Sarkar, and K. A. Brucker, Physics of Fluids **22**, 095102 (2010).